Dissertation

submitted to the
Combined Faculties of the Natural Sciences and Mathematics
of the Ruperto-Carola-University of Heidelberg, Germany
for the degree of
Doctor of Natural Sciences

Put forward by
Dipl.-Phys. Sara Tegami
born in: Genoa

Oral examination: 08.02.2013

LET measurements
with a Liquid Ionization Chamber

Referees: **Prof. Dr. Joachim Ullrich**
Prof. Dr. Wolfgang Schlegel

To my family and my friends, for their love and support

LET-Messungen mit einer Flüssigkeitsionisationskammer—Tiefliegende Tumore können mit schweren geladenen Teilchen effizient behandelt werden. Die Charakteristik der verursachten Energiedosis innerhalb des Gewebes (Bragg Peak) erlaubt es, eine hohe Energiedosis innerhalb des Tumors zu platzieren, während das umgebende gesunde Gewebe verschont bleibt. Verglichen mit Protonen verursachen schwere Ionen wie Kohlenstoff oder Sauerstoff eine höhere Anzahl von Ionisationsereignissen entlang ihrer Bahn (und insbesondere am Ende der Ionenstrahlbahn), was zu irreparablen Schäden in der DNS der Tumorzellen führt. Die Dichte solcher Ionisationsereignisse wird mittels des linearen Energieübertrags (engl. *Linear Energy Transfer, LET*) beschrieben, einer wichtigen physikalischen Größe, die jedoch schwer direkt zu messen ist. Das Ziel dieser Arbeit ist die Bestimmung des LET der Strahlen bei der Hadronentherapie unter Verwendung von Flüssigkeitsionisationskammern (engl. *Liquid Ionization Chambers, LIC*). Das Ionisationssignal in LICs wird von starken Rekombinationseffekten beeinflusst, welche vom LET der eintreffenden Strahlung abhängen. Die unterschiedlichen Rekombinationseffekte in LICs und luftgefüllten Ionisationskammern können ausgenutzt werden um den sogenannten Rekombinationsindex zu erhalten, welcher mit dem mit Monte Carlo Methoden berechneten LET verknüpft werden kann. Wir haben daher eine Methode entwickelt eine Kalibrationskurve zu erstellen, welche den Rekombinationsindex mit dem LET in jeder Tiefe innerhalb des Gewebes in Verbindung bringt. Das Ergebnis dieser Arbeit kann für die Online-Überwachung der Ionenstrahlqualität verwendet werden.

LET measurements with a Liquid Ionization Chamber—Deep-seated tumors can be efficiently treated with heavy charged particles. The characteristic depth dose profile inside the tissue (Bragg peak) allows to deliver a high dose inside the tumor, while sparing the neighboring healthy tissue. As compared to protons, heavy ions like carbon or oxygen produce a higher amount of ionization events along their track (and in particular at the end of the ion beam path), resulting in an irreparable damage to the DNA of the tumor cells. The density of such ionization events is described in terms of Linear Energy Transfer (LET), an important physical quantity, but difficult to be measured directly. The aim of this work is to determine LET of hadrontherapy beams by using Liquid Ionization Chambers (LIC). The ionization signal in LICs is affected by recombination effects that depend on the LET of the incident radiation. Differences in recombination effects in LICs and air-filled ionization chambers can be exploited to obtain the recombination index, which can be related to the LET, calculated by Monte Carlo methods. We thus developed a method to construct a calibration curve, which relates the recombination index with the LET at each depth in water. The result of this work can be used for online monitoring of the ion beam quality.

List of Publications

Part of this work has been object of a patent submitted in June, 2012 (Spain).

Patent title:

"Method and apparatus for measuring linear energy transfer and energy of hadron beams"

Authors: Faustino Gómez Rodríguez; Juan Pardo Montero; Sara Tegami; Michael Holzscheiter
Patent holding body: Universidade de Santiago de Compostela
Application number: P201231211
Priority country: Spain
Date: 27/07/2012

Further publications with own contributions :

"Analysis of ionic mobilities in liquid isooctane with low dose radiotherapy pulsed photon beams"

J.Pardo-Montero, S.Tegami, A.Gago-Arias, D.M.González-Castaño, M.H.Holzscheiter, F.Gómez.
published by Journal of Instrumentation, Volume 7, September 2012.

Abbreviations

$2D$ = Two Dimensional
$2DR$ = Two Dose Rate Method
$2VM$ = Two Voltage Method
$3VM$ = Three Voltage Method
ACE = Antiproton Cell Experiment
AD = Antiproton Decelerator
BP = Bragg Peak
CPE = Charged Particle Equilibrium
$CSDA$ = Continuous Slowing Down Approximation
$DKFZ$ = Deutsches KrebsForschungsZentrum
DSB = Double Strand Break
ECR = Electron Cyclotron Resonance
GR = General Recombination
HDR = High Dose Rate
$HEBT$ = High Energy Beam Transport line
HIT = Heidelberg Ion-Beam Therapy Center
IC = Ionization Chamber
$IMRT$ = Intensity Modulated Radiation Therapy
IR = Initial Recombination
LDR = Low Dose Rate
$LEBT$ = Low Energy Beam Transport line
LEM = Local Effect Model
LET = Linear Energy Transfer
LET^D = Dose Averaged Linear Energy Transfer
LET^F = Fluence Averaged Linear Energy Transfer
LIC = Liquid Ionization Chamber
$LINAC$ = LINear ACcelerator
LQ = linear quadratic
MC = Monte Carlo
MLC = Multileaf Collimator
MU = Monitor Unit

PCB = Printed Circuit Board
PS = Proton Synchrotron
QA = Quality Assurance
RFQ = Radio Frequency Quadrupole
RBE = Relative Biological Effectiveness
$SOBP$ = Spread Out Bragg Peak
SSB = Single Strand Break
SSD = Source to Surface Distance
USC = University of Santiago de Compostela

Contents

Aim of the Thesis

The main advantage of charged-particle cancer therapy as compared to conventional radiotherapy is the geometrical shape of the energy deposition inside the body. The sharp Bragg peak allows to deliver a high dose in a deep seated tumor, while sparing neighboring healthy tissues in the entrance channel and beyond the Bragg peak. In particular, beams containing heavy ions, such as carbon or oxygen, offer an additional advantage as compared to protons: due to their enhanced nuclear charge, heavy-ion beams cause higher density of ionization events along their track as they travel through the target resulting in a multitude of double strand breaks in the DNA molecules of the cells, which constitutes an irreparable damage to them. For a carbon ion beam, this desired effect is much more pronounced at the end of the ion beam path, and is hence the origin of the enhanced biological efficiency at the Bragg peak.

This biological efficiency is described in terms of Relative Biological Effectiveness (RBE). The RBE is usually determined via in-vitro cell-killing experiments or through biophysical models. Despite the fact that these two approaches give comparable results, uncertainty in the RBE calculation remains a source of concern in the dose prescription during particle treatment plans. RBE depends upon many parameters, both biological (tissue type, repair capability, oxygenation level) and physical, such as dose, dose rate, particle type etc. A fundamental physical property of the beam closely related to RBE is the Linear Energy Transfer (LET). The LET can be calculated from physical interaction models using Monte Carlo simulation techniques, however, an experimental way to verify the reliability of LET calculations is still missing.

Despite many attempts to perform an LET measurement using different kinds of detectors and techniques, up to now, nobody managed to experimentally determine LET in tissue with sufficient accuracy. The most-used detectors in radiotherapy are air-filled ionization chambers (ICs). But due to the steep dose gradients present in particle therapy close to the Bragg peak,

the dose needs to be monitored with better spatial resolution than achievable with ICs and the tendency is the reduction of the detector size. For this reason, liquid-filled ionization chambers (LICs) have been proposed as an alternative to the more widely used ICs. On the other hand, the main drawback of using a liquid medium is the higher amount of recombination effects taking place in the sensitive volume, which need to be corrected for before an absolute dose value can be extracted. Recombination can be grouped into two main categories: initial recombination (IR), involving electron-ion pairs produced along one single particle track, and general recombination (GR), between electron-ion pairs created in different tracks. For high-LET radiation (ion beams) the contribution of IR becomes more important in LICs and it needs to be taken into account. Because IR is related to single track processes, it is LET dependent and, thus, offers the possibility to relate the IR processes to LET. However, because the GR and IR processes are always coupled, one first needs to evaluate separately how GR and IR losses affect the overall signal.

Unfortunately, a theoretical modeling describing how IR depends on LET remains, for the time being, still an ambitious goal. However, we developed a method which can relate, in real time, IR to a Monte Carlo simulated LET, by using both a LIC and an IC, coupled very closely together, so as to monitor at least nearly the same position of the beam. With this apparatus the physical depth dose distribution in water with the LIC and the IC can simultaneously be measured, and hence, the ratio between the two curves can be determined. The IC and the LIC readings are affected by GR and IR in different ways, therefore the LIC IR losses can be identified and this ratio can directly be related to the calculated LET of the particles in the measuring point. This procedure provides a calibration curve, where the LET at each depth can be identified from a certain ratio value. The rational of this methodology is based on the different way recombination affects the charge collection in a gas versus a liquid medium. ICs have small initial recombination effects even when irradiated with high-LET particles; therefore the measured signal is closely related to the LET and any signal/LET dependency can be neglected to first order. LICs, on the other hand, exhibit a much higher signal variation dependent on LET due to the small electron thermalization distances in liquids.

The ratio values are independent on variations in the dose of the beam if both, the IC and the LIC measurements, are carried out simultaneously or if the conditions of irradiation are repeatable (i.e. coupled system of ionization chambers).

The thesis is structured as follows:

- Chapter 1: basic principles of radiotherapy, with a particular focus on hadrontherapy, and definition of the main quantities;
- Chapter 2: general overview of the most widely used detectors for radiotherapy and detailed description of liquid ionization chambers, the various theories of recombination and the correction methods present in literature, description of the detector used, the 2D-array;
- Chapter 3: experimental setup and the different radiation sources used in our studies, experimental results concerning the 2D-array characterization and the LET measurement;
- Discussion and conclusion

AIM OF THE THESIS

Chapter 1

Radiotherapy

Cancer is one of the most significant causes of death worldwide.

The World Cancer Research Fund (WCRF) International estimated the number of world cancer cases to be about 12.7 million in 2008, increasing to 21 million by 2030 [61]. The most common cancer type is lung cancer, contributing nearly 13% of the total number of new cases diagnosed in 2008, followed by breast cancer with nearly 1.4 million new cases in 2008.

Different treatment modalities may be employed to treat cancer: the most-used are surgery, chemotherapy and radiation therapy, depending on the characteristics of each tumor and on the strategy chosen by the medical team. In many cases, the surgical removal of a tumor is still the most efficient approach, especially when the tumor is well-defined and compact. Sometimes, unfortunately, the tumor may be located in proximity of important organs at risk (e.g., close to the spinal cord or in the eye) or in areas which can not be reached through surgery (e.g., head tumors), or the tumor may have microscopic ramifications spread over a wider area. In these cases, surgery can not be performed and radiotherapy may be the best choice. Radiation therapy is widely used to cure brain, head and neck, lung, prostate, pancreatic and eye cancers. When the tumor begins to spread throughout the body, called the "metastatic phase", chemotherapy becomes the most effective approach. Usually, however, combinations of different treatments are used to fight a cancer, especially if the clinical picture is complex.

For this reason, not only a better understanding of tumor growth and development mechanisms is required, but also the demand for improving radiotherapy and targeted drug delivery techniques has grown.

In this chapter the main features of radiation therapy are covered, and therapies using photons and electrons ("conventional radiotherapy") are compared to heavy charged particles (protons and heavy ions).

1.1 Interaction of ionizing radiation with matter: the basis of radiotherapy

The use of heavy charged particles (protons and heavy ions) to treat cancer was first proposed by Robert Wilson in 1946 [63]. He reasoned that the shape of the energy deposition as a function of depth associated with charged particles would be advantageous when compared to photons and electrons (fig. 1.1).

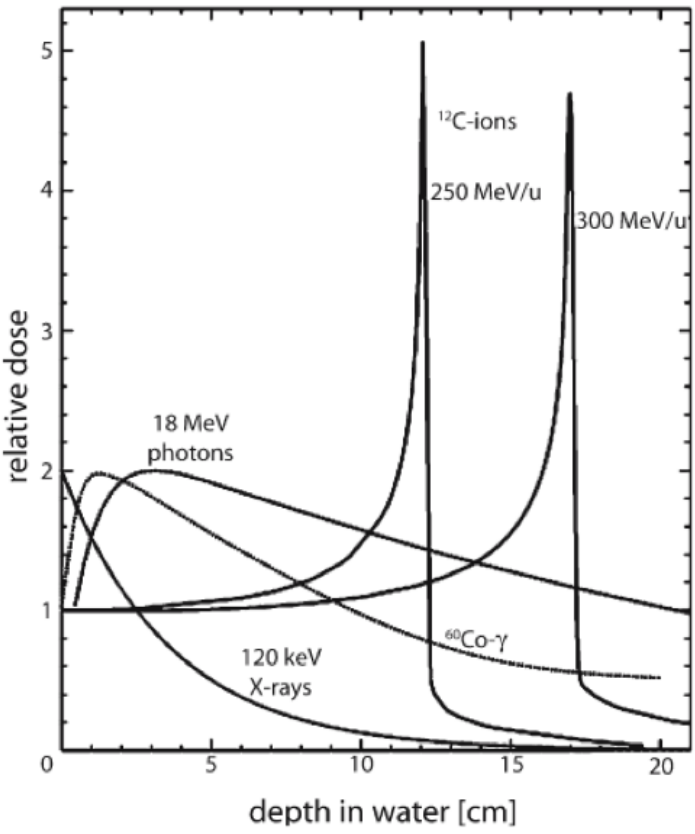

Figure 1.1: Depth dose profiles in water for various radiation types: photons from different radiation sources and carbon ions ([62]), at two different energies. The position of the Bragg peak is energy dependent.

Photons and X-rays deposit the highest amount of energy (the concept of dose will be defined later in this chapter) just beneath the skin, and are therefore rather inefficient if the tumor is embedded deep in the tissue. Heavy charged particles, however, are able to travel through the tissue releasing a small amount of energy in the entrance region and delivering the highest

amount at the end of their track, in the so-called Bragg peak. By varying the ion beam energy, the position of the Bragg peak can be adjusted and precisely located at the desired depth, which is within the tumor. In addition, heavy ions, like carbon and oxygen, exhibit higher biological effectiveness than protons, due to the different amount of charge carried by the ions, a property which varies with ion type.

As interaction between matter and radiation depends on the latter's nature, a distinction between interactions of light particles (mainly X-rays) and heavy ions will be given in the next paragraphs.

1.1.1 Photon interactions

Photons traveling into matter lose their energy in the medium through three different processes: Compton scattering, photoelectric effect and pair production. In these processes, the photon releases all or part of its energy to the atomic electrons of the absorber, which are then removed from their atomic orbitals or promoted from their ground state to a higher energy state, leading the atoms to a state of ionization or excitation:

- in the Compton scattering the photon is inelastically scattered by an atomic electron and it emerges with a lower energy. The energy difference is transferred to the scattered electron;
- in the photoelectric effect the photon is absorbed by one atomic electron which is then ejected by the atom;
- in the pair production one high-energy photon is transformed into an electron-positron pair.

The secondary electrons (also called δ-electrons) released through these processes cause secondary ionizations in the surrounding atoms and they are responsible for the energy transfer to the tissue. In figure 1.2, the relative importance of the three effects depending on the energy is shown: with the increase of the photon energy, the dominant interaction channel goes from photoionization to Compton to pair production.

In particular, at the therapeutically relevant energies for radiotherapy (5 - 25 MeV), Compton scattering dominates.

1.1.2 Charged-particle interactions

When a charged-particle travels trough matter its Coulomb field interacts with the electrons and the nuclei of the atoms of the target material. Along

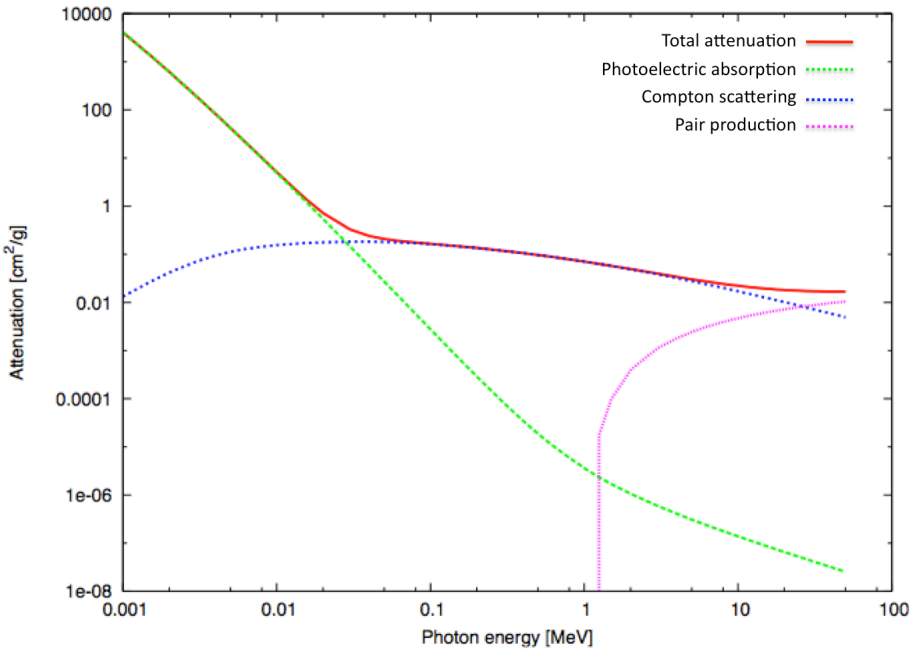

Figure 1.2: Contribution of Compton effect, photoelectric effect and pair production for photons to the attenuation curve in water [54].

its path, it loses its kinetic energy via excitation, ionization and radiative loss (bremsstrahlung) processes. In general, the passage of charged particles through matter is characterized by two phenomena: their energy loss and their deflection from the original trajectory [44]. Heavy charged particles typically transfer only a small amount of their energy in one single electronic collision, losing energy almost continuously in many different collision events with the atomic electrons (for a 1 MeV particle, this happens in about 10^5 events) before they come to rest, leaving ionized and excited atoms behind. The Continuous Slowing Down Approximation (CSDA) is based on this assumption and it is used to calculate the CSDA ranges, a close approximation to the average path length traveled by a charged particle as it slows down to rest (fig. 1.3).

The energy losses per unit path length of charged particles are described by the stopping power, given in $keV/\mu m$. Three different terms contribute to the total stopping power:

$$-\left(\frac{dE}{dx}\right) = \left(\frac{dE}{dx}\right)_{el} + \left(\frac{dE}{dx}\right)_{nucl} + \left(\frac{dE}{dx}\right)_{rad} \tag{1.1}$$

The first term is the electronic stopping power, defined as the average rate

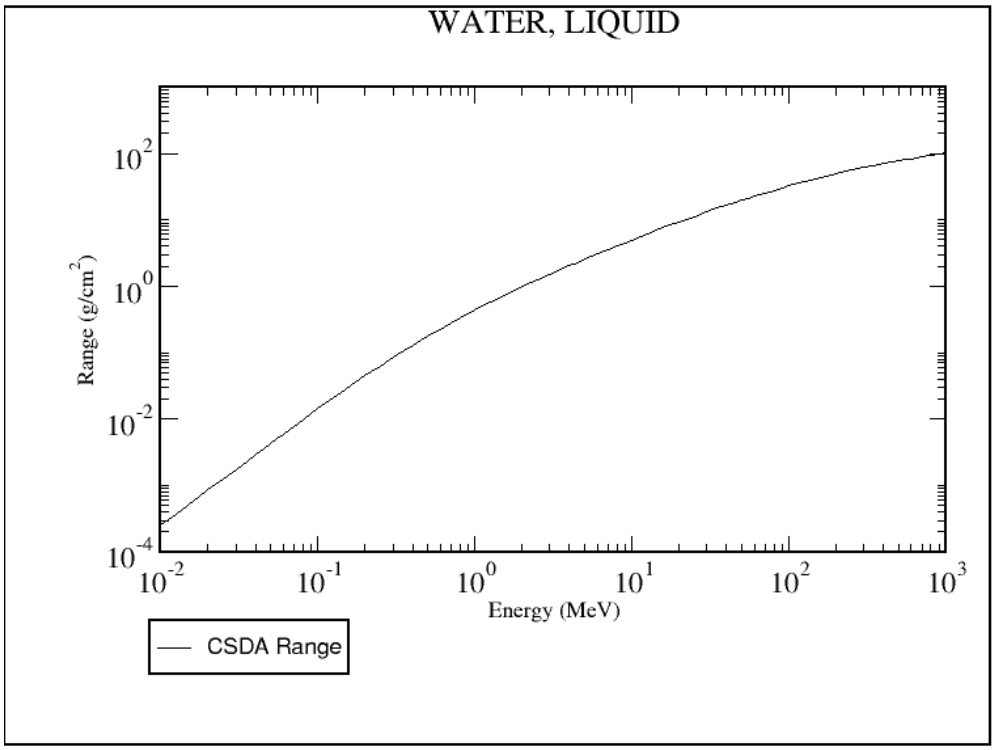

Figure 1.3: CSDA range of electrons in water [101].

of energy loss per unit path length due to Coulomb interactions with the target electrons; the second term is the nuclear stopping power, which is the average rate of energy loss per unit path length due to elastic Coulomb collisions with atomic nuclei; the third term is the radiative stopping power, the average rate of energy loss per unit path length due to bremsstrahlung [56], only relevant for electrons.

Often, the mass stopping power is considered, which is the stopping power divided by the density of the target material ρ. The reason for this is that it is nearly independent of the density of the actual material (except for the polarization effect [87]), which is useful when different kind of tissues are present, since it takes into account their heterogeneities. It is usually given in $MeV \cdot cm^2/g$.

The Bethe-Bloch formula

The electronic stopping power is approximated by the Bethe-Bloch equation, formulated in relativistic terms by Bethe in 1932 [43]. For the therapeutically relevant energies, it is described as:

$$-\left(\frac{dE}{dx}\right) = 2\pi r_e^2 m_e c^2 N_e \frac{Z^2}{\beta^2}\left[ln\frac{2m_e c^2\beta^2 W_{\max}}{I^2(1-\beta^2)} - 2\beta^2 - 2\frac{C}{Z_t} - \delta\right] \quad (1.2)$$

where r_e and m_e are the classical electron radius and rest mass, N_e is the electron density, Z the projectile charge (in units of electron charge), β=v/c, where c is the velocity of light and v the speed of the incident particle, W_{max} the largest possible energy lost in a single collision, I the mean excitation potential of the medium, Z_t is the atomic number of the medium and $\delta/2$ is a density-effect correction. C/Z_t is the shell correction term, which accounts for the internal structure of the target atoms and plays a role only for low energies, in the order of a few MeV/u. Neglecting the $2C/Z_t$ term, equation 1.2 describes the mean rate of energy loss in the region $0.1 \lesssim \beta\gamma \lesssim 1000$ for intermediate-Z_t materials within an accuracy of a few % (here, γ is the relativistic factor). The symbols $\lesssim$ are used because these limits of validity depend on both the effective atomic number of the absorber and the mass of the slowing particle. To extend the lower limit down to $\beta \approx 0.05$ (when the projectile velocity becomes comparable to atomic electron velocities) the shell correction term $2C/Z_t$ has to be included to take into account the atomic binding. This correction decreases very rapidly with increasing energy. At the upper limit, radiative effects begin to be important.

The average loss of energy is dominated by the term $1/\beta^2$ $\approx$1/E, thus showing a characteristic energy dependence: the energy loss rate increases

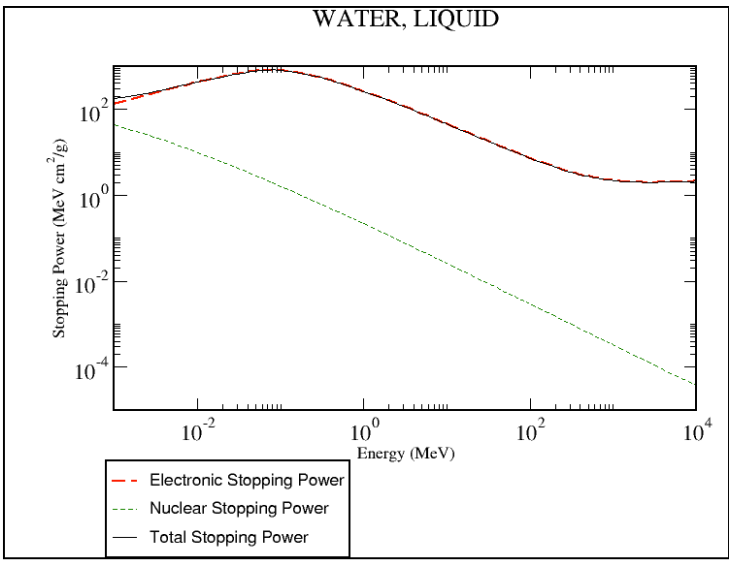

Figure 1.4: Total, electronic and nuclear stopping power of protons in water [45].

as the kinetic energy of the particle diminishes along the penetration depth, with a much steeper rise at low residual energy values corresponding to the last few millimeters of the particle path. The faster the ion is, the smaller is the interaction probability with the atoms of the medium. The energy loss is also independent of the ion mass. In the track end, the electronic stopping power drops down also because, at low energies, Z decreases fast due to increasing cross sections for electron capture by the projectile and the energy loss reaches a maximum at ion velocities that are comparable to the velocity of the orbital electrons. To consider the loss and capture of the electrons from the target, Z is replaced by Z_{eff}. In general, Z_{eff} is not equal to the ionic atomic number, as it depends on the ion energy and on the medium. The charge of the ion decreases at low energies due to the electronic capture. There is not a theoretical universally accepted method to describe Z_{eff} in all the media, but semiempirical formulas are used.

Z_{eff} is well approximated by the Barkas equation [60]:

$$Z_{eff} = Z\left(1 - e^{-a\beta Z^{-\frac{2}{3}}}\right) \tag{1.3}$$

with $a = 125$. When the corrections are properly included, the Bethe formula is accurate to about 1% down to $\beta \approx 0.05$, or ~ 1 MeV for protons. For $0.01 < \beta < 0.05$, there is no satisfactory general theory describing the energy loss in matter [65].

Energy and range straggling

By integrating equation 1.2 one finds the CSDA range (R_{CSDA}) for a particle which looses energy only through ionization and atomic excitation, i.e. by electronic energy loss. The R_{CSDA} is defined as the expectation value of the pathlength that a charged particle follows until it comes to rest. It is related to the mass stopping power by:

$$R = \int_{E_0}^{0} \left(\frac{dE}{\rho dx} \right)^{-1} dE \tag{1.4}$$

where E_0 is a given initial energy, $\frac{dE}{dx}$ is the stopping power and R is expressed g/cm^2 (it can be converted into length by dividing by the density of the target material).

For example, the electron R_{CSDA} in water is represented in figure 1.3. Delta electrons, produced via ionizations by the heavy-ion beam, have a kinetic energy of only few eV, because part of that energy is spent in overcoming the electron binding energy.

Eq. 1.4 is an approximation of the length of the average distance travelled by an ion in a material. However, when a beam of charged particles enters the matter, instead of a single one, it becomes clear that not all the particles have the same fate concerning interaction events. Instead, the energy lost in each collision between the nuclei and the electrons undergoes statistical fluctuations and two particles with the same initial energies will most probably differ slightly in their penetration depth. Such fluctuations in the case of charged particles passing through a thin layer of matter are described by an asymmetric distribution [67], but in the limit of many collisions the distribution can be assumed as Gaussian [59]. The width of the range straggling is:

$$\sigma_R = \frac{R}{\sqrt{m}} f \left(\frac{E}{mc^2} \right) \tag{1.5}$$

where m and E are the projectile's mass and energy, respectively, and f is a slowly varying function depending on the absorber [68]. From the $1/\sqrt{m}$ dependence it is clear that straggling is smaller for heavier ions than for protons (i.e., factor 3.5 for carbon ions).

As a result, a beam of identical particles, having all the same initial conditions, at each depth has a distribution of energy and of ranges. These two phenomena are called, respectively, energy straggling and range straggling, and they are responsible for the broadening of the Bragg peak of a particle beam compared to the one of a single particle, that would have a very sharp

peak near the stopping point, as described by equation 1.2.

The range straggling increases with the penetration depth in matter: as consequence, for a given ion type, Bragg peaks with higher initial energies have larger width. At the same time, the Bragg peak becomes smaller with the increase of the beam energy, which is due to the nuclear reactions taking place along the trajectory [58].

Multiple Coulomb scattering

A charged particle traveling in matter undergoes multiple elastic collisions with the atomic nuclei along its path. This effect is called multiple Coulomb scattering and it is responsible for the statistical deviations of the particle from its most likely path due to the repeated small-angle nuclear scattering events, which makes the total distance traveled longer than the particle's total depth of penetration [59]: this results into a spread and a divergence of the beam in depth. The whole theory of multiple Coulomb scatting is comprehensively covered in [64], but good estimates are usually given by empirical formulae. The lateral spread and the divergence of the beam lead to a certain angular distribution with respect to the incident direction and the central part of such a distribution contains very small angles ($<10°$) and is approximately gaussian, due to the statistical repetition of multiple scattering events at small angle deflections. In this case, the angular density distribution can be characterized by its mean and its standard deviation. A good approximation of the standard deviation σ is given by the empirical formula [66]:

$$\sigma = \frac{13.6\frac{MeV}{c}}{\beta p}\sqrt{\frac{l}{X}}\left[1 + 0.038ln\frac{l}{X}\right] \tag{1.6}$$

where p is the momentum of the particle, X and l are given in g/cm^2 and are the medium's radiation length [1] [114] and path length, respectively. From equation 1.6 follows that the effect of multiple Coulomb scattering increases as the particle energy decreases.

Fragmentation of the projectile

Heavy charged particles traveling through the matter may also interact with the nuclei of the absorber atoms via nuclear reactions, which are responsible for fragmentation processes. They strongly characterize the radiation field, acquiring more importance with the increase of the penetration depth.

[1] defined as the mean length to reduce the energy of an electron by the factor 1/e.

Such processes can be explained through the abration-ablation model [69], illustrated in figure 1.5, which is schematized as a two-step process.

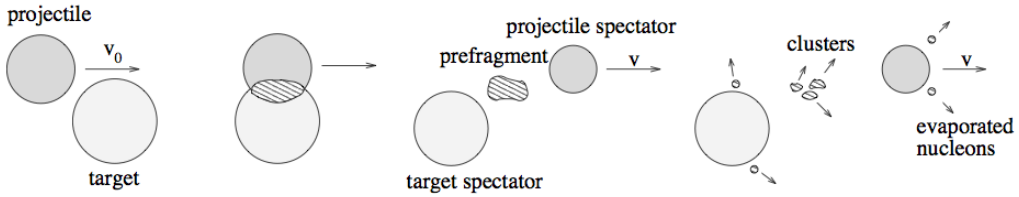

Figure 1.5: Schematization of a nuclear reaction depending on the abration-ablation model [119].

High-energy particles travel approximately on a straight line across the target and, when they collide with a nucleus, they give rise to the so-called pre-fragment, formed by those nucleons abraded in the overlapping area between the projectile and the target nuclei. After the collision, the outer nucleons of both the projectile and the target are almost not affected by this collision, with the projectile spectator nucleus emerging with nearly the same velocity and direction, while the target spectators staying at rest. This is the first step: it is a fast process (about 10^{-23} s) and gives rise to highly excited pre-fragments. In the second step, such excited pre-fragments de-excite by emitting different kind of particles (neutrons, protons, gammas and small clusters). What remains from such emission are lighter ions (α, deuteron and triton) and single nucleons. This second step is called evaporation and its typical times are 10^{-16} - 10^{-18} s. While projectile-like clusters are emitted in a forward direction with respect to the mass center and contribute to the dose deposition until they are completely stopped, neutrons and clusters from target-like fragments are emitted isotropically in the center of mass and with lower velocities. Due to the A/Z^2 dependence of the range (A is the nucleon mass), lighter fragments can travel beyond the range of the primaries, resulting in the characteristic fragmentation tail behind the Bragg peak of ion beams. As a consequence of these nuclear reactions, the fluence distribution of the primary particles can be approximated as being exponentially attenuated in depth x according to the expression:

$$\Phi(x) = \Phi_0 e^{-N\sigma_R x} \tag{1.7}$$

where Φ_0 is the initial fluence, N is the atomic density of the medium and σ_R is the total reaction cross section. From equation 1.7 and taking into account that the dose is proportional to the fluence (as it will be explained in the next paragraph), it follows that the dose delivered by the primary ions

is reduced with increasing depth due to nuclear reactions. Together with the attenuation of the primaries (important for heavier ions), also secondary nucleons, particles and fragments produced in nuclear reactions strongly affect the energy deposition patterns (nuclear recoils contribute only negligibly [70]).

As represented in figure 1.6, the number of primary particles decrease with the depth and, at the same time, the number of fragments increases.

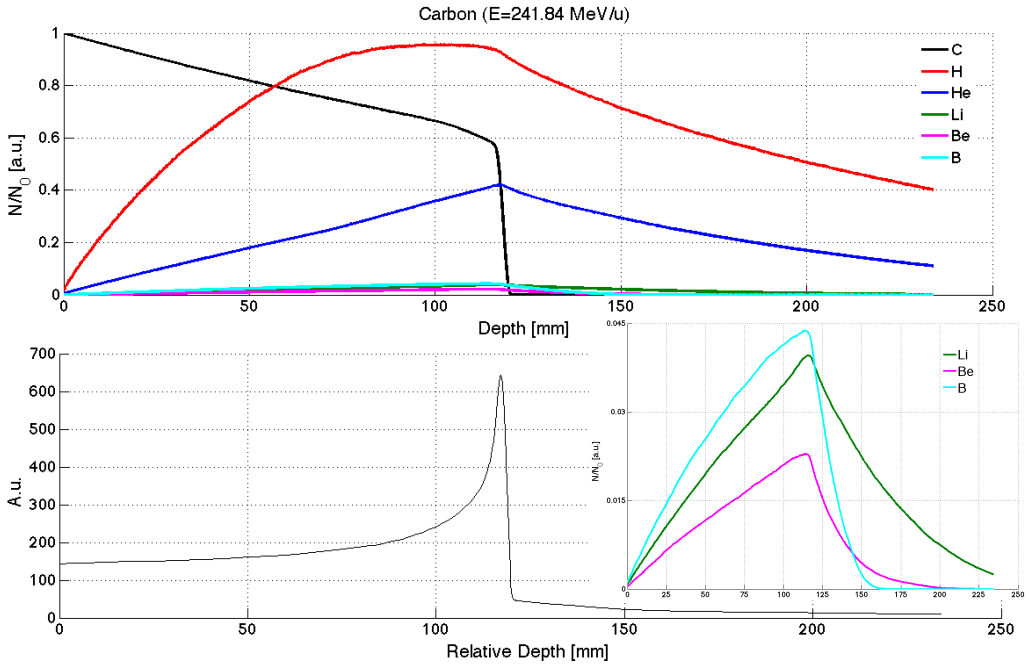

Figure 1.6: Simulated contributions of primary and secondary particles (upper figure) for the ^{12}C Bragg curve of a beam of energy 241.84 MeV/u (lower figure). The insertion in the lower figure shows a zoom of the heavier fragments depicted in the upper figure. (*Courtesy of A.Mairani)*

During fragmentation processes the primary ions can be stripped of one or two neutrons and they turn into the positron-emitting isotopes ^{11}C and ^{10}C, with half lives of 20 minutes and 19 seconds, respectively. This offers the possibility to perform the Positron Emission Tomography (PET): when the isotopes decay, they emit positrons, which annihilate with electrons, giving rise to two gammas, that escape back-to-back, because of momentum and energy conservation. By their coincident detection via a PET camera, the spatial β^+-activity distribution in the patient can be reconstructed and subsequently compared to the intensity distribution calculated by the treatment plan, resulting in an important tool to verify the treatment.

1.2 Absorbed Dose

The primary physical quantity in dosimetry is the Dose (D), defined as the mean energy $d\epsilon$ deposited by ionizing radiation in a mass element dm [71]:

$$D = \frac{d\epsilon}{dm} \tag{1.8}$$

Dose is measured in Gray (Gy):

$$1Gy = 1\frac{J}{kg} \tag{1.9}$$

For beams broad enough to ensure lateral secondary electron equilibrium, which is normally the case, the deposited energy is relative insensitive to variations in local density and field size. Charged particle equilibrium (CPE) exists for a defined volume if each charged particle of a given type and energy leaving the volume is replaced by an identical particle entering. CPE is not always fulfilled: an example is the build-up region in a photon beam, where the dose builds-up to a maximum and then reduces with depth. If CPE is verified, the dose D in one defined volume can also be expressed in terms of particle fluence ϕ of monoenergetic ions (number of primary ions per cm^2) and the average energy loss dE/dx:

$$D[Gy] = 1.6 \cdot 10^{-9} \frac{dE}{dx} \cdot [keV/\mu m] \cdot \phi \ [cm^{-2}] \cdot \frac{1}{\rho} \ [cm^3/g] \tag{1.10}$$

where $\frac{dE}{dx}$ is the stopping power and ρ the density of the stopping material. As the stopping power describes the energy lost by the traveling particle, dose is related to the specific energy pattern deposited by the primaries.

1.3 Linear Energy Transfer (LET)

The concept of Linear Energy Transfer (LET) was introduced in the early 1950s to describe the quality of radiation and it represents the rate at which energy is deposited by the ionizing particles [18]. In such terms, LET and stopping power represent the same quantity. Nevertheless, the interest in discriminating between the energy transferred by the particle and the one which is effectively deposited in the area of interest lead to the adoption of the term *restricted linear collision stopping power* [46]. In 1962 the International Commission on Radiation Units and Measurements (ICRU) introduced the adjective "locally" to the energy imparted to a medium, but, again, the

definition was not quite strict and LET was not always used with the same meaning. Finally, in 1980, the ICRU defined LET as:

$$L_\Delta = \left(\frac{dE}{dl}\right)_\Delta \tag{1.11}$$

where dl is the distance traversed by the particle and dE is the mean energy loss due to those collisions which have an energy transfer smaller then a specified energy cut-off value Δ. For example, L_∞ means that all possible energy transfers are included and in this case the concept of non-restricted stopping power is used, while L_{100} means a cut-off value of 100 keV and it is referred to as restricted stopping power. In this case, those secondary electrons with more than 100 keV are not taken into account, as they leave the volume of interest around the primary particle track. LET is usually expressed in keV/μm.

LET, being a measure of the density of the ionization events along the particle track, is strongly related to the amount of biological damage inferred by a certain kind of radiation to biological tissue. The ultimate target for inducing cell death is its DNA molecule, which is enclosed in the cell nucleus and is holding all the genetic information of the cell. To inactivate the cell, its DNA must be irreparably damaged such that the cell looses its capacity to duplicate itself.

DNA damage can be direct, caused by the ion or its induced secondary electrons (30%, for low-LET radiation, slightly increased for high-LET radiation), or indirect, generated by radiation induced radicals (70%, for low-LET radiation). There exists a variety of DNA damages. Some are isolated DNA lesions, like single strand breaks ($SSBs$), damaged bases, and abasic sites, which can be generally repaired efficiently. Others are more closely spaced lesions, like double strand breaks ($DSBs$), two or more SSBs on opposing strands and other clustered damages, constituting lesions on both DNA strands, which are considered to be significantly harmful. When a complex damage is inferred, chromosome aberrations and cell death occurs in the DNA, as it has been modeled using Monte Carlo simulations ([72]). Monte Carlo techniques simulate radiation action and the damage inferred on the DNA molecule. Track structures characteristic of the radiation used are calculated in homogeneous media and the energy transfer patterns are determined and processed to derive SSBs and DSBs [88].

Low-LET and high-LET radiation have different efficiency in damaging the DNA and this is related to the spatial distribution of their energy deposition. If photons deposit energy homogeneously throughout the nucleus, ions deposit energy in well localized sites of the cell nucleus. In particular, they

deposit a very high dose in proximity of the particle track and essentially no energy in the areas in between the tracks, leading to a very inhomogeneous distribution of the local dose. The higher efficiency of high-LET radiation in damaging the DNA molecule is due to the short range of the electrons produced along the particle tracks, which causes them to stay in proximity of the particle trajectory (in the order of nanometers). The resulting particle track has a high ionization density along its trajectory and is therefore able to induce a considerable amount of complex lesions close to each other (less than one nanometer), which are difficult to be repaired. Instead, in case of low-LET radiation the average spacing between ionization events in the track is of the order of hundreds of nanometers: the interaction between products of different ionization events in a track is, therefore, negligible, and irreparable damage to the DNA is unlikely (instead, the interaction of events from different tracks is of importance). For this reason, same doses of carbon ions and X-rays have completely different effects at a biological level due to different events occurring at a microscopic level (fig. 1.7).

The track structure is related to energy, as the diameter of the particle track depends on the range of the produced electrons, and therefore on the ion energy. This can be qualitatively explained by considering the relation between energy and particle track along the particle path, for example, for carbon ions. At high energy the track is wide and LET is low, meaning that the ionization events are well separated one from the other. As long as the energy decreases, the track narrows and at the same time LET increases. With the increase of LET, the local density of produced damage increases, with a consequent enhancement of cell damage. At the very end of the track, the diameter shrinks and LET grows further: this is the overkill region, where the overproduced dose is wasted and no additional cell damage can be harmful [7].

Those ionization densities along the particle track matching the transversal length of the DNA molecule are the most efficient in generating irreparable damage to the tumor cells, as the probability to cause a complex damage to the DNA is higher. Within this context, the efficiency of different kinds of radiations is represented by the graph in figure 1.8. If LET is increased beyond an optimal value, there will be additional ionization events, but without any further increase of damage, and thus, effectiveness decreases. Therefore, since the deposited dose still increases with LET, the relative biological effectiveness will decrease, being defined as ratio of doses (see paragraph 1.4). This decrease at very high LET values is called overkill effect and occurs at typical LET values of 100-200 keV/μm.

Particle LET and energy alone are not the only parameters that govern the mechanism of damage formation in the cell, but there is a wide set of

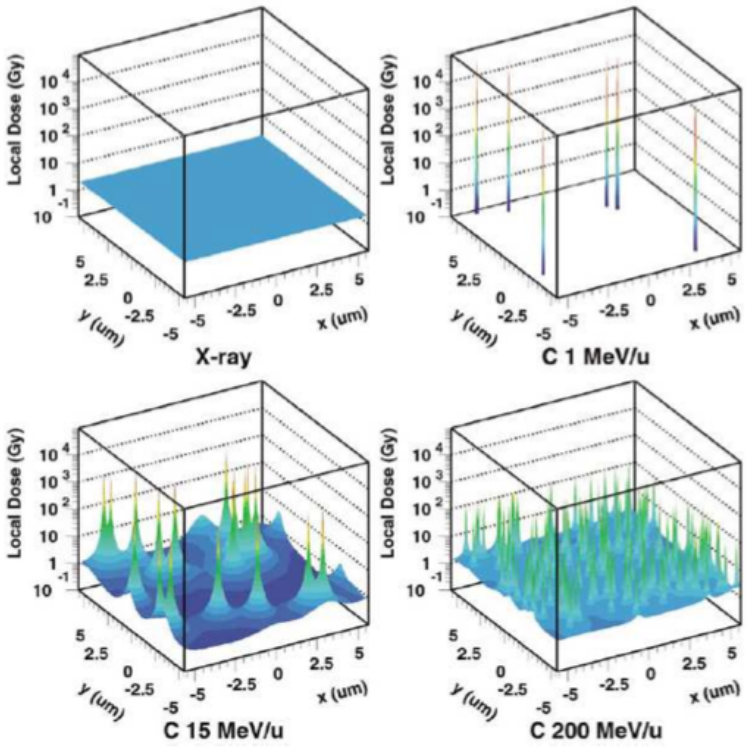

Figure 1.7: Illustration of the microscopic dose depositions of X-rays and carbon ions at different energies. The average dose is 2 Gy in all cases, but, as LET decrease with the energy increase, also the fluence increases. The size of the area is $10 \times 10\ \mu m^2$, a typical size of mammalian cell nuclei [74].

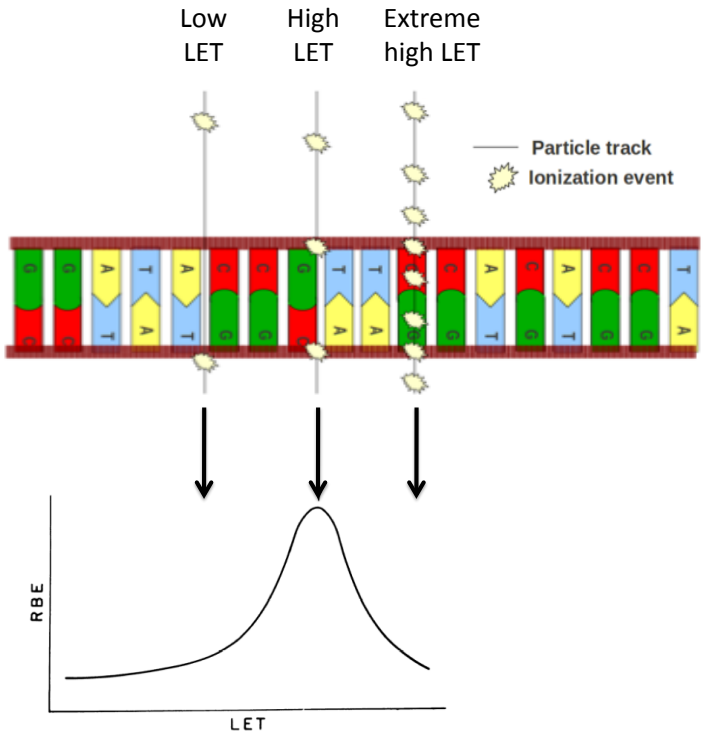

Figure 1.8: Schematic representation of the overkill effect: low-LET radiation has a low biological efficiency, while high-LET radiation corresponds to higher RBE values. Too high-LET radiation causes the so-called "overkill effect", as it deposits higher dose without a correspondent enhanced biological damage. The different LET levels are also schematically indicated in terms of density of ionization events along the particle track and correlated to their capability to cause DSBs in the DNA molecule. Adapted from [89].

.

factors which intervene in the response of a biological tissue under irradiation. These factors are of both, physical and biological nature and the interplay between them contribute to the overall radiobiological response of that tissue, as it will be discussed in section 1.4.

1.4 Relative Biological Effectiveness (RBE)

The motivation for using heavy ions in particle therapy is twofold: first of all, the Bragg peak dose deposition shape allows a more confined delivery of dose in correspondence of the tumor volume, sparing at the same time the surrounding healthy tissues. But, even more important, the radiobiological properties of ion beams make them more efficient in inducing damage in carcinogenic cells [48]. By tuning the beam energy, the high-efficiency portion of radiation, which for carbon ions occurs at the end, can be confined in the tumor volume, limiting in this way the damage inferred to the tissue in the entrance channel, where the biological effectiveness is lower.

To describe radiation in terms of its efficiency, the relative biological effectiveness (RBE) has been introduced. It is defined as the ratio of X- ray dose to particle dose to produce the same biological effect (fig. 1.9 [2]), which can be chosen to be an endpoint of, for example, 10 % survival rate:

$$RBE = \left.\frac{D_{X-Ray}}{D_{Particle}}\right|_{10\%} \tag{1.12}$$

The rationale behind comparing the particle dose to the photon dose is that most of the clinical experience is based on photon radiotherapy, therefore RBE correlates directly dose depositions of photons and heavy-ion radiation, giving a measure of the difference between them.

The usual way to analyze the effects of different radiation types is by means of cell survival curves. The most common relation between cell survival probability (S, i.e. the fraction of surviving cells) and absorbed dose (D) is the so-called linear-quadratic (LQ) model, that aims to predict survival levels at different doses for different types of radiation. According to the LQ model, RBE has an exponential linear quadratic dependence on dose, described by the relation:

$$S = S_0 e^{-\alpha D - \beta D^2} \tag{1.13}$$

Here:

- α represents the probability associated to lesions induced by a single track (SSB or DSB). It is expressed in Gy^{-1} and it is related to the

initial slope, it is caused by repairable damage to the target and dominates the radiation response at low doses;

- β the probability for lesions introduced by two or more tracks. It is expressed in Gy^{-2} and represents the irreparable damage and causes the curve to bend at higher doses.

The survival curve is represented in figure 1.9 [92].

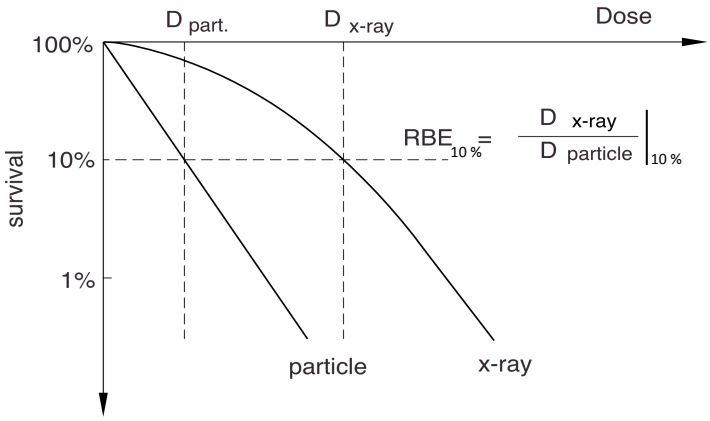

Figure 1.9: Definition of the relative biological effectiveness RBE, illustrated for cell survival curves ([2]).

The shape of the curve is determined by the α and β parameters, reflecting the kind of damage inferred to the cell. Low-LET radiation produces sparse lesions in the DNA, easy to repair via the cell repair mechanisms, while high-LET radiation damage is more difficult to repair. The increase of dose is related to a more complex cell damage: this trend is represented by the shape of the linear-quadratic curve.

RBE is used in treatment planning as weighting factor to obtain the biological dose (D_{bio}), as the physical dose (D_{phys}) alone does not consider the response of biological tissues to the radiation:

$$D_{bio} = RBE \cdot D_{phys} \tag{1.14}$$

The D_{bio}, instead, accounts for the increase of the biological effectiveness of ion beams towards the Bragg peak compared, for example, to the one of a proton beam: while for protons an RBE value of 1.1 is used in clinical practice (ICRU (2007)), the assignment of an RBE value at each depth for carbons is much more complicate. First of all, the RBE increase goes together with the LET increase, because of the higher density of ionization

events, causing more damage to the DNA. Moreover, the contribution of the secondary fragments produced along the path has to be included to have the final biological effect. The main physical parameters which characterize RBE are the ion species, the beam energy, the dose and the LET, while the main biological ones are the tissue type, the repair capability of the cell, the level of oxygenation of the tissue [48]. Due to its complex and multiple dependencies, RBE is not an easy quantity to evaluate experimentally: for this reason, the application of different biophysical models is necessary in treatment planning. These models give comparable results in terms of the RBE evaluation, but inaccuracy in the RBE determination is still a source of uncertainty in the prescription of biological dose in carbon therapy.

1.4.1 RBE dependencies

As RBE changes not only along the depth dose curve but also for the various ion species with different LET values, RBE is often given as a function of LET (fig. 1.10, left). RBE increases with LET until it reaches a maximum, corresponding to the optimum LET value. After this point, a further increase of LET will not be anymore beneficial to cell killing and the excessive energy will not produce any further cell damage (see fig. 1.8).

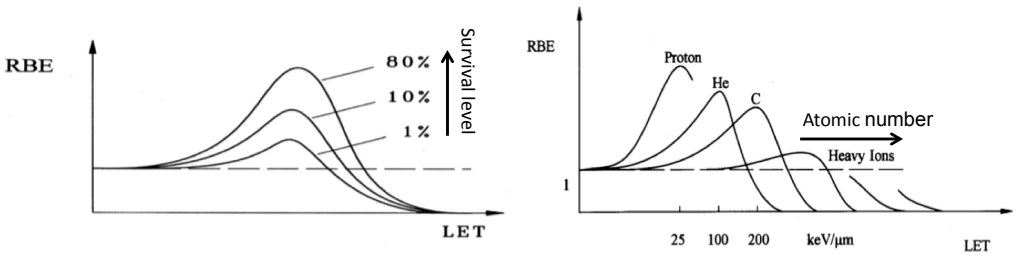

Figure 1.10: RBE as function of LET for a fixed atomic number: because of the dose dependence, RBE differs for different survival levels ($left$). Schematic comparison of RBE for different atomic numbers: for heavier ions the RBE maximum is shifted to larger LET values and decreased in height ($right$) [2].

Because of the dependence of RBE on dose, the fraction of survival has to be specified.
RBE also depends on the particle type (fig. 1.10, right): with the increase of the atomic number, the RBE maximum decreases and shifts to bigger LET values. These two dependencies show that the particle track plays a role in the biological efficiency of the various ions, because not only the initial

energy, but even more the particular way the particle interacts with matter, counts. On the other hand, for a given particle type, RBE depends on depth. For carbon ions, for example, at high energies, the track is wider and LET is low: the biological efficiency is therefore similar to the one of sparsely ionizing radiation. But as soon as the energy diminishes, the track shrinks and LET increases: as a result, the ionization density becomes higher and can cause more cell killing. Therefore, the increase of RBE is confined to the very end of the particle range. Further on, the diameter narrow even more, LET increases further and an overproduction of local damage takes place: this is the overkill region, mentioned before.

Another important element connected with the tissue quality is the repair capability. Tissues with high repair capacity have higher RBE maximum compared to those which have a lower repair capacity (fig. 1.11). This aspect has to be considered accurately in the treatment planning, as usually various tissues with different repair capacities are present. Moreover, also different endpoints are required, to guarantee an high efficiency of cell killing in correspondence of the tumor and a sparing of the surrounding healthy tissues.

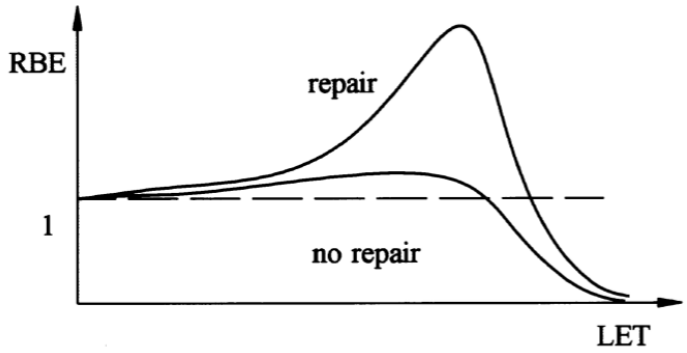

Figure 1.11: RBE as function of the linear energy transfer for cells with normal and reduced repair [2].

1.5 Conventional radiotherapy and particle therapy

From what has been discussed in the previous paragraphs, charged particle therapy can offer different advantages over conventional radiotherapy. First, the Bragg peak shaped dose deposition in depth (fig. 1.12) offers an advantage compared to photons for the treatment of deep seated tumors.

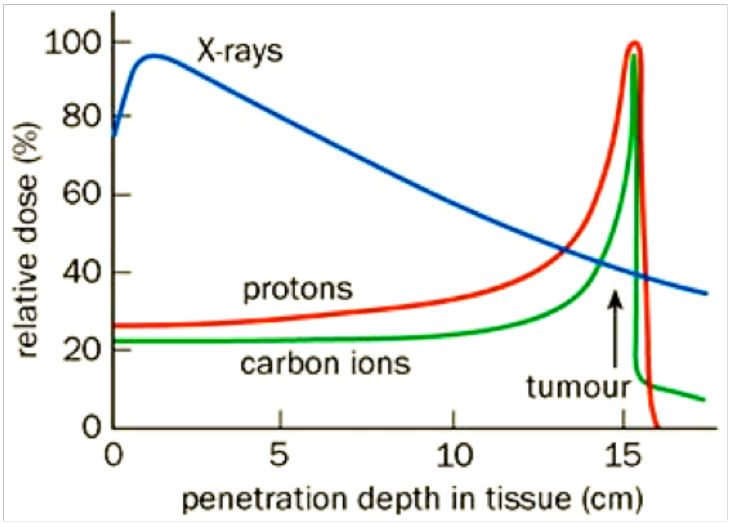

Figure 1.12: Comparison of typical depth dose distributions for X rays, proton and carbon ions.

Secondly, the RBE that characterizes heavy-ion beams is mainly due to a larger production of lethal DNA damages in the region of high local ionization density at the end of the ion track, which could be reached for photons only with an increased total dose.

In general, the gain in having an enhanced RBE is highest when the RBE and the Bragg maxima overlap sufficiently, allowing to have at the same time high dose and high RBE. RBE and the correspondent depth dose curves are represented in 1.13 for protons and two ion species, carbon and neon.

For lighter ions, like for protons, the RBE maximum is located at the distal edge of the Bragg peak: in this region, only few particles have not yet stop, due to the straggling and, consequently, the larger amount of dose has already been deposited. For this reason, the RBE for protons is clinically considered to be 1.1 ([55]), even though this practice has been now put in doubts but many authors [91], [93]. In fact, much higher RBE values are reported [93], but only restricted to the last sub-millimeters of range. Therefore, for the sake of simplicity in treatment planning, which includes RBE variations over the treated volume, a fixed clinical RBE is commonly adopted and currently used in proton therapy. For ions heavier than oxygen (like Ne in fig. 1.13) the RBE maximum is shifted with increasing atomic number towards the plateau region and the high-LET effects are shifted to the normal tissue, whereas the RBE in the Bragg peak already decreases in the overkill area. The situation is better for carbon ions, where RBE is low in the entrance region (compared to Ne ions) and it increases together

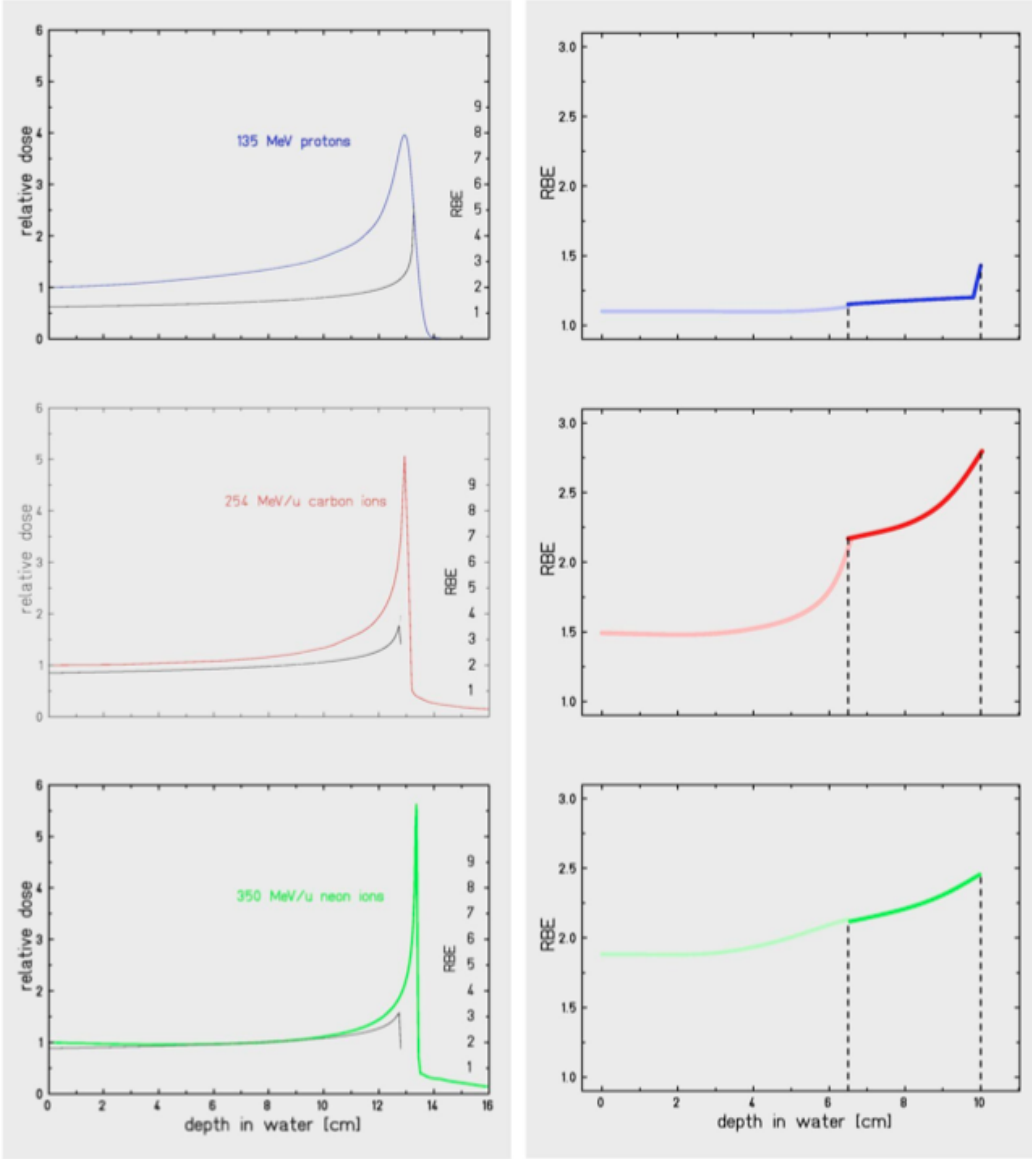

Figure 1.13: *Left*: comparison of the Bragg curves (in color for the left scale) and relative RBE (in black for the right scale). *Right*: RBE is given for extended Bragg curves (dose is not shown). The curves refer to CHO cells [90].

with the increase of the dose deposition peak. Neutron beams exhibit also high RBE values, however, due to their unfavorable depth dose distribution, RBE is high everywhere in depth, causing not only an enhanced biological efficiency in the tumor, but also normal tissue complications.

In addition to the greater RBE, carbon ion beams also have a smaller range straggling and lateral scattering [2], which translates into a more rapid lateral fall-off of dose compared to protons.

Single Bragg peaks are too sharp to treat the whole tumor volume, which has to be fully covered with a homogeneous dose deposition. Longitudinally, a *spread-out Bragg peak* (SOBP) must be built, by superimposing different single Bragg peaks (fig. 1.14):

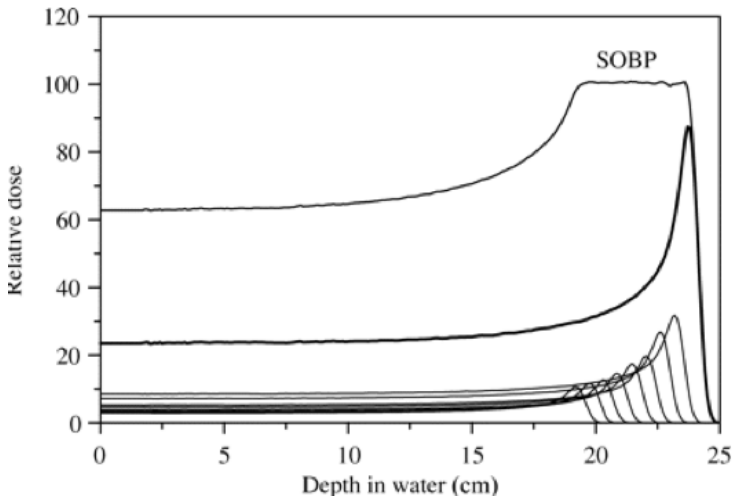

Figure 1.14: The superposition of suitably weighted particle beams of different energies results in a spread-out Bragg peak (SOBP) that provides a uniform depth dose over the target region [94].

This can be achieved by passive systems (by using, for example, range shifters of variable thickness) or active energy scanning (in this case, the energy of the particles is changed directly in the accelerator). For what concerns the lateral direction, a fully coverage of the tumor volume is obtained or by active beam scanning, or passively, with double scattering techniques, to expand the peak over a larger area. More details on these topics can be found in [2].

Chapter 2

Dosimetry: materials and methods

2.1 Detectors for radiotherapy

Dose measurement and control during patient treatment is an important requirement especially for hadron therapy, where the steep dose gradients need to be accurately controlled and the delivered dose has to be known very precisely over the whole tumor volume.

As discussed in [5], all the standard dosimetry is usually expressed in dose to water quantities, in part because of the historical development of treatment planning algorithms, in part because the treatment instrumentation is calibrated in terms of absorbed dose to water. The basic assumption is that, in first approximation, the human body is water, as water makes up the bulk of the volume of cells and body fluid [95].

An ideal dosimeter has to match a number of requirements:

- it should be energy independent: if the detector response to a given dose varies with the radiation beam energy, then a correction for this effect should be carried out;
- dose responce: the readings should be linearly proportional to dose;
- dose rate independence has to be fulfilled;
- accuracy and precision: it has to be able to correctly measure the dose and to reproduce the readings under similar short-term and long-term irradiation conditions;
- spatial resolution: ideally, it should be able to detect the dose with a resolution of less than a millimeter;

- tissue equivalence: an ideal detector should be as much tissue equivalent as possible, to match the medium where the dose is measured. If this is verified, the signal from the detector can be considered as being directly proportional to absorbed dose in tissue without the need to perform any correction.

Different kind of detectors can be used to measure the dose, but they all have some advantages and drawbacks:

- silicon diodes have a very small active volume and a high sensitivity, but they do not have an isotropical response and they are energy, dose rate, and temperature dependent;

- diamond detectors are nearly tissue equivalent, have a small sensitive volume and negligible directional dependence ([33]), but they are very expensive and dose rate dependent ([29]);

- thermoluminescent dosimeters (TLDs) are small, nearly tissue equivalent, but they have a non-linear dose response and they are energy dependent ([27]). Moreover, the read-out process is also relatively laborious;

- alanine detectors are small, but due to the low sensitivity, the pellets with which acceptable radiotherapy level dosimetry is achieved are usually quite large (typically, 5 mm diameter and 2.5 mm thick) and, thus, prone to substantial volume averaging. Moreover, the read-out process is time consuming ([26]).

- radiographic and radiochromic films have a high spatial resolution, they are nearly tissue equivalent and they are very thin, therefore they perturb only negligibly the beam, but they are light sensitive, they present energy dependency problems and variations between different types of film and different batches of the same film. The scanning procedure is usually time consuming and complex ([25]).

2.2 Ionization chambers

Ionization chambers (IC) are the most widely used detectors in radiotherapy [17]. They are composed of two electrodes, separated by a volume filled with a gas or a liquid (fig. 2.1). The working principle of an IC is illustrated in figure 2.1.

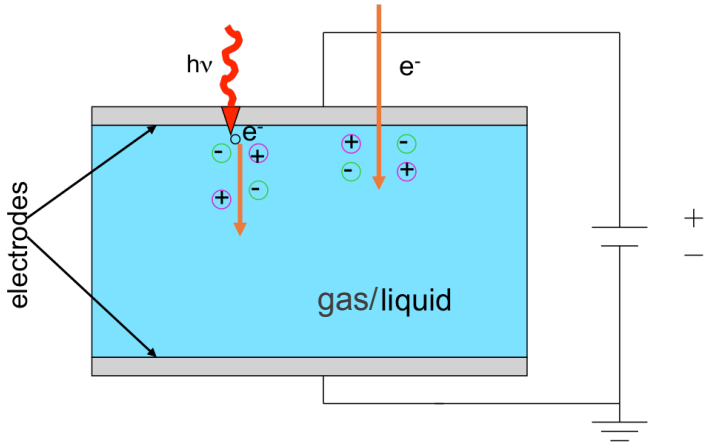

Figure 2.1: Working principle of a ionization chamber with parallel-plate geometry, filled with gas or liquid: the beam (in this case, photons and electrons) is impinging on the chamber and it produces ionizations in the medium. Ions and electron produced are collected at the electrodes by applying an electric field between them.

When a charged particle passes through it, it produces ionizations and excitations of molecules along its track. After a neutral molecule is ionized, the resulting positive ion and free electron form an electron-ion pair. These ionization events can be directly produced by primary particles or by the secondary electrons created through collisions with gas/liquid molecules.

An important quantity in dosimetry is the energy required from ionizing radiation to form an electron-ion pair in the active volume of a ionization chamber. Therefore, a lot of studies in radiation chemistry and dosimetry aim at the estimation of the energy required to form electron-ion pairs. The mean energy required in a gas to form an ion pair, W, is given by:

$$W = \frac{E}{N} \tag{2.1}$$

where N the mean number of electron-ion pairs formed when the initial kinetic energy E of a charged particle is completely dissipated in the gas ([97]). It is expressed in $[J]$ or in $[eV]$.

The definition of W is strictly valid for indirectly ionizing radiation or when all the energy is dissipated in the gas volume. For protons, instead, as they may loose only a fraction of their energy in the gas volume, the concept of a differential value, $w(E)$, is more appropriate [96], because the variation of the mean energy expended per ion pair along the path of the particle becomes important. The relationship between w and W is given by:

$$W(E) = \frac{E}{\int_I^E \frac{dE'}{w(E')}} \tag{2.2}$$

where I is the ionization threshold energy of the gas. Knowledge of w(E) over the whole energy range from I to E is necessary to derive W(E).

Through the application of an electric field, the charges created by direct and indirect ionization within the gas are collected. The response of the IC depends, therefore, not only on the radiation properties, but also on the applied voltage, because a lower voltage will allow a larger fraction of the electron-ion pairs produced in the medium to recombine before they could be collected at the electrodes.

The charge counted by the chamber differs from the one actually created in the sensitive volume by radiation, because different types of processes can happen between free electrons, ions and neutral gas molecules (fig. 2.2):

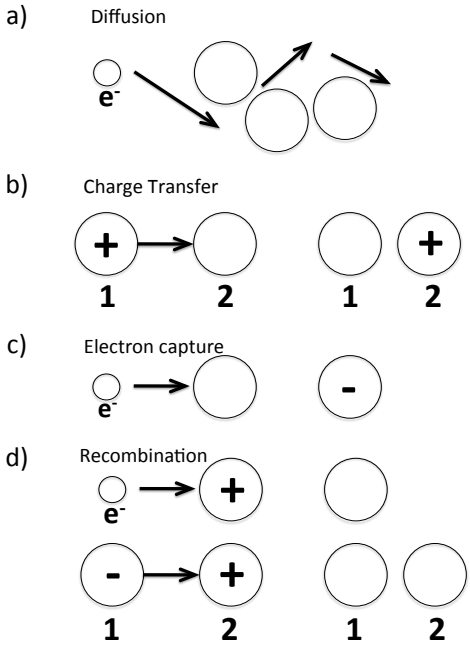

Figure 2.2: Collisions between free electrons (small circles), ions (large circles with + or -) and neutral gas molecules (large circles).

- diffusion: thermal diffusion of electrons and ions against the applied electric field towards regions with less concentration of charge, as a result of the Brownian motion. It is much more important for free

electrons, due to their higher thermal velocity. Diffusion plays a certain role in gases, where electrons are free to drift, but in liquids, due to the small mean free path and low charge carriers mobilities [12], it does not need to be taken into account (fig. 2.2a).

- charge transfer: a positive ion collides with a neutral molecule. In the collision, one electron is stripped from the neutral molecule and it is captured by the ion (fig. 2.2b).

- electronic capture: a neutral molecule collides with an electron. In the collision, the electron is captured by the neutral molecule, which becomes negatively charged (fig. 2.2c). Such effects are important in a medium with a high concentration of electronegative impurities, responsible for absorbing electrons present in the medium;

- recombination: it can involve a free electron and a positive ion, or a negative ion and a positive ion. In both cases, the electron (or additional electron, respectively) recombine with the positive ion, and both positive and negative charged parts are neutralized.

Ionization chambers filled with a liquid instead of a gas offer a number of advantages [15]. Due to the higher density of the liquid, the sensitive volume can be built much smaller, providing the same sensitivity of an air-filled chamber with a larger volume. In this way, a better spatial resolution with respect to ICs can be achieved. This is particularly appealing in modern X-ray therapy (IMRT) and in ion therapy, where steep dose gradients are present and the dose needs to be accurately monitored. The liquid filled chambers are water equivalent, therefore no air-density correction is needed and they do not significantly perturb the radiation field for in-water measurements. They have a long-term stability [16], as the liquid is not prone to aging or degradation, compared for example to diodes. Finally, they have small directional dependency.

However, along with these advantages comes at least one significant drawback: the distance between ions formed in the track of an ionizing particle is much shorter than in gas; therefore recombination in the liquid is much more pronounced. The higher amount of recombination is not only due to the high ionization density, but also to the low ion mobility in the liquid, which increases the probability that ions will recombine before being collected.

2.3 Recombination in ionization chambers

Recombination in ionization chambers can be classified to be general or initial.

- Initial recombination (IR, also called geminate recombination) takes place in the first tens of nanoseconds along one single particle track. It is usually considered negligible in ICs in low-LET regimes and it becomes more important for high-LET radiation. In LICs, however, this effect is much more relevant, because the mass density of liquid hydrocarbons is almost three orders of magnitude higher than the density of gases at normal conditions, and therefore the electron thermalization distances are much smaller. In the track of a highly energetic particle, ions are formed in clusters containing one or a few electron-ion pairs. Frequently, in fact, a primary ionization is accompanied by one or more secondary ionizations and gives rise to ion clusters containing one or more ion pairs (cluster probability for more than 6 electron-ion pairs is less than 4%)[98]. In very densely ionizing radiation, the successive clusters overlap to form a column of electron-ion pairs rather than a series of discrete clusters [99]. IR depends on the liquid properties, on its temperature, T, and on the external electric field, E, but not on the dose rate. By definition, it is obvious that it depends also on the density of ionization events along the track and, hence, on LET. Therefore, IR is related to the energy transferred "locally" by one single incident particle to the medium.

- General recombination (GR, also called volume recombination) is between different tracks: the electrons who escaped from initial recombination flow due to drift and diffusion and this makes possible the interaction between ions and electrons originating from different ionizing particles. GR depends, therefore, on the rate by which incident particle tracks are created, i.e. on the dose rate, on the liquid properties and on the collecting electric field.

Both IR and GR also depend on the ion mobility. Charge loss due to diffusion against the electric field has a low probability of occurring and is generally considered negligible.

2.3.1 Initial recombination

The IR processes can be distinguished in:

- geminate recombination: involving one electron and its mother ion. It is described e.g. by the Onsager theory;
- cluster recombination: between electron-ion pairs belonging to the same cluster, composed by different charge carriers (inter-cluster recombination). It is described by the Kara-Michailova and Lea theory. This process is not treated here;
- columnar recombination: clusters formed along the same track of one individual ionizing particle begin to expand due to ionic and electronic diffusion and they start to overlap. Such an intra-cluster recombination taking place between different clusters is described by the Jaffè theory.

These processes are not completely independent of each the other, but rather there is partial overlap between them, which makes the classification scheme above somewhat arbitrary. Nevertheless, it is convenient to continue using this classification, as each group is treated by different theoretical models.

The Onsager Theory

In 1938 Onsager described recombination taking place between one electron and its mother ion in their mutual Coulomb field [19]. His approach was based on the solution of the problem of Brownian motion of the electron under the influence of both its mother ion Coulomb field and the external electric field E.

The Onsager theory is based on the assumption that the distance between consecutive ionization events along the single track is much larger than the thermalization distance:

$$d_{ion} >>> d_{therm} \tag{2.3}$$

Equation 2.3 is valid for low-LET radiation. In this case, the probability of an electron escaping the Coulomb field of its parent ion, P_{esc} can be expressed as a function of the distance r, the initial separation and the orientation of the pair with respect to the external electric field, θ, by:

$$P_{esc}(r,\theta) = e^{-\frac{r_c}{r}-\beta r(1-cos\theta)} \sum_{n,m=0}^{+\infty} \frac{\beta^{m+n}(1+cos\theta)^{m+n} r^n r_c^m}{m!(m+n)!} \tag{2.4}$$

where:

$$r_c = \frac{e^2}{\epsilon K_B T} \quad and \quad \beta = \frac{eE}{2K_B T} \tag{2.5}$$

Here, r_c is the distance at which the Coulomb energy equals the thermal energy K_BT, K_B is the Boltzmann constant, T is the temperature, ϵ the liquid dielectric constant ($\epsilon = 1.94\ \epsilon_0$ for liquid isooctane at room temperature) and e is the electric charge. Mozumder [35] integrated this expression over all the initial angles θ, assuming an isotropic distribution. The free-electron yield, G_{fi}, is defined as the number of electron-ion pairs escaping IR per 100 eV of absorbed energy and represents the probability that the electrons formed by ionizing radiation have sufficient energy to escape from the electric field of the parent positive ions. It can then be expressed as:

$$G_{fi}(E,T) = N_{tot}P_{esc}(E,T) \tag{2.6}$$

where N_{tot} is the total number of electron-ion pairs initially created (those escaping initial recombination) per 100 eV absorbed energy. In Onsager's theory P_{esc} depends on the initial separation, interpreted to be the thermalization distance, which is independent of the electron's diffusion coefficient, and therefore, of the mobility. The first expansion term of the power series of the Onsager's escape probability is independent on r and, for low electric field values (0 - 2000 V/mm), varies linearly with E [78]:

$$P_{esc} = e^{-\frac{r_c}{r}}\left(1 + \frac{er_c}{2K_BT}E + ...\right) \tag{2.7}$$

According to Onsager's theory, therefore, in the low electric field region, IR and G_{fi} rise linearly with E:

$$G_{fi} \ = G^0_{fi}(1 + aE) \tag{2.8}$$

where a is a parameter that is well approximated by $1/E_0$, $E_0 = 8\pi\epsilon(k_BT)^2/e^3$ and ϵ is the medium dielectric constant. For too high E values (for values on the order of 1 MV/m), IR dependence on E becomes sub-linear, and higher-order terms must be added to equation 2.8.

The Jaffè Theory

Jaffè studied the recombination taking place in the column of ionization produced by alpha-particles. The same theory is valid for recombination taking place in the column of a proton track [21]. The Jaffè theory postulates an initial distribution of ions cylindrically symmetrical around the axis of the column and it takes into account the motion of ions under the combined effects of diffusion and electric field.

By changing the applied electric field E, the number of ions escaping IR also changes: therefore, the collected charge increases with the increase of E

([13]). A plot of chamber response (i.e. current i against the applied electric field E) is called an ionization curve and is shown in figure 2.3: it can be seen that the ionization curve in LICs never reaches saturation, contrary to ICs, because IR is strongly dependent on the applied electric field.

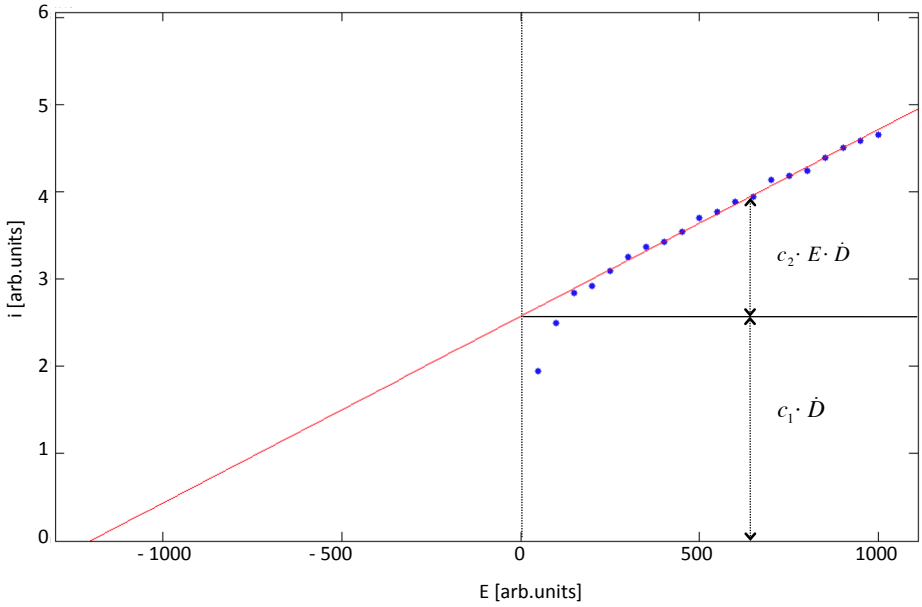

Figure 2.3: Ionization current as a function of the electric field strength (depending on equation 2.9) measured with a LIC: c_1 is the fraction of ions escaping IR due to diffusion and c_2 is the fraction of ions escaping IR due to the external electric field strength. At low E values the ionization current deviates from linearity due to GR. The red line indicates the extrapolation of the linear part of the curve down to zero gives the ratio -c_1/c_2. Adapted from [13].

In case of negligible GR, it has been shown that ionization current in a dielectric liquid increases linearly with the increasing electric field [115].

Above a certain value of the applied electric field E, the ionization curve increases linearly with the increase of E. In this region general recombination can be ignored and the ionization current i and the external electric fields strength E can be described by the linear equation:

$$i = (c_1 + c_2 E)\dot{D} \tag{2.9}$$

where c_1 and c_2 are two constants depending on the properties of the dielectric liquid, representing the probability of ion escape from IR, c_1 due to diffusion,

c_2 due to the external field strength E, and $\dot{D}$ is the dose rate. At low electric field strengths the ionization current deviates from linearity due to GR (fig. 2.3). The intercept-to-slope parameter can be obtained by extrapolation of the linear part of the ionization curve and it is given by the ratio $-c_1/c_2$. This constant $-c_1/c_2$, which represents the relative contribution from each of the two IR escape processes, is characteristic for the liquid and of the radiation quality, i.e. the LET of the radiation.

Applications of the Jaffè theory can be found in literature. Chu [109] used the Jaffè theory to calculate the ion escape probability of a LIC irradiated with gamma rays and neutrons, but observed an overestimation of the collection efficiency, that he attributed to the poor knowledge of the W/e values for isooctane. Kanai [8] exposed an IC filled with different gases to carbon and neon beams and applied on his measurements the Jaffè theory. Nevertheless, the use of the Jaffè theory for LICs exposed to densely ionizing (high-LET) radiation is still controversial and it is still considered only an approximate attempt to describe IR [77].

2.3.2 General recombination

Electron-ion pairs which survive IR thanks to diffusion and the action of the external electric field may undergo General Recombination (GR). GR was described by Greening (1964) ([31]) in case of continuous radiation and by Boag (1950) ([30]) for pulsed radiation.

2.4 Correction methods for general recombination

2.4.1 Air-filled chambers

One of the main tasks of the International Atomic Energy Agency (IAEA) is the development of Codes of Practice, or protocols, for the dosimetry of external beams used in radiotherapy. IAEA TRS-398 recommends the Two Voltage Method (2VM) for correction of GR losses [5], [10]. The collection efficiency f of the ionization chamber at the applied voltage V is defined as:

$$f = \frac{Q(V)}{Q_{sat}} \tag{2.10}$$

where the charge Q(V) measured at a given chamber potential V is always smaller than the saturation charge Q_{sat}, as some charge is lost due to recombination of positive and negative ions in the air cavity and to diffusion

of ions against the applied electric field. The 2VM assumes a linear dependence between the inverse of the collected charge and the inverse of the applied voltage V. Then, assuming that the collected charge is measured at two voltages, V_1 and V_2 and Q_1 and Q_2 are the charges measured at V_1 and V_2, respectively, then $f(V_1)$ can be written as:

$$f(V_1) = \frac{Q_1}{Q_{sat}} = \frac{Q_1/Q_2 - (V_1/V_2)^2}{1 - (V_1/V_2)^2} \tag{2.11}$$

The ratio V_1/V_2 should be equal to or larger than 3. In this formulation, any effects of space-charge screening and diffusion loss have been neglected. Moreover, when dealing with pulsed radiation, the following assumptions are made: the recombination during the radiation pulse is negligible (short pulses compared to the ion transit time), the densities of charge carriers of opposite charges are equal, and the pulse repetition frequency must be low enough that the charge generated by a radiation pulse is fully collected before the next pulse occurs.

The 2VM only takes into account GR and neglects other processes such as IR, ionic diffusion and charge multiplication. The latter can occur at high electric fields near the saturation region when some electrons gain sufficient energy to further ionize atoms in the detector volume. Zankowski and Podgorsak [7] showed that the 2VM overestimates Q_{sat}, exactly because of this effect. At the same time, when no charge multiplication takes place, IR and ionic diffusion have to be correctly taken into account, to avoid an underestimation of Q_{sat}, which could be up to 0.4%. They propose an empirical model which takes into account not only the effect of GR, but also of IR, ion diffusion and charge multiplication. The collected charge Q can then be expressed as:

$$\frac{1}{Q} = \frac{1}{Q_{SAT}} + \frac{\alpha}{V} + \frac{\beta}{V^2} \tag{2.12}$$

where Q_{SAT} is the saturation charge, α is a parameter taking into account IR and diffusion and β is related to GR. The α and β parameters can be determined by fitting the data represented in a $1/Q$ vs.$1/V^2$ plot with the equation 2.12. The total collection efficiency f_T can then be obtained as a function of the applied voltage V in the following form:

$$f_T(V) = \frac{V^2}{V^2 + \alpha V Q_{sat} + \beta Q_{sat}} \tag{2.13}$$

2.4.2 Liquid-filled chambers

For LICs the 2VM can not be used, as IR losses are much more important than in ICs. GR correction methods have been studied during the last century ([22], [23]): for example, GR losses have been determined by Johansson and Wickman [14] by direct use of the theory from Mie and Greening with the ion mobility value obtained experimentally, which implies the knowledge of mobility values and of other parameters, which are in general poorly known. Therefore, no rigorous correction method is well established for LICs.
In the last two years, the two dose rate method (2DR) [9] and the three voltage method (3VM) [12] have been proposed to perform a GR correction in low-LET beams. They will be discussed in the next two subsections.

The Two Dose Rate method (2DR)

The 2DR ([9], [100]) has a different basis depending on the radiation beam delivery: for pulsed beams, it is based on the Boag theory for f, while for continuous beams, it is based on Greening's theory. The beam signal is measured at the same time with a LIC and an IC at two different dose rates, d_1 and d_2. In the case of continuous radiation, Greening showed that for ICs the general collection efficiency is given by:

$$f_c = \frac{1}{1 + \frac{1}{6}\xi^2} \tag{2.14}$$

while for pulsed radiation, Boag showed that:

$$f_p = \frac{1}{u} ln(1 + u) \tag{2.15}$$

with

$$\xi^2 = m^2 \frac{h^4 q}{U^2}, m = \left(\frac{\alpha}{e k_1 k_2}\right)^{1/2} \tag{2.16}$$

and

$$u = \frac{\alpha/e}{k_1 + k_2} \frac{h^2}{U} \tag{2.17}$$

where h is the separation between the collecting electrodes, U is the chamber polarizing voltage, k_1 and k_2 are the mobilities of the positive and negative ions, respectively, α is the general recombination rate constant, q is the charge created per unit volume and time escaping IR and e is the electron charge. Measuring at two different dose rates with the LIC and the IC and omitting

the calculations, it has been shown by Andersson and Tölli that :

$$\xi_1^2 = \frac{\left(\frac{Q_{IC}(d_1)}{Q_{IC}(d_2)} - \frac{Q_{LIC}(d_1)}{Q_{LIC}(d_2)}\right)}{\frac{1}{6}\left(\frac{Q_{LIC}(d_1)}{Q_{LIC}(d_2)} - 1\right)} \tag{2.18}$$

for continuous radiation [100] and:

$$\frac{Q_{LIC}(d_1)}{Q_{LIC}(d_2)} = \frac{ln(1+u_1)}{ln\left(1+\frac{Q_{IC}(d_1)}{Q_{IC}(d_2)}u_1\right)} \tag{2.19}$$

for pulsed radiation [9]. In the case of pulsed radiation, f can be determined for d_1 and d_2, by solving numerically u_1, first, and afterwards u_2, by using the fact that: $u_2 = \frac{Q_0(d_1)}{Q_0(d_1)}u_1$.

The Three Voltage Method (3VM)

The 3VM [12] is an extension of the 2VM and it allows to correct for GR in both, pulsed and continuous beams. It is based on Onsager's theory for IR, which assumes that the distance between consecutive ionizations is much larger than the thermalization distance and that G_{fi} rises approximately linearly with the electric field. It consists of a system of nonlinear equations which can be solved numerically to calculate f: f can be expressed as a function of two parameters, A_c, which is dose-rate dependent, and c, which is dose-rate independent. The collection efficiency can be expressed as:

$$f_c = \left[1 + \frac{A_c(1+cV)}{V^2}\right] \tag{2.20}$$

in the case of continuous radiation, and as:

$$f_p = \frac{V}{A_p(1+cV)} log\left(\frac{V + A_p(1+cV)}{V}\right) \tag{2.21}$$

in the case of pulsed radiation, with

$$A_c = \frac{\alpha N_{ion}^0 h^4}{6k_1k_2} \tag{2.22}$$

and

$$A_p = \frac{\alpha r_0 h^2}{e(k_1+k_2)} \tag{2.23}$$

where N_{ion}^0 and r_0 are the number of ionized pairs per unit volume and unit

time (those that escape from initial recombination) for continuous and pulsed beams, respectively.

The 3VM, being developed on the basis of the Onsager theory, can not be applied to high-LET radiation, due to the small distance between ionized pairs. However, the authors claim that, when the collected charge shows a linear dependence on the electric field [8], this method might be of utility.

2.5 The 2D-array Liquid Ionization Chamber (LIC)

The high sensitivity of LICs has already been employed in different applications. Two-dimensional (2D) matrices of LICs have been developed for dynamic multileaf collimator (MLC) verification [102], [103] [1]. In the course of our collaboration with Universidade de Santiago de Compostela (USC) we developed the idea to use LICs for LET measurements. In particular, the dependence of the IR process on LET could be exploited to study LET distributions in one plane along the depth dose curve of hadron beams. However, translating this world to high LET presents the challenge of increased IR.

A two-dimensional liquid-filled ionization chamber (2D-array) was developed at USC for the verification of IMRT profiles [1]: during IMRT dose delivery needs to be monitored with detectors with high spatial resolution and fast response and, therefore, LICs are perfect candidates for such applications.

The 2D-array consists of a matrix of 16 $\times$ 8 channels filled with liquid isooctane (2,2,4-Trimethylpentane, C_8H_{18}), a stable dielectric liquid, with structure and stoichiometric form illustrated in figure 2.4(a) and 2.4(b).

The ideal liquid should be a good insulator, to help in keeping the leakage current low; it should have a high ion yield (i.e., a low ionization potential), to have a sufficient signal when irradiated; its density and atomic number should be close to the ones of water; the stopping power ratio to water should have no energy dependence; the mobility of ions created by irradiation should be as high as possible, to minimize recombination. Liquid isooctane is an insulating non-polar liquid, composed by low atomic number elements. It has a density of 0.69 g/cm^3 and an effective atomic number of 5.4, which is quite similar to the one of water (7.4). It is expected, therefore, to present only a low perturbation of the radiation field for water or water-like material measurements. Some of the physical and chemical properties of liquid isooctane

[1] MLCs are used in intensity modulated radiation therapy (IMRT) to provide conformal shaping of the beams through the independent movements of individual "leaves"

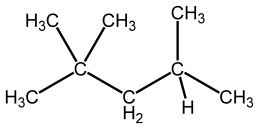

(a)

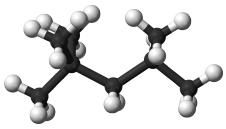

(b)

(c)

Chemical form	C_8H_{18}
Molar mass	114 g/mol
Density	0.69 g/cm^3
Melting point	-107 °C
Boiling point	99 °C
Rel. Dielectric constant	1.94
Ion mobility (both)	3.5 10^{-8} m^2/s V
Recombination constant	5.9 10^{-16} m^3/s
G_{fi}^0 1/β	0.32 pairs/100 eV 1.74 10^6 V/m
Thermalization distance (Co)	163 Å

Figure 2.4: The isooctane molecule (2,2,4-Trimethylpentane: C_8H_{18}): chemical composition (a); 3D-structure (b); physical and chemical properties (c).

are reported in the table in figure 2.4(c). The stopping-power ratio water-to-liquid is quite constant for isooctane compared to air over the range of clinically relevant electron energies (with a variation of 5% compared to the 20% of air over the same energy range of 1-20 MeV), which makes the conversion of ionization response to absorbed dose to water almost independent on the energy [37]. The ratio of the collision stopping-power for air-water and for isooctane-water is shown in figure 2.5 (defined as the rate of energy loss resulting from the sum of the soft and hard collisions, usually referred to as "collision interactions"). A liquid detector filled with isooctane is expected to be, therefore, very little energy dependent [6].

A schematization of the 2D-array layout is illustrated in figure 2.6. The matrix is composed by 128 pixels, arranged in a 16 × 8 grid: each of them has a dimension of 1.8 × 1.8 mm and a pitch of 2 mm, for a total active area of 3.2 × 1.6 cm^2. The detector is composed by two printed circuit boards (PCBs) [1], which are made from FR4 fiber glass epoxy. The upstream PCB is 0.15 mm thick and contains the high-voltage plane, provided by a Cu+Ni+Cu metallization (drift plane). The downstream wall is composed by a multilayer PCB with a 0.47 mm thickness and contains the 128 electrodes segmented anode. The 0.5 mm thick isooctane layer is given by a G10 spacer and it is located between the drift plane and the segmented anode. A guard electrode ensures that the electric field near the edge of the collecting electrode remains straight and minimizes the leakage from the volume outside of the collecting volume. The PCB inner layers contain metallic strips that carry out the ionized charges to the read-out electronics, which is attached to the edge of

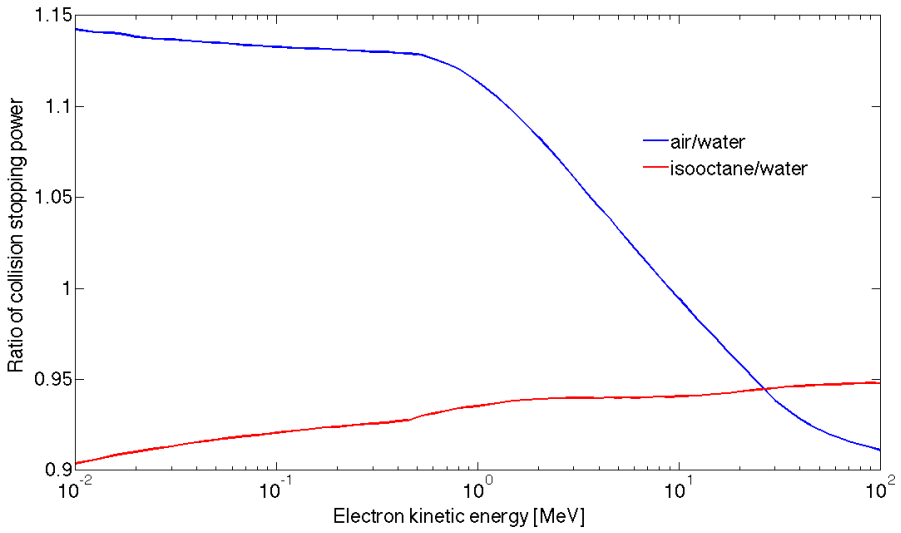

Figure 2.5: Collision stopping-power ratios as function of electron kinetic energies for air-water (blue line) and isooctane-water (red line) [101].

the detector and contained in the metallic box visible in figure 2.7. A voltage of +5V and +12V is required to feed the electronics and it is provided by an external source. The total dimensions of the assembled device are 350 mm $\times$ 70 mm $\times$ 45 mm.

The detector is located in between two PMMA (Poly-methyl-methacrylate) 5 mm thick slabs, which provide mechanical rigidity. The read-out is performed with one X-ray Data Acquisition System (XDAS) board (Sens-Tech Ltd, UK), which integrates 128 read-out channels. The XDAS is controlled and read-out through an ethernet interface using raw-packet communication. The integration time can be varied from 10 μs up to 0.5 s, and the number of subsamples from 1 to 128 as powers of 2 (The number of subsamples is the number of measurements that the XDAS will acquire and average before sending an output to the acquisition computer.)

Data acquisition and detector control is carried out with a software based on LabView (National Instruments, USA), developed by the manufacturers in USC. The XDAS operation parameters are set at the beginning of the acquisition. Basic commands allowing background subtraction, sequence of acquisitions, mean value and sum saving, together with some more complex routines as e.g. saving a sequence of segments specifically oriented to IMRT verification, are implemented in this software to facilitate the different tasks performed in dosimetry. A view of the data acquisition software GUI is shown in figure 2.8.

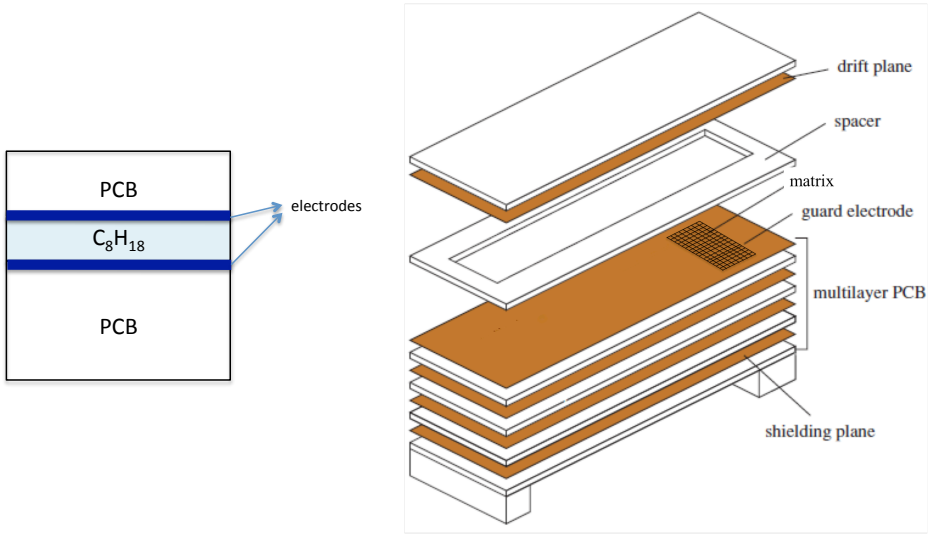

Figure 2.6: The 2D-array: cross section of the detector (left) and schematic layout of the detector [11] (right).

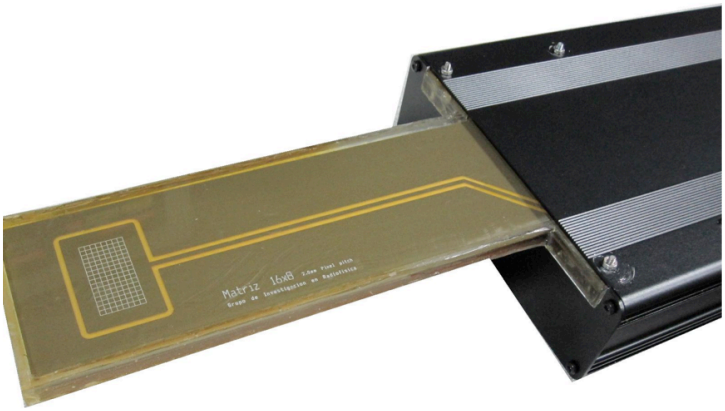

Figure 2.7: Picture of the 2D-array: on the left, the matrix sandwiched between the two PMMA slabs can be seen. They are attached to the black box, visible on the right, containing the electronics.

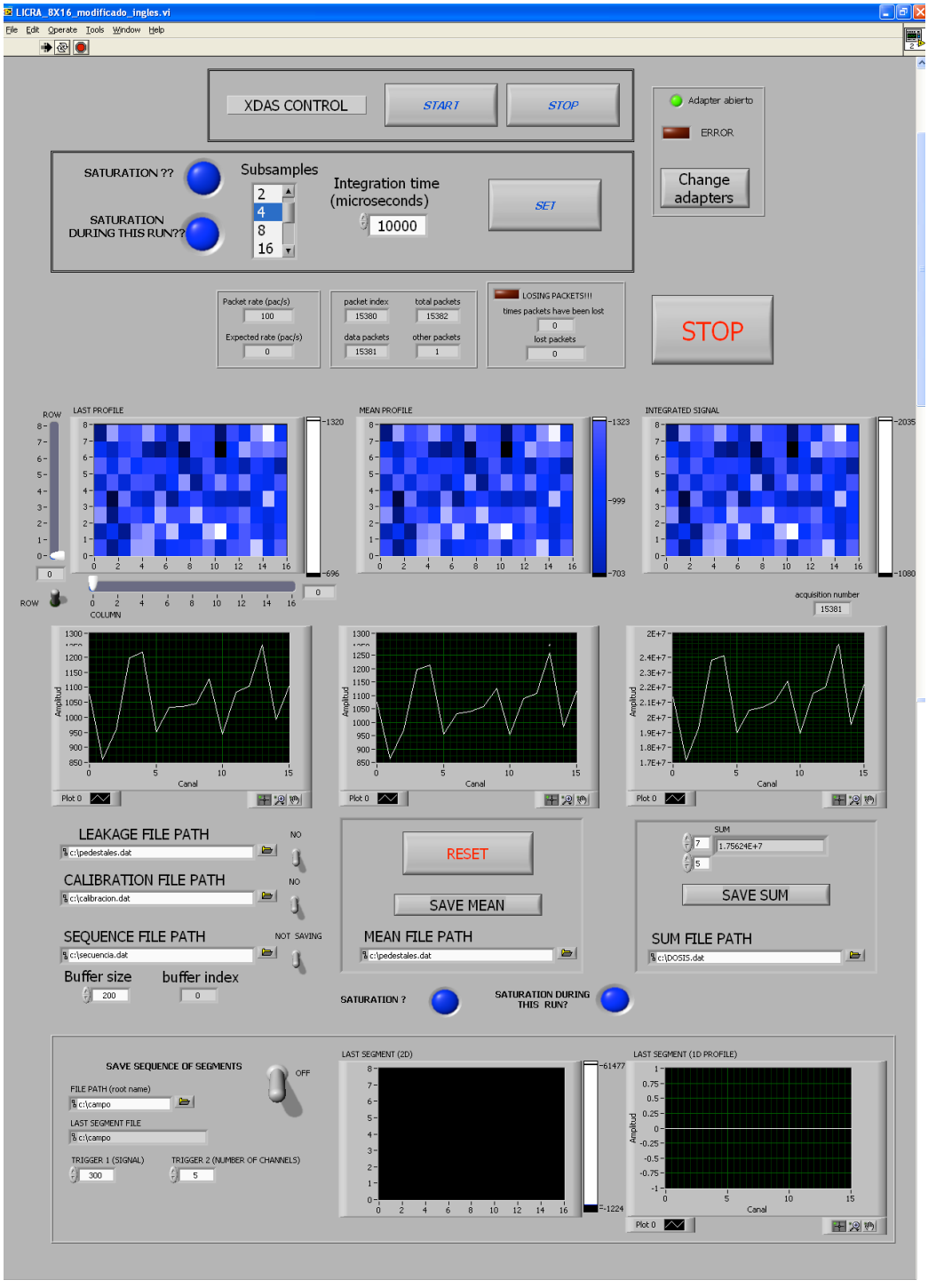

Figure 2.8: General view of the 2D-array data acquisition software GUI.

2.6 Other LIC arrays

Recently, a lot of interest arose on the LICs technology. Matrices of LICs can be employed as quality assurance (QA) devices to monitor the beam before and during the treatment. With their high sensitivity, they are able to provide planar dose information, which cannot be done using single LICs, because their volume is too small to verify that the treatment is correctly delivered. Recently, a commercial device has been developed by PTW for beam verification and QA: it is a 2D matrix called Octavius 1000 SRS (figure 2.9, right) and it is able to provide high-resolution dose measurements of radiation fields smaller than 1 cm $\times$ 1 cm and of regions with steep dose gradients.

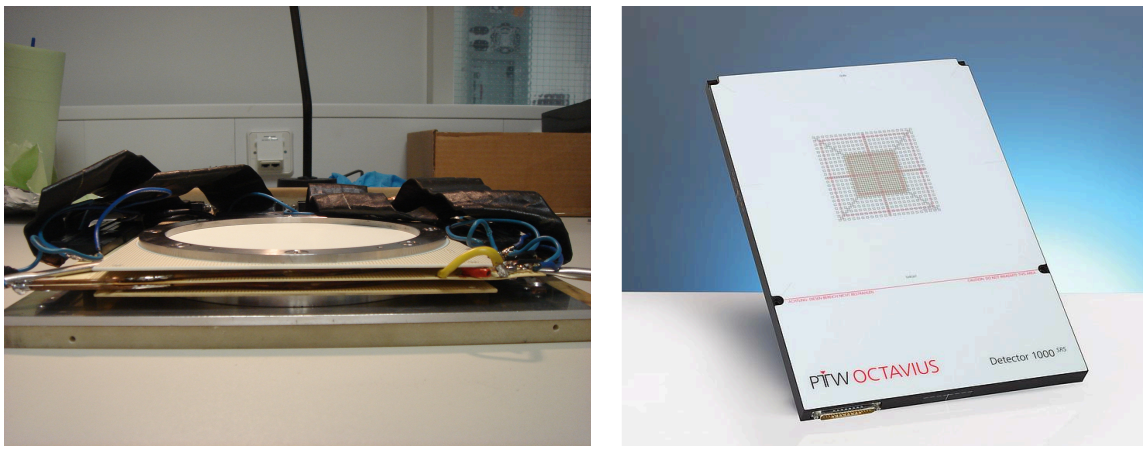

Figure 2.9: Photograph of a prototype of a LIC array, developed in Karlsruhe, for dynamic MLC verification [102] (left). The 2D array of LICs Octavius 1000 SRS, a commercial product from PTW (right).

Chapter 3

Experimental Results

To study the response of the LIC to different kind of radiations, we performed measurements with low-LET beams - at the Deutsches Krebsforschungszentrum (DKFZ) in Heidelberg - and with high-LET beams - at the Heidelberg Ion-Beam Therapy Center (HIT) and at the antiproton Decelerator (AD) at CERN, Switzerland. An overview over the various irradiation systems will be given in the next sections.

3.1 Low-LET irradiation systems

The 2D-array was irradiated with two kinds of low-LET sources: a ^{60}Co source and a linear accelerator (LINAC). In both cases, the detector is sandwiched between 2.5 cm of PMMA on the top and 5 cm on the bottom, to guarantee that the LIC is beyond the maximum of the build-up region along the depth dose curve (see fig. 1.13), which assures charged-particle equilibrium.

Figure 3.1 represents a schematic cross-sectional view of a beam of a given energy and field size incident normally on a tissue-equivalent water phantom. Dose at a certain point is given as a function of the depth in the phantom (d), the field size measured at phantom surface (s), the lateral distance from the central axis (r), and the radiation source to phantom surface distance (SSD).

The dose rate can be varied by varying the distance from the source.

The beam provided by the Siemens Artiste LINAC of DKFZ is a pulsed electron beam. The so-called monitor unit (MU) is used to measure the LINAC output (i.e., current). The LINAC is calibrated such that 100 MU gives an absorbed dose of 1 Gray for a 10×10 cm^2 field at 95 cm SSD.

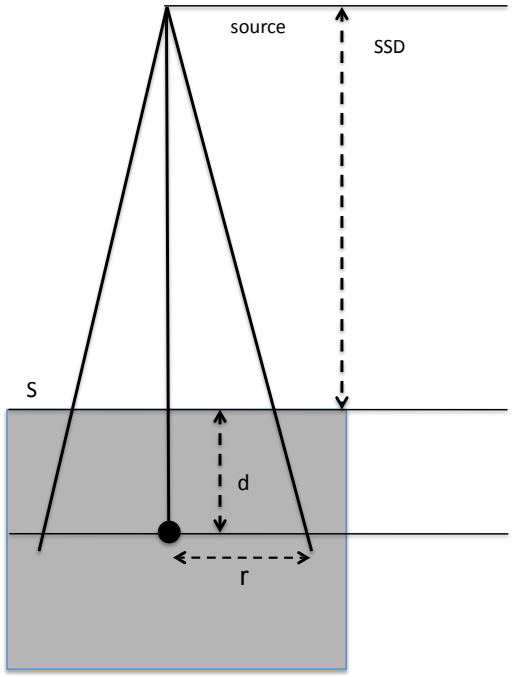

Figure 3.1: Schematic cross-sectional view of the LINAC irradiation geometry. The beam impinges normally on a tissue-equivalent water phantom. Dose at a given point is given as a function of the depth in the phantom (d), the field size measured at phantom surface (s) and the radiation source to phantom surface distance (SSD). [105].

3.2 The HIT facility in Heidelberg

The Heidelberg Ion-Beam Therapy Center (HIT) was the first clinical-based ion therapy facility in Europe, located at the Radiological University Hospital in Heidelberg (Radiologische Universitätsklinik Heidelberg, Germany). It started its operation in November 2009 and in the first two years more than 600 patients have been treated. It is a unique radiotherapy center, as it offers proton and heavy-ion beams not only for treating patients and for clinical studies, but also for physical research. HIT started as part of the University Hospital of Heidelberg, from the collaboration with the German Cancer Research Center (DKFZ) and the Gesellschaft für Schwerionenforschung (GSI), where the pilot project on Heavy-Ion Cancer Therapy was developed. Siemens Healthcare provided the treatment planning system, the patient positioning and verification system, the beam application including scanning and control system. The Raster Scan Method, an active beam delivery system that allows to cover the whole tumor volume, is integrated into the HIT gantry, the only rotatable heavy-ion gantry worldwide.

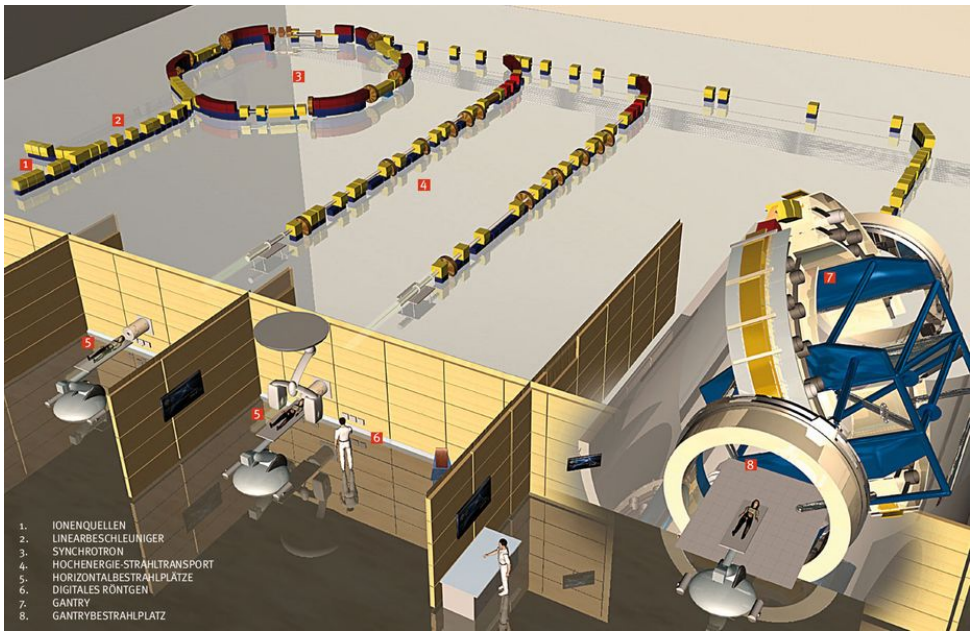

Figure 3.2: The Heidelberg Ion-Beam Therapy Center (HIT) Facility ([50]).

In figure 3.2 a schematic layout of the facility is depicted. In (1) two 14.5 GHz permanent magnetic electron cyclotron resonance (ECR) ion sources from PANTECHNIK, running 330 days per year, are used to produce proton, carbon and oxygen beams from collisions between carbon dioxide gas

and electrons accelerated by magnetic fields and microwaves [104]. In (2) a LINAC collimates and accelerates particles from 8 keV/u to 7 MeV/u. It consists of the low-energy beam transport line (LEBT), a 400 keV/u radio-frequency quadrupole accelerator (RFQ) and a 7 MeV/u IH-type drift tube linac (IH-DTL). The LINAC injects the particles in a compact synchrotron with a circumference of about 65 m. The synchrotron provides a variety of beam parameters: for both protons and carbon, the range of extraction energies covers penetration depths in water from 20 mm to 300 mm, ranging between 90 and 430 MeV/u, for carbon, and between 40 and 220 MeV, for protons. After the extraction, the beam is distributed by the high-energy beam transport line (HEBT), composed by vacuum tubes and magnets, to one of the three treatment rooms (4). Two of them are fixed horizontal rooms. Here, the patient is positioned on a robotically positioned treatment couch and immobilized with the help of masks (5). Before irradiation starts, the correct position is checked with a computer tomography (CT) digital X-ray scanner (6). In the third room, the beam is guided along an isocentric gantry (7), which allows irradiation at different angles. A fourth fixed beam station, the quality assurance (QA) room, is used for QA, development and research activities. All places are equipped for a 3D raster scan volume conformal irradiation: the beam passes trough two scanners, which scan the beam horizontally and vertically.

The maximum available beam intensity at the patient treatment place are 8×10^7 particle/s (for carbon) and 3.2×10^9 particle/s (for protons).

Beam Characteristics at HIT

Due to the beam extraction procedure of the synchrotron, particles are delivered not continuously, but in spills. The extraction time of the synchrotron is fixed to 5 s, thus providing spills which are five seconds long and separated from one another by a temporal interval of five seconds. Extraction may be aborted earlier by the treatment system. The spill may be interrupted asynchronously up to five times, enabling the irradiation of disjoint tumor slices in a single acceleration cycle. A temporal sequence of a proton beam measured with the LIC is depicted in figure 3.3.

As can be seen, the intensity (dose rate) during one spill is not stable, but it can vary up to 20 %. The total number of particles delivered is equal to the one prescribed by the plan and read by the operation system, as, for therapeutical purposes, the total dose (i.e., total number of particles) must be accurately monitored. Hence, as soon as the total dose is delivered, the spill is aborted. While dose-rate variations have no relevance for therapy, they do have in the LIC response. All the main measurements that will be

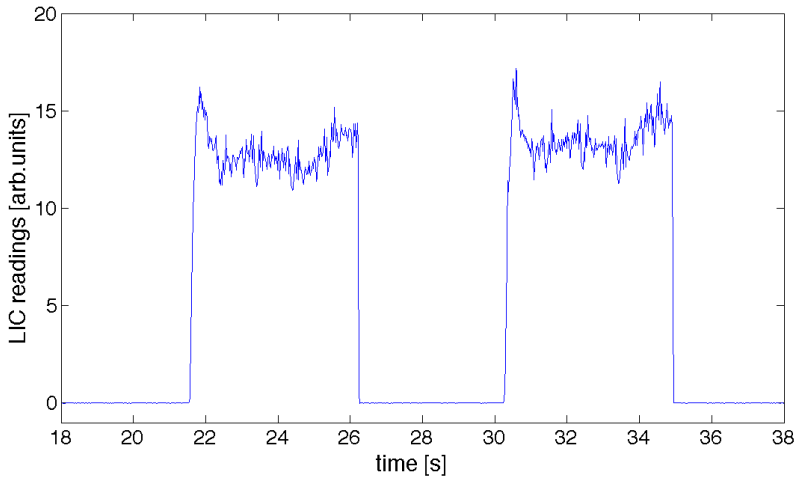

Figure 3.3: The typical spill structure of a proton beam (energy 128.11 MeV) at HIT is five seconds beam on and five seconds beam off. The temporal sequence is measured with the whole LIC matrix.

discussed in chapter 4 have been done at the lowest dose rate, to minimize the effect of GR.

The beam experimental settings provided by the accelerator operation system which can be chosen by the experimenter are: the ion species, the energy, the dose (total number of particles), the dose rate (particle/s), the focus (Full Width Half Maximum, FWHM, measured in the nozzle). Specifications of the parameters used in the experiments are summarized in table 3.1.

From now on the beam will be defined in terms of energy and intensity levels and focus number (i.e., the FWHM measured at the nozzle).

3.3 The ACE Experiment at CERN

The antiproton Cell Experiment (ACE) started in 2003 at CERN to study the potential of using antiprotons as an alternative to protons and carbon ions in hadrontherapy ([51]).
The rationale of studying the biological effectiveness of antiprotons is due to the behavior of these particles when they pass through tissue: fast antiprotons penetrating matter have the same stopping power as protons, hence, in the plateau they behave like protons, releasing a small amount of energy (dose) on their way to the tumor. When they slow down to eV energies, they are captured by high-Z nuclei of the target material, they deexcite and

Particle type	Energy (MeV/u)	E level (#)	Focus (mm)	Dose rate (part/s)	Dose rate level (intensity)
p	128.11	100	12.8	1.2e8	i2
				2e8	i3
				3.2e8	i4
p	150.95	140	12.4	1.2e8	i2
c	241.84	100	10.2	5e6	i3
				8e6	i4
				10e6	i5
c	283.76	140	10	5e6	i3
c	329.44	180	9.9	5e6	i3
ox	286.05	100	10.2	4.5e6	i4
ox	340.52	140	10	4.5e6	i4

Table 3.1: Beam parameter used during the experiments performed with the LIC.

finally they annihilate with a nucleon. This annihilation process releases 1.88 GeV [52] (twice the rest mass of the proton) and the energy released is converted on average in 4 or 5 pions (π^-,π^+ or π^0). The π^0 is unstable and instantaneously decays into high-energy gamma rays (70-300 MeV). If one of the charged pions escape the nucleus, it recoils with the Fermi momentum of the lost nucleon (i.e. 0.1–5 MeV). If, instead, one of them penetrates the nucleus, there will be an intranuclear cascade that will cause the nucleus to break into fragments (mainly, neutrons, protons and heavy nuclei). As charged fragments have a very short range (smaller than 10 μm), they will release their kinetic energy in the vicinity of the annihilation vertex. The total energy deposited locally by these fragments has been estimated 30 MeV per antiproton [112], which has been confirmed experimentally by Sullivan [52]. Some of these fragments have a high-LET and an increased biological effectiveness compared to protons. When antiprotons come to rest at the end of their range, therefore, they can in principle create DNA damage like carbon ions do [110].

To investigate the biological effects of antiprotons and the potential benefits of using them as alternative to protons or heavier particles, V79 Chinese hamster cells are exposed to antiproton irradiation using the antiproton decelerator (AD) at CERN [53], [110]. The first results coming from the 2011 and 2012 runs showed a steep increase of RBE for antiprotons at the proximal edge of a SOBP, in contrast to carbon ions, where RBE is increasing more gradually along the beam path.
To interpret the results correctly, it is of crucial importance to know and

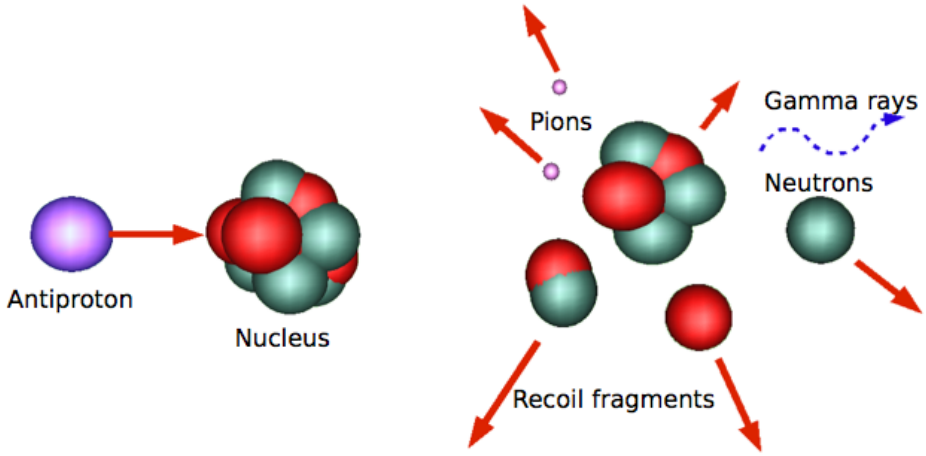

Figure 3.4: Antiproton annihilation creates gamma rays, pions, nutrons and recoil fragments [118].

carefully monitor the physical beam parameters. Therefore, in parallel to the biological experiments, other kinds of dosimetry studies using different detectors are performed. These studies aim to answer the question related to the feasibility of standard dosimetry when the reference conditions are not met and identify the possibility of measuring the beam quality, in particular, LET.

3.4 The 2D-array

This section is divided in two main parts: the first one is about the preliminary characterization of the 2D-array, needed to understand how the LIC responds to irradiation. The second one is about the study of LICs' recombination processes, in particular initial recombination and its dependence on LET, with the purpose of overcoming the disadvantage of recombination and turning it into a key to determine LET.

The original idea of relating IR to an LET measurement has been approached from two sides:

- the intercept-to-slope parameter of the linear part of the so-called voltage curve (or ionization curve), as reported in literature, should be LET dependent. This dependence has been analyzed for different particle beams, but it was suffering from unaccuracies, which gave rise to big error bars, and it only provided relative LET values.

- the idea of coupling the reading of two detectors, a LIC and an air-filled chamber, and hence to quantify, at each depth, their different response to irradiation through a ratio, which is LET dependent.

3.5 Characterization of the 2D-array

A physical characterization of the device is presented, along with a theoretical study on charge-carrier mobilities performed with the 2D-array. This demonstrates that LICs are versatile instruments, which can be used not only as dosimeters, but also to perform other fundamental studies, for example, on the properties of the liquid used as a sensitive medium.

3.5.1 Measurement of the real 2D-array gap

The value of the isooctane gap of the 2D-array given by the manifacturer is 0.5 mm. This number refers to the whole nominal layer thickness and it does not take into account the thin epoxy layer, necessary to glue the PCBs together, and hence a value of 0.6 mm would be more realistic.

To determine the real gap for each pixel, one can assume that the 2D-array is a parallel plate capacitor. In this case, the capacitance, C, is related to the surface of the two plates, S, and the distance between them, d, as:

$$C = \epsilon \frac{S}{d} = \epsilon_r \epsilon_0 \frac{S}{d} \tag{3.1}$$

where ϵ is the total dielectric permittivity, ϵ_r the relative permittivity of the dielectric material between the plates and ϵ_0 the permittivity in vacuum. In a capacitor, a voltage increase ΔV generates a charge ΔQ depending on the linear relation:

$$\Delta Q = a + C\Delta V \tag{3.2}$$

where the capacitance C is the coefficient of the linear slope and a a parameter of the fit to account for a potential offset in the experiments.

To evaluate C, hence, the charge ΔQ_i induced by different polarization voltage steps, ΔV_i has been measured and C has been determined from the slope of the linear fit to the data.

The voltage was increased by fast random steps between 0 and 1300 V. When a voltage step occurs, the LIC responds with a spike after which the LIC reading returns to a constant value. This behavior is represented in figure 3.5, where a zoom on a single voltage step is shown.

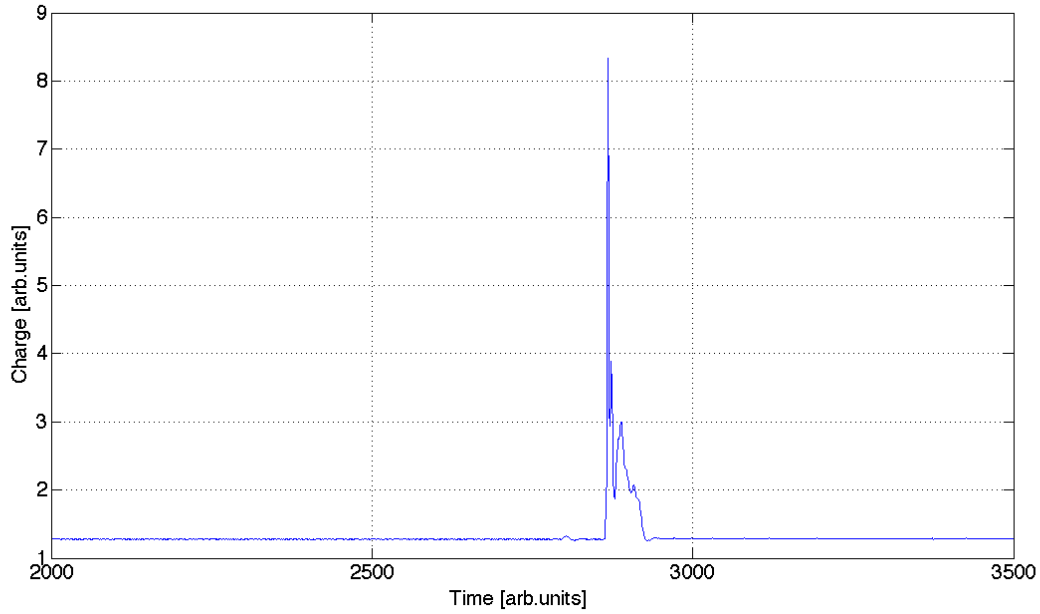

Figure 3.5: LIC reading as a function of time, for one single voltage step: the voltage is increased from V=632 to V=745.

After the spike, the signal comes back to approximately the same value as before, meaning the there is no significant leakage current caused by the change of the voltage. If the leakage would be exactly zero, after the voltage spike the signal would go back to its original value before the V change. In figure 3.6, a zoom on the y-axis for different ΔV is shown: the slight signal increase after each voltage spike indicates that the LIC does not behave exactly like an ideal detector, but that a small leakage is associated to the voltage change.

The induced charge ΔQ as a function of the voltage steps ΔV is depicted in figure 3.7 for a single channel of the matrix.

The data are fitted with $\Delta Q = a + C\Delta V$ (blue line) and with $\Delta Q = C\Delta V$ (red line). The agreement between the fits is a sign that the parameter a is, as expected, very low, which means that no charge is collected at zero voltage.

The same fit can be done for all the 128 channels and from it C can be calculated for each of them. By using equation 3.1, the numerical value of d can be adapted to adjust the fit as best as possible to the experimental data. The results are depicted in figure 3.8.

The pixels on the edges of the matrix do not behave exactly like parallel-

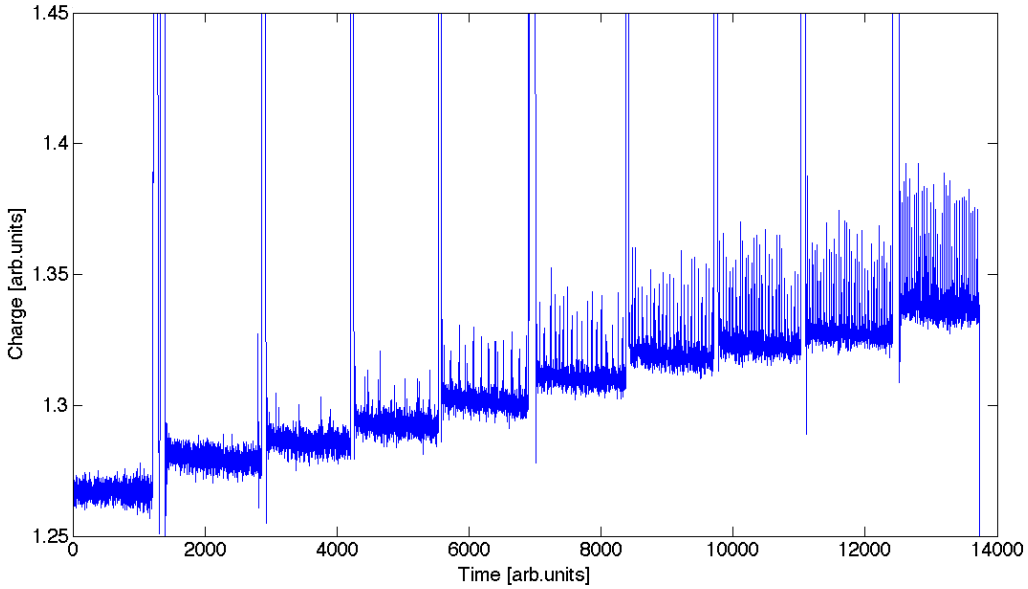

Figure 3.6: LIC reading as a function of time, for 9 random voltage steps, ranging from V=0 to V=1300.

plate capacitors; therefore they are outside of the general trend.

The electrical capacitance is slightly lower than the theoretical one, which indicates that the real dimension of the gap is bigger than the nominal one. The value resulting from such measurements is between 0.6 mm and 0.65 mm.

3.5.2 Response uniformity and leakage control

Due to the specific process how the pixels are produced, each pixel of the 2D-array exhibits differences from the others in the gain of the electronic read-out channel (up to around 0.6%), in the pixel gap and also in relation to some area inhomogeneities. We studied, therefore, the response of the LIC matrix to a uniform radiation field, using a flat field of 30×30 cm^2 generated with the ^{60}Co unit of DKFZ. The 2D-array was positioned in the isocenter sandwiched between two sets of PMMA slabs (as described in par. 3.1) and the dose rate was 0.14 Gy/min. The LIC response under such a flat field is represented in figure 3.9.

The reading at the four edges are higher than in the rest of the matrix. This effect is due to a small space of 0.4 mm existing between the guard electrode and the pixels at the borders, which is responsible for the small

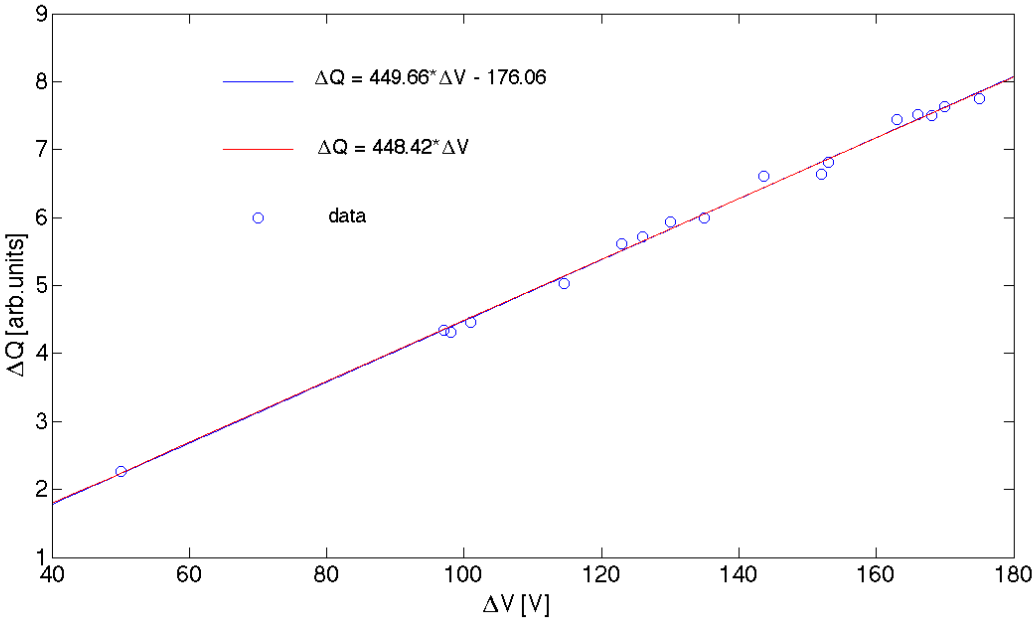

Figure 3.7: ΔQ induced from random ΔV steps for one single channel of the LIC and linear fit with ΔQ=a+CΔV (blue line) and with ΔQ=CΔV (red line). The two fits overlap very closely due to the small a value.

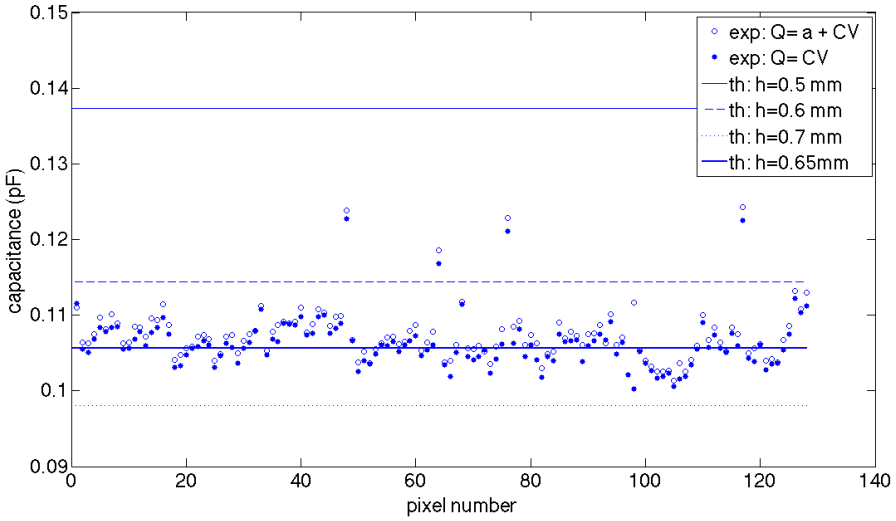

Figure 3.8: Capacitance values for all the 128 channels as calculated from $\Delta Q = a + C\Delta V$. The fits indicate a gap value between 0.6 mm and 0.65 mm. The four points off the trend are located at the corners, where a parallel-plate capacitor behavior is not expected.

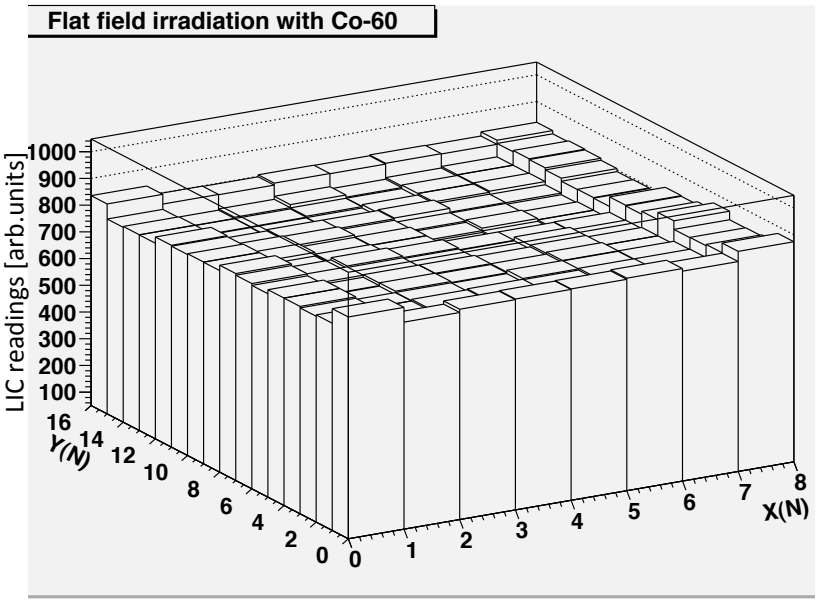

Figure 3.9: Irradiation of the 2D-array with a flat field from a ^{60}Co source: the edge effects are clearly visible for the pixels at the boundaries of the array.

amount of additional charge collected by the border pixels.

The guard electrode ensures that the electric field near the edge of the collecting electrode remains straight and minimizes the extent of charge leakage from the volume outside of the collecting volume because there is no significant driving potential to promote this additional charge collection by the collecting electrode in preference to collection by the guard electrode.

To quantify the variation of the leakage current with time, the 2D-array collected data without being irradiated during a whole night.

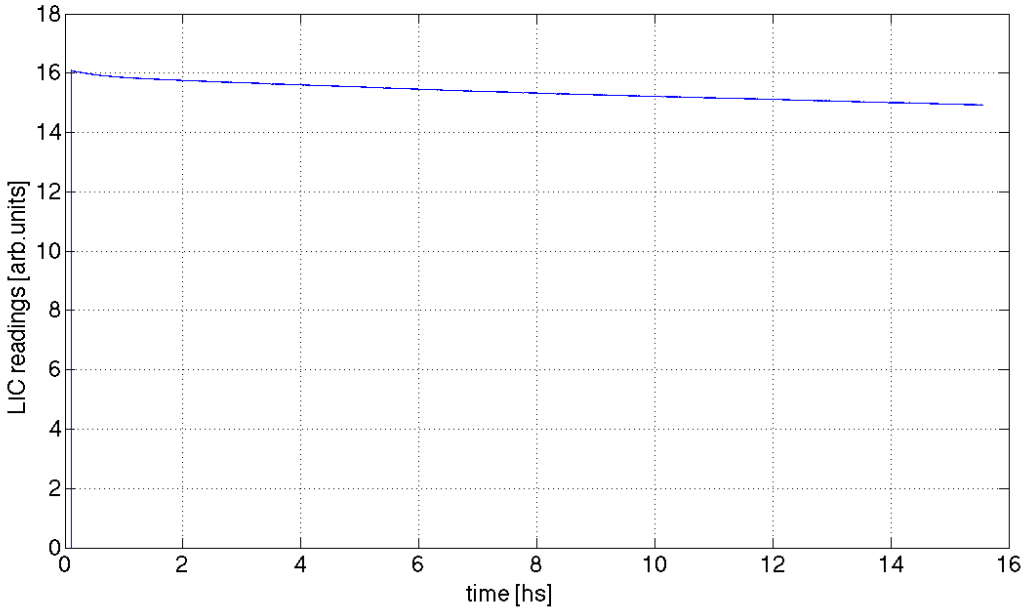

Figure 3.10: Measure of the leakage current during night: with the decrease of the room temperature, the leakage current decreases as well during night.

As can be seen in figure 3.10, the signal - and therefore the leakage current - is higher in the first hours and then it decreases slowly during night. This trend might be explained with a slight change in the temperature, which decreased by $\sim$2°C during night. The leakage current does not only change with time, but also with the voltage applied between the electrodes. Luckily, it can be recorded and subtracted, therefore, before each measurement, the contribution of the leakage to the measured values was always accounted for.

3.5.3 Dose rate dependence

An ideal detector in dosimetry should be energy and dose-rate independent: both these requirements have been studied for the 2D-array.

The dose-rate dependence has been studied by irradiating the 2D-array with the LINAC of DKFZ. The distance between the 2D-array and the LINAC was set to 100 cm, 30 cm and 150 cm from the source, to obtain a different dose per pulse. The 2D-array was irradiated with a flat field of 10×10 cm^2, the electron energy was 6 MV, the dose rate was 50 monitor units per minute (MU/min) and the total dose was 50 MU (at the isocenter). The dose rate has been determined with a Farmer Ionization Chamber (FC Type 30010, PTW) irradiated under the same conditions used for the 2D-array. The signal recorded with the LIC is depicted in figure 3.11.

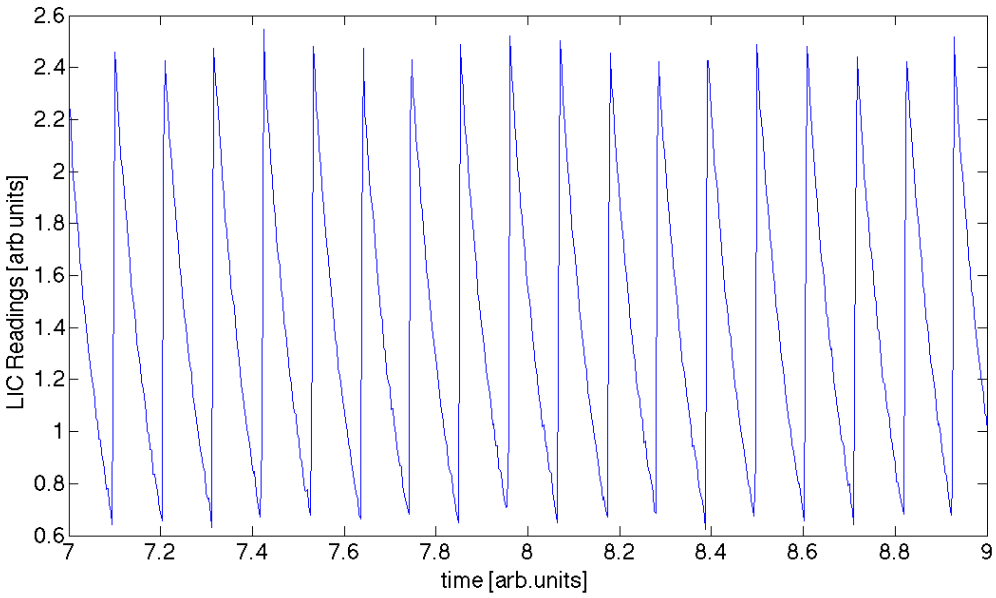

Figure 3.11: The LIC signal does not go to zero after one spill, because the charge is not completely collected before the arrival of the next spill.

The LIC signal does not go to zero after one spill, because the charge is not completely collected before the arrival of the next spill. Unfortunately, this effect could not be avoided, because it was not possible to further reduce the pulse repetition frequency.

To verify the dose-rate dependence, data were fit to the Fowler-Attix relationship [106]:

$$S = k\dot{D}^{\Delta} \tag{3.3}$$

where S is the 2D-array reading, $\dot{D}$ is the dose rate (in mGy/min), k a proportionality factor and Δ is related to the dose-rate dependence. The data measured at different dose rates and for different voltages are fitted with equation 3.3 and are depicted in figure 3.12.

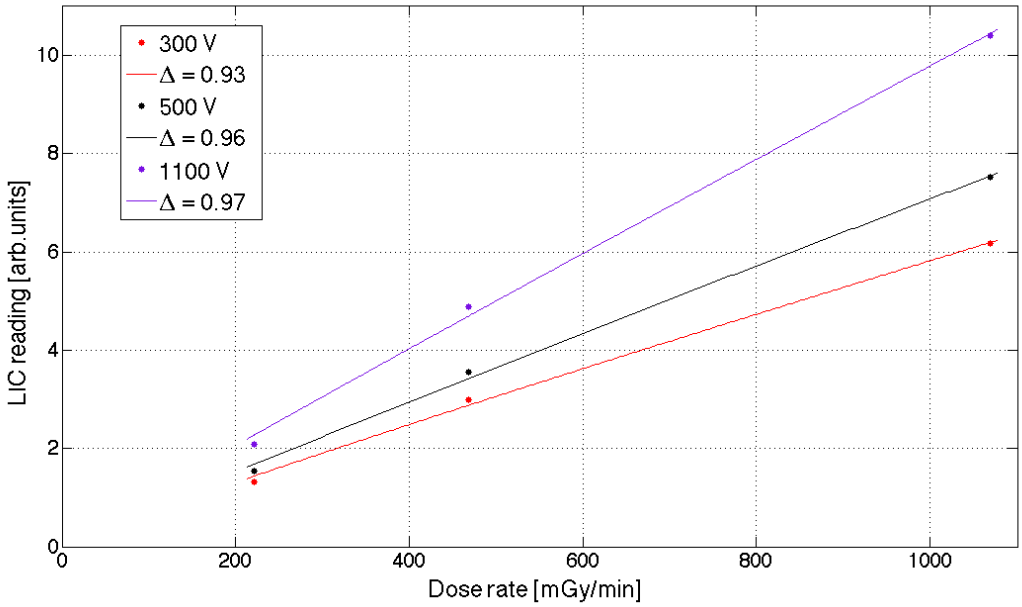

Figure 3.12: 2D-array read-out signal versus dose rate: the data have been fitted with the Fowler-Attix relationship (solid lines, eq. 3.3) for three different applied voltages. The dose rate was varied by changing the source-to-detector distance, while keeping constant the monitor units (50 MU/min).

For a linear dose-rate response, Δ is expected to equal 1. In figure 3.12 Δ=0.97 at 1000V, which points to a moderate dependence of the LIC on the dose rate. At lower voltages, the trend departs more from linearity, due to the enhanced effect of general recombination at lower voltages.

3.6 Impurities in dielectric liquids

Liquids with a low dielectric constant are characterized by a conductance which is related to groups of few ions (clusters) moving under the influence

of an external electric field, more than to movements of single ions, which are quite difficult to distinguish.

An important property of liquids is the mobility μ, which is related to the drift velocity ν_D and the electric field E trough [38]:

$$\nu_D = \mu E \tag{3.4}$$

If electronegative impurities are present in the liquid, they have the tendency to capture free electrons available in it. When one electron is captured by an impurity, they form negative ions with lower mobility. The rate at which the electron is trapped is given by:

$$\frac{d[e^-]}{dt} = k[e^-][Y] \tag{3.5}$$

where $[e^-]$ and $[Y]$ are the concentrations of the electrons and of the impurities in the medium, respectively, k is the reaction rate constant, given in $[M^{-1}]$ (moles) $[s^{-1}]$, quantifying the speed of the reaction and Y is the impurity involved in the process. When one electron reacts with oxygen, which is the most common impurity:

$$e^- + O_2 \longrightarrow O_2^- \tag{3.6}$$

with k=6×10^{11} M^{-1} s^{-1}. Another common impurity is carbon dioxide, CO_2, for which electron capture is reversible:

$$e^- + CO_2 \longleftrightarrow CO_2^- \tag{3.7}$$

In (3.7) the CO_2 molecule traps one electron, but the resulting anion is unstable and releases the electron back into the solvent. As a result of this process, the drift time increases, which means that the mobility decreases. For CO_2, k=4.2×10^{11} M^{-1} s^{-1}.

Commercial non-polar liquids used in LICs, like isooctane, are used in non-ultrapure regimes [39] (99.5% purity), resulting in ionized electrons being instantly attached to electronegative impurities, and thus, charge carriers are positive and negative ions. The knowledge of the mobility values and of the kind of charge carriers is a critical point in the modeling of the ionization process and charge collection in non-polar liquids. The mobilities of positive and negative charge carriers affect also the recombination rate in LICs, and therefore, their determination is important for quantifying such effects.

3.6.1 Mobility study

The LIC can be used to study the mobility of the charge carriers produced in liquid isooctane by looking at the temporal development of the LIC signal irradiated with a low dose-rate source, which guarantees low recombination losses. This has been done with the 2D-array, which was irradiated with a 6 MV Siemens Mevatron LINAC. The pulsed photon beam generated by this LINAC has a frequency that depends on the monitor unit rate, while the pulse length is a few microseconds, which is negligible in comparison with the charge depletion time that amounts to a few milliseconds. The monitor unit rate was set to 50 MU min^{-1} - its minimum value - which corresponds to a pulse repetition frequency of 64 Hz. The distance from the source to the LIC was 150 cm in order to have a low dose per pulse, around 0.06 mGy $pulse^{-1}$, and negligible general recombination effects. The polarization voltage was 1500 V, which was set in order to achieve total charge depletion before the arrival of the successive pulse, thus avoiding pulse overlapping. The integration time was set to 0.8 ms, which is large enough to have a significant signal and low enough to avoid signal shape distortions due to the integration time. Several thousand pulses have been fitted with three different models:

- 2CC: two charge carrier species, one positive, represented by ionized isooctane molecules and one negative, represented by one type of impurity;
- 3CC: three charge carrier species, one positive, represented by ionized isooctane molecules and two different kind of negative impurities;
- GCC: positive and negative charge carriers distributed according to a Gaussian distribution.

A typical pulse is depicted in figure 3.13.

The pulse shape is best described by the 3CC model, indicating that the model with three different mobilities is the one that describes the experimental data best. Adding a fourth mobility does not improve the quality of the fit. Of course, this study is related to the isooctane quality used, because the level of impurities is dependent on that, but it pointed out that the recombination may not be described with only two kind of charge carriers.

3.7 LET determination: a first attempt

The dependence of Initial Recombination (IR) on LET offers the possibility to characterize the beam quality in terms of LET. As shown in previous

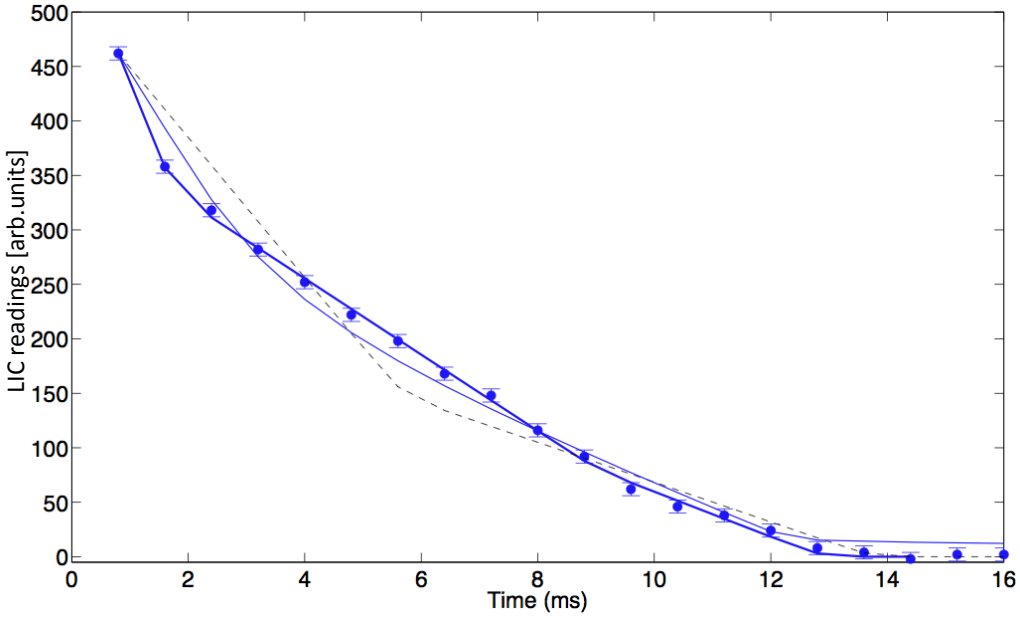

Figure 3.13: Charge collection for a single pulse, expressed in LIC reading versus time: experimental points (solid circles) and 2CC (dashed line), 3CC (thick solid line) and GCC (thin solid line) fits.

works ([75]), the extrapolation of the linear portion of the voltage-curve (V-curve) yields an intercept with the x-axis (intercept-to-slope parameter) that depends on LET. To quantify this parameter and relate it to LET, the general recombination (GR) effects should be accurately corrected for.

With the purpose of studying the behavior of the intercept-to-slope parameter as a function of beam quality, the 2-D array was irradiated in a water phantom at different dose rates with a proton and a carbon ion beam at the HIT Facility in Heidelberg [1].

The data have been summed-up on the whole matrix during the entire irradiation procedure. For protons, the V-curves have been measured only in one position (plateau, see fig. 3.14) as LET is expected to be the same everywhere, except for the very distal edge of the Bragg peak. For carbon ions, they have been evaluated in the Bragg peak and in the plateau (fig. 3.15 and 3.16), as a difference in LET is expected between the two regions. The lowest dose rates (or intensity levels, i#) available at HIT have been used: i3=2×10^8 part/sec, i4=3.2×10^8 part/sec, for proton, and i3=5×10^6 part/sec, i4=8×10^6 part/sec, i5=10×10^6 part/sec, for carbon. The voltage was varied from 400 to 1300 V, in steps of 100 V (for proton) and from 100 to

[1] by the time these studies were done, oxygen was not yet available at HIT

1300 V in steps of 200 or 100 V (for carbon). It was provided by an Iseg High Voltage Power Supply SHQ 224. The data have been normalized using an air-filled monitor chamber in front of the phantom, to account for variations from irradiation to irradiation. A linear fit of the linear part of the V-curves has been done to evaluate the intercept-to-slope parameter, corresponding to the intercept of the linear fitting line with the x-axis.

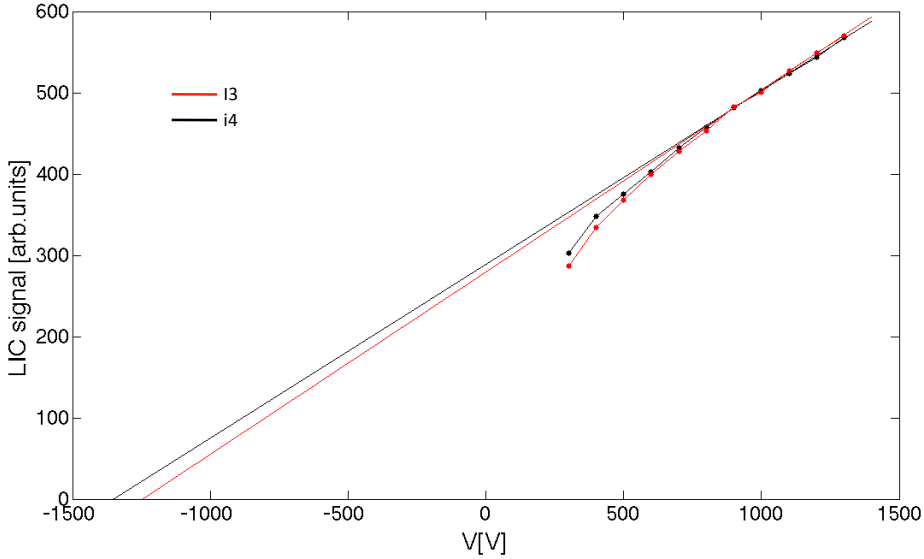

Figure 3.14: Voltage curves for a proton beam of energy 128.11 MeV at two different intensities (i3=2×10^8 part/sec and i4=3.2×10^8 part/sec) before applying the 3VM correction, and linear fits of the linear part of the curve using the points at V=900 and V=1300.

Both in the proton and in the carbon curves only a small dose-rate variation can be observed when comparing different intensity levels, as confirmed by the Fowler-Attix fit in figure 3.12. In all cases, the departure from linearity is due to GR and it is more pronounced for low voltages. To correct for such an effect and obtain a corrected signal, the collection efficiency f is calculated and the readings of the detector are divided by f at each voltage and for each single pixel.

The value of f could be calculated by the 2DR method or the 3VM (par. 2.4.2). They have both been developed and tested for low-LET radiation and a comparison between the two is discussed in [77], for different kind of radiation (pulsed and continuous), and for different dose rates. The authors claim not only that for pulsed beam the deviations between the 2DR and 3VM are larger with respect to continuous beams (where they are less than

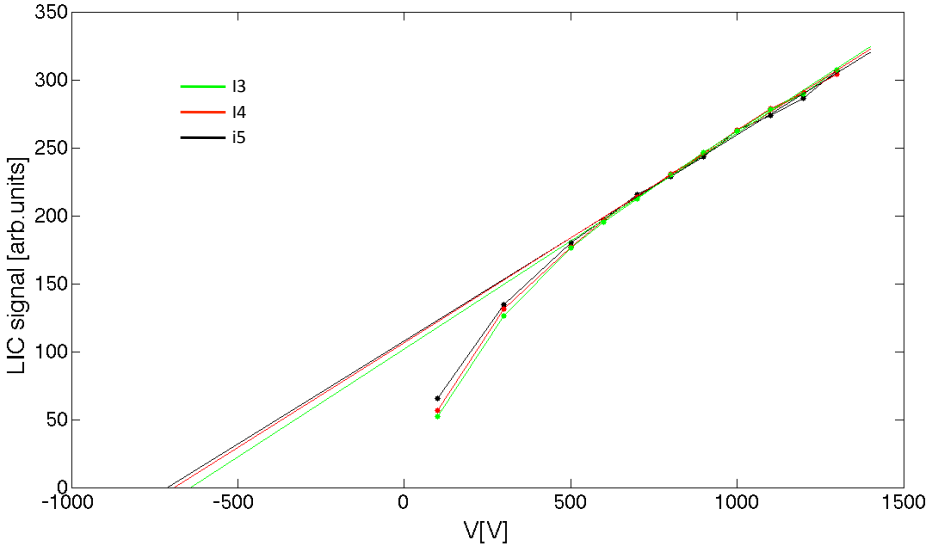

Figure 3.15: Voltage curves for the Bragg peak region of a carbon beam at three different intensities (i3=5×10^6 part/sec, i4=8×10^6 part/sec, i5=10×10^6 part/sec) before applying the 3VM correction, and linear fits of the linear part of the curve using the points at V=900 and V=1300.

7%), but also they observe that the numerical solution of the 3VM does not converge for all the triplets of voltages chosen,which is a sign of the intrinsic arbitrariness of the method.

The reason behind this is that the theory according to which IR is modeled in the 3VM (i.e. Onsager) might be a limiting factor, causing the deviations between the different results, while the 2DR methods, not requiring any modeling of IR, should not be limited to any specific radiation beam characteristics (e.g. LET). In particular, the problems related to the 3VM become important in both, the low and high polarizing voltage regimes: in low regimes f is below 0.9 and the theory of Greening is uncertain, while in high regimes, nonlinear effects intervene in the modeling of the IR. Nevertheless, as also emphasized in [78], the linear modeling of IR according to the Onsager theory should be sufficient for the radiation investigated.

In our case, the 3VM was used, for two main reasons: first of all, the 2DR method requires the use of a local monitor chamber, because the signal should be ideally measured at the same point with the LIC and the IC. Second, due to the different local dose-rate variations encountered in the radial beam direction, a pixel by pixel computation of f is needed, which means that to apply the 2DR method, a pixelized monitor in front of the

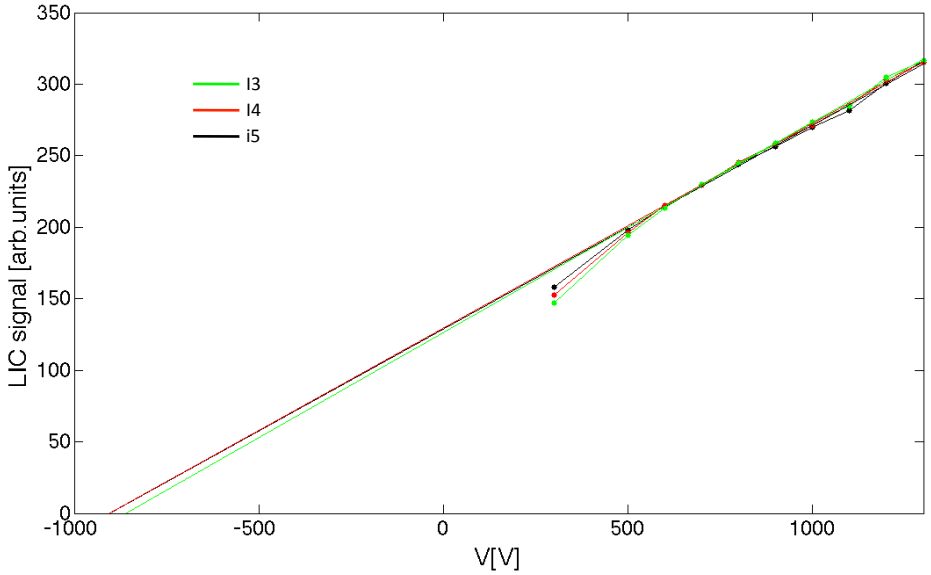

Figure 3.16: Voltage curves for the plateau region of a carbon beam at three different intensities (i3=5×10^6 part/sec, i4=8×10^6 part/sec, i5=10×10^6 part/sec) before applying the 3VM correction and linear fits of the linear part of the curve using the points at V=900 and V=1300.

LIC matrix and of its same dimensions is required. Unfortunately, such a pixelized monitor chamber was not available. Instead, a circular air-filled ionization chamber with radius 40.8 mm covering the whole matrix area (PTW Bragg peak chamber, *type* 34070) was used in the measurements. To apply the 3VM, no monitor is needed for the calculation of f, which therefore can be evaluated individually for each single pixel and the signal could be corrected accordingly. Protons and carbon ions were investigated, the latter in the Bragg peak and plateau position. The readings were corrected for each pixel and summed up, to obtain the correct readings for the whole matrix. In the evaluation of f with the 3VM a Matlab program was written to apply the 3VM simultaneously to all the 128 pixels: different triplets of voltages are chosen, avoiding voltages which are too high and too close to each other, as suggested by the authors. Due to the radial dose gradient, dose rate variations are seen by the different pixels: this causes a different weight of GR from pixel to pixel and, consequently, a different efficiency of the 3VM. Depending on the voltage triplets chosen, f varies from a minimum of 0.80 to a maximum of 0.99 (in some cases, due to the non-convergence of the 3VM, values of f >1 are obtained: in these cases, other voltage values were chosen manually in the calculations).
Once the f for all the 128 pixels have been obtained, the readings are adjusted to obtain the corrected V-curves. The intercept-to-slope parameters were evaluated by fitting the linear part of the V-curves of protons and carbon at three different intensities taking into account the voltage ranges of 900-1300 V. The values before and after the correction are reported in Table 3.2.

Intensity	p	p_{CORR}	c_{PL}	$c_{PL-CORR}$	c_{BP}	$c_{BP-CORR}$
I_c=i4			903±24	1178±35	710±28	947±44
I_p=i3 I_c=i5	1170±59	2000±95	904±48	1161±38	689±41	905±36
I_p=i4 I_c=i6	922±42	1959±84	860±43	1367±41	640±34	993±30

Table 3.2: Evaluation of the intercept-to-slope parameters at two different intensities for protons (i3=2×10^8 part/sec, i4=3.2×10^8 part/sec) and for carbons (i3=5×10^6 part/sec, i4=8×10^6 part/sec, i5=10×10^6 part/sec) in the plateau (C_{PL}) and Bragg peak (C_{BP}) region, before (P, C_{PL}, C_{BP}) and after (P_{CORR}, $C_{PL-CORR}$, $C_{BP-CORR}$) the 3VM correction. The trend with increasing intensity observed in the not-corrected data vanishes (within error bars) after the 3VM correction.

From the table, it can be seen that the non-corrected data show a descending trend, with decreasing values from the lowest intensities to the highest. After the 3VM correction, this trend is no longer observed and the intercept-to-slope parameter shows quite a constant behavior within the error bars, calculated from the statistical deviations of repeated measurements. This indicates an efficient correction for GR by applying the 3VM.

At the same time, this method lacks robustness: uncertainties arise not only from the different f values obtained depending on the triplets of voltages chosen for the different pixels, as previously discussed, but also from the choice of the voltages chosen to fit the V-curves. A small change in the linear fit, due to the inclusion of a lower or an higher voltage in the voltage range, in fact, results in a big change of the intercept-to-slope parameter.

3.8 LET determination: the calibration curve

A more robust method relies again on the dependence of IR on LET and it exploits the different sensitivities of LICs and ICs to IR losses. While in LICs IR is significant, in ICs it can be approximately neglected. The new approach consists therefore in measuring the signal at any point along the depth dose curve both, with the LIC and an IC. Subsequently, the ratio IC/LIC can be calculated and directly related to the LET of the particles in each measuring point along the depth dose curve, calculated by Monte Carlo methods.

The goal of the method is to obtain a *calibration curve*, in which the ratio value IC/LIC is plotted against LET, in a one-to-one correspondence. This is, of course, an indirect LET measurement: distributions of LET and its variation with depth in water are simulated by using the Monte Carlo transport code FLUKA, able to treat the transport of particles through matter. In the next paragraphs the development of such a coupled-device, the details of the FLUKA calculations, and of the entire procedure are given.

3.8.1 Experimental setup

The experiments have been performed at the HIT Facility in Heidelberg, in the quality assurance (QA) room, where different experiments and beam tests can be carried on. The 2D-array was irradiated with proton, carbon and oxygen beams in a water phantom at different depths, with steps of 1 cm in the plateau region and of 1 mm in the Bragg peak area. The potential difference applied between the electrodes was 1300 V.

The experimental apparatus can be seen in figure 3.17.

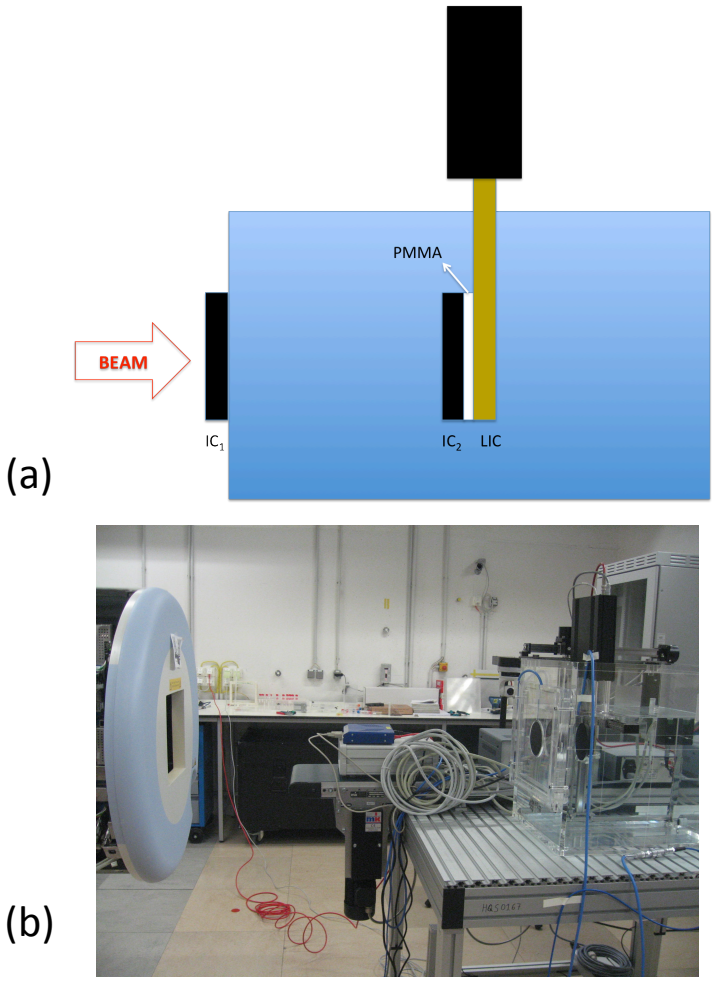

Figure 3.17: (*a*) Scheme of the experimental apparatus: the beam impinges on the water phantom from left. One can see, from left to right, the first Bragg peak chamber (IC_1), fixed outside the water phantom; then the complex IC_2 and LIC, hold together in the mobile holder, shiftable in depth and parallel to the beamline. IC_2 and LIC are separated by a PMMA layer. The picture is not to scale. (*b*) A photo of the experimental apparatus.

Two air-filled chambers (both of them are PTW Bragg peak chambers, *type* 34070) have been used:

- one in front of the phantom (IC_1), to monitor the dose entering the water phantom and to correct for fluctuations of the primary beam;
- one directly in front of the 2D-array (IC_2), to monitor the local dose.

The standard potential difference between the electrodes was 400 V for both of them. The IC_2 and the LIC were moved together in a custom made PMMA holder able to host the IC_2 and the 2D-array. As the latter is not water tight, the LIC was entirely and hermetically surrounded by PMMA, to prevent any water leak. This introduces an additional 2.41 mm PMMA wall between the IC_2 and the 2D-array, corresponding to a water equivalent distance of 2.87 mm.

Due to the sharpness of the Bragg peak, the positioning of the chambers in correspondence to the peak is quite challenging. Hence, to widen the Bragg peak, an additional passive energy spreading device, a ripple filter, was inserted in the beamline. The one used at HIT is a stationary mini ridge filter that generates a small but exactly defined modulation effect, via the multiple scattering in the ridge filter itself. The total effect is the broadening of the peak connected with a shift to lower depth [85]. The ripple filter was employed only for carbon and oxygen, because in the case of protons at energies greater than 100 MeV the pristine Bragg is much wider than for carbon and oxygen and the effect would be only a marginal increase of the full width half maximum (10%) [86].

3.8.2 LET calculation with the Monte Carlo method

The FLUKA Monte Carlo code is able to describe particle transport and interaction with matter [116], [117].

Besides incorporating all the main electromagnetic physical processes as described in Chapter 1, it has been improved to treat hadronic interactions up to 10000 TeV [32] as well and it has also been thoroughly benchmarked against other models and experiments specific to particle therapy [81], [83].

In FLUKA, the transport of charged particles is performed trough a multiple Coulomb scattering algorithm [79] and the treatment of ionization energy loss is based on the first Born approximation combined with a statistical approach able to produce well the average ionization and fluctuations such as energy and angular straggling [80]. In addition, effective charge parametrizations are employed.

A complete description of the FLUKA code can be found elsewhere [84].

The fluences for proton, carbon and oxygen beams at the energies used in the experiments were scored and integrated over a parallelepiped of the same dimensions as the LIC matrix and are represented in figures 3.18, 3.19 and 3.20, respectively (*courtesy of A. Mairani and K. Parodi*).

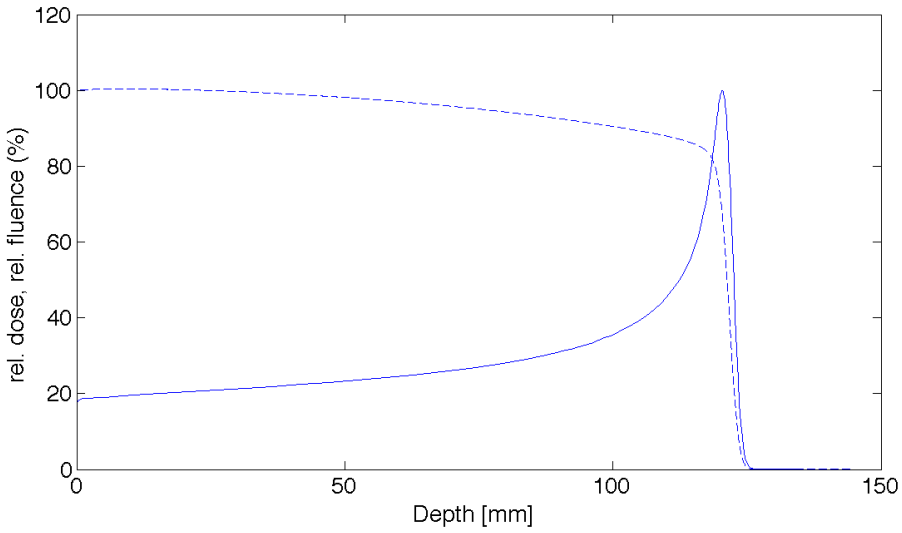

Figure 3.18: Dose (—) and fluence (· · · · · ·) for a 128.11 MeV proton beam.

The depth-dependent fluence is normalized to the primary entrance fluence. From figures 3.18, 3.19 and 3.20 it is clear that the fluence is not constant due to the nuclear interactions which give rise to a changing particle spectrum all along the depth. This is particularly important for heavy ions, where various light fragments contributing to the total dose are produced. For this reason, average values are commonly used instead of pure LET values.

3.9 LET averages

When considering one single particle traveling through matter, its LET can be directly calculated through equation 1.11. But in a physical beam, where many different particles are contributing to the dose deposition, e.g. after nuclear fragmentation, there is a certain distribution of the particle's LET. It is then reasonable to calculate an average LET that represents the LET distribution of the beam at a given depth. Average values can be expressed in different ways. The two standard modes are the *fluence* or *track averaged*

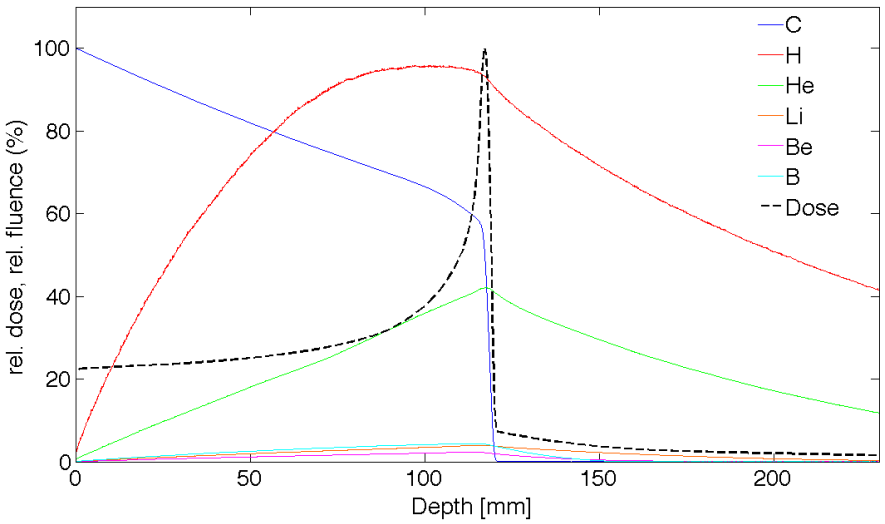

Figure 3.19: Dose and fluences for a 241.84 MeV/u carbon beam.

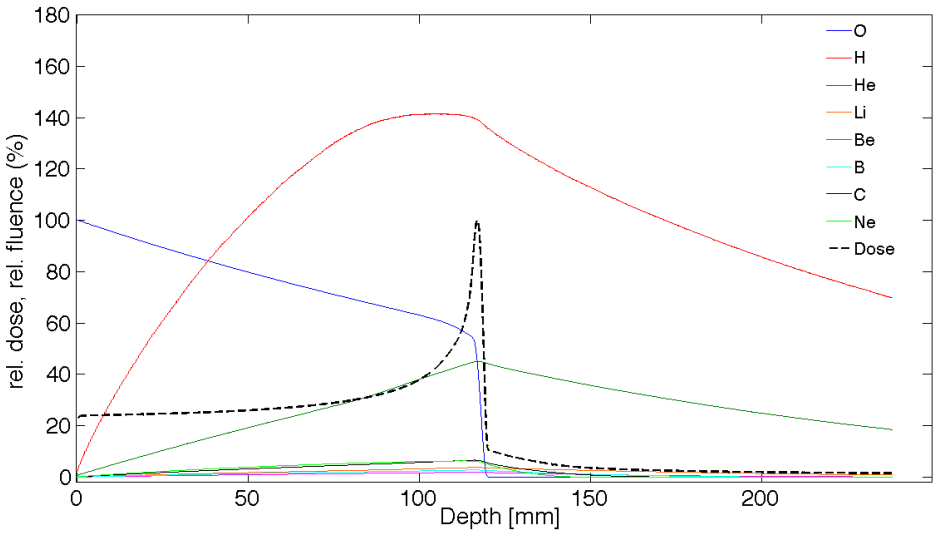

Figure 3.20: Dose and fluences for a 286.05 MeV/u oxygen beam.

LET and the *dose averaged LET*, depending on the physical quantity used to weight LET [46]:

- fluence averaged LET can be expressed in its integral form:

$$LET^F = \int_0^\infty t(L) LET dL \tag{3.8}$$

or:

$$LET^F(x) = \frac{\sum_{j=1}^n LET_{t,j}(x)\Phi_j(x)}{\sum_{j=1}^n \Phi_j(x)} = \frac{\rho}{\Phi(x)} \sum_{j=1}^n D_j(x) \tag{3.9}$$

where t(L) is the track length distribution and t(L)dL corresponds consequently to the fraction of the total track length having that LET. The second equality is justified by equation 1.10. Fluence-averaged LET means that the contribution of each particle type j is weighted by its fluence;

- the dose averaged LET is expressed as:

$$LET^D = \int_0^\infty d(L) LET dL \tag{3.10}$$

or:

$$LET^D(x) = \frac{\sum_{j=1}^n LET_{d,j}(x) LET_{d,j}(x)\Phi_j(x)}{\sum_{j=1}^n D_j(x)} = \frac{1}{D(x)} \sum_{j=1}^n LET_{d,j}(x) D_j(x) \tag{3.11}$$

where d(L) is the absorbed dose distribution, so that d(L)dL corresponds consequently to the fraction of the total dose having that LET. Dose-average LET means that the contribution of each particle is weighted by its contribution to the dose, therefore, particles which are responsible for an higher amount of dose deposition have a higher weight in the averaging process.

There is no universal agreement in the scientific community on which is the best way of averaging LET: depending on the applications and the schools of thought one average is adopted instead of the other. For this reason, in this work, both, the dose and fluence averaged LET will be considered and compared. The LET calculations shown take into account ionization energy

loss, multiple Coulomb scattering and nuclear fragmentation reactions. In the case of carbon and oxygen, the ripple filter was implemented in the FLUKA calculations.

The depth dose curves and relative dose and fluence averaged LET are represented in figures 3.21, 3.22 and 3.23 for the different particles and energy levels used.

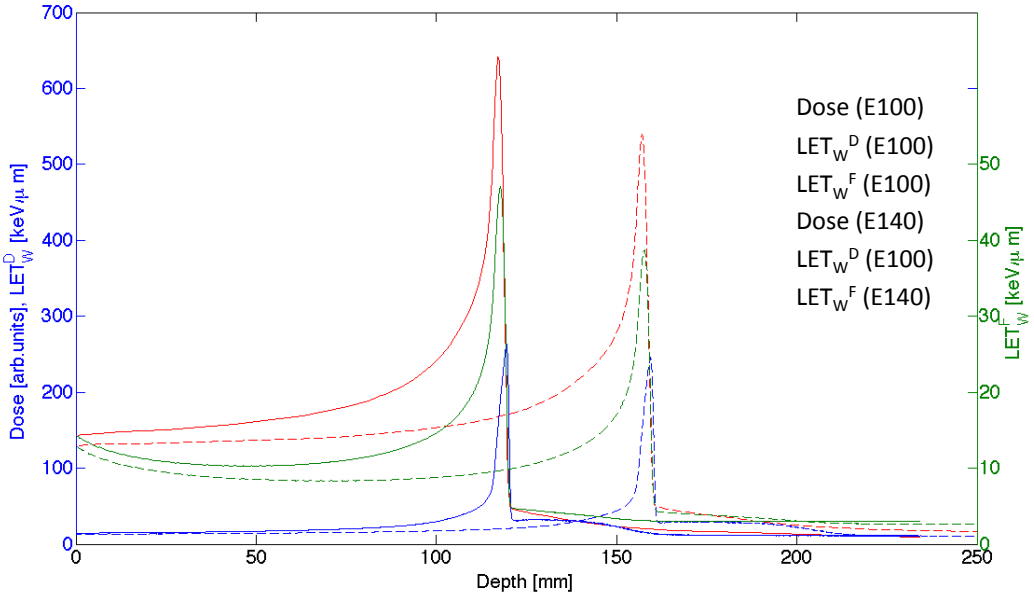

Figure 3.21: Depth dose curve, dose averaged LET (LET_W^D) and fluence averaged LET (LET_W^F) for carbon beams at two different energy levels (E100 and E140, *see table 3.1*).

The energy levels represented are E100 and E140 (see Table 3.1). The different particle species (figs. 3.21, 3.22, 3.23) with the same energy level have the Bragg peak at about the same position. As for protons the ripple filter is not used, the peak is located at a higher depth with respect to the other two.

Considering one particle species, the Bragg peak position and the dose averaged LET position are not located at the same depth, but the LET peak is shifted towards the very distal edge of the dose peak, which means that LET keeps on increasing beyond the Bragg peak. This effect is due to the straggling: the slightly more energetic particles stop behind the Bragg peak with a very low energy, being at the end of their path. Therefore, they have a very high LET, which makes the LET curve increase, even if they are in a very limited number (for this reason, statistics becomes very poor in this region and the curves are more noisy).

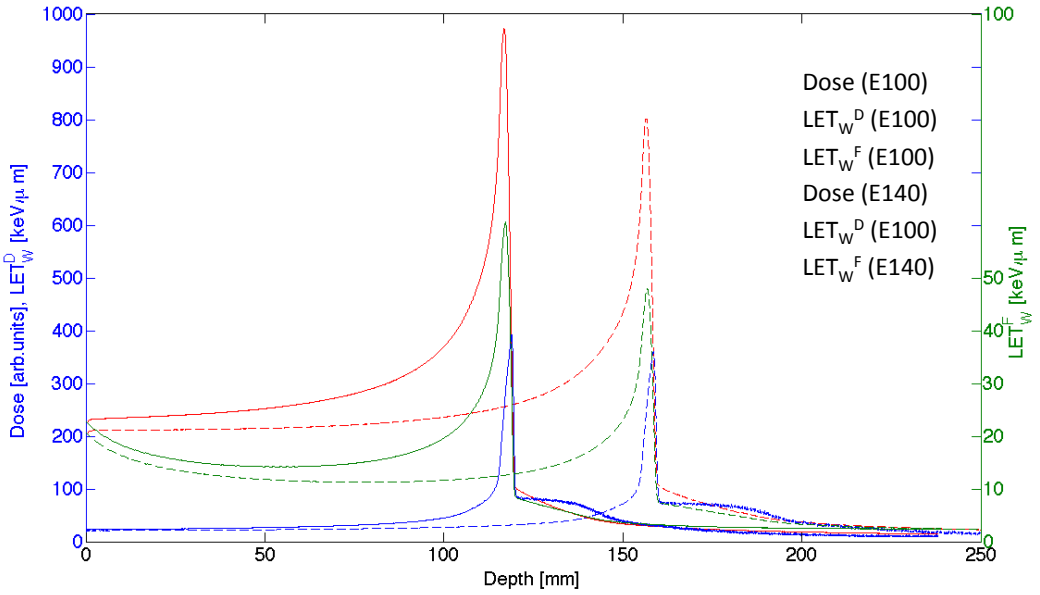

Figure 3.22: Depth dose curve, dose averaged LET (LET_W^D) and fluence averaged LET (LET_W^F) for oxygen beams at two different energy levels (E100 and E140, *see table 3.1*).

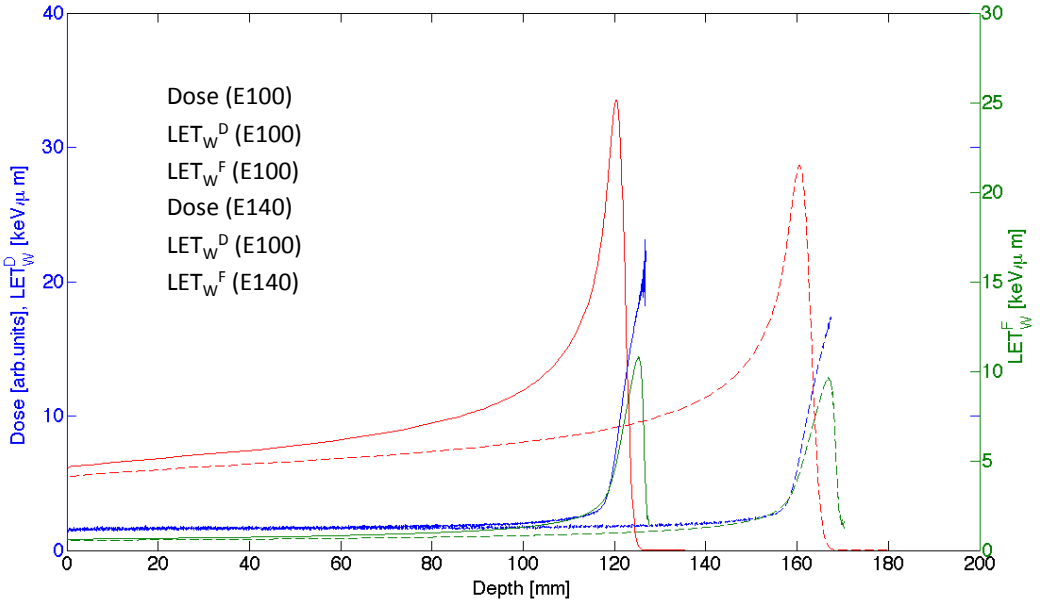

Figure 3.23: Depth dose curve, dose averaged LET (LET_W^D) and fluence averaged LET (LET_W^F) for proton beams at two different energy levels (E100 and E140, *see table 3.1*).

3.10 Estimation of the collection efficiency f

Before calculating the ratio IC/LIC a correction for GR losses should be performed on both chambers, as previously discussed (par. 3.8). Because of the afore-mentioned difficulties related to the application of the 3VM, the lowest dose rate has been chosen for taking the calibration curves in order to minimize the GR losses and no other correction has been applied to the LIC measurements. Whereas in air-filled chambers IR is not important at all in low-LET regimes, this is not anymore totally true for high-LET regimes, where IR becomes more important. The effect is, anyway, not as big as in LICs and the small correction needed to get rid of it is discussed. As will be seen in the following subsections, the calibration curve is not that sensitive to the corrections for GR losses - for IC and LIC - and IR losses - for IC - because the errors arising from the overall procedure generating the ratio IC/LIC are much more important. Before deciding to neglect them, details are given in the next subsections.

3.10.1 GR corrections for the 2D-array

The collection efficiency f, defined as the ratio between the current collected at a certain V and the saturation current, changes with depth, decreasing while going from the entrance channel towards the Bragg peak region, due to the higher production of charge in this area resulting in increased recombination. To apply the 3VM, therefore, a voltage curve at each depth is needed. An alternative solution is to calculate f (by using the 3VM) at one point where a whole V-curve has been measured and take this point as reference. Subsequently, $f{=}f(d_i)$ can be estimated at each depth performing an extrapolation of the f_{REF} calculated at the reference point. Details on the calculations are presented in the Appendix A.

The collection efficiency estimated for the central pixel hit by the center of the beam is shown in figure 3.24: some fluctuations of f can be observed, as only one pixel is taken into account and the signal is more prone to instabilities. Such instabilities in the LIC readings normally average out when all the pixels of the matrix are considered.

f decreases while approaching to the Bragg peak, as expected, because the amount of charges produced there and, therefore, the recombination is higher and f drops down. After the Bragg peak, the dose rate decreases rapidly and f increases and approaches 1. The decrease is only approximately 1% over the whole depth until the Bragg peak: as already anticipated, this is only a small variation and it will be neglected in the further analysis. For precise dosimetric evaluations, this extrapolation method can be of some utility and

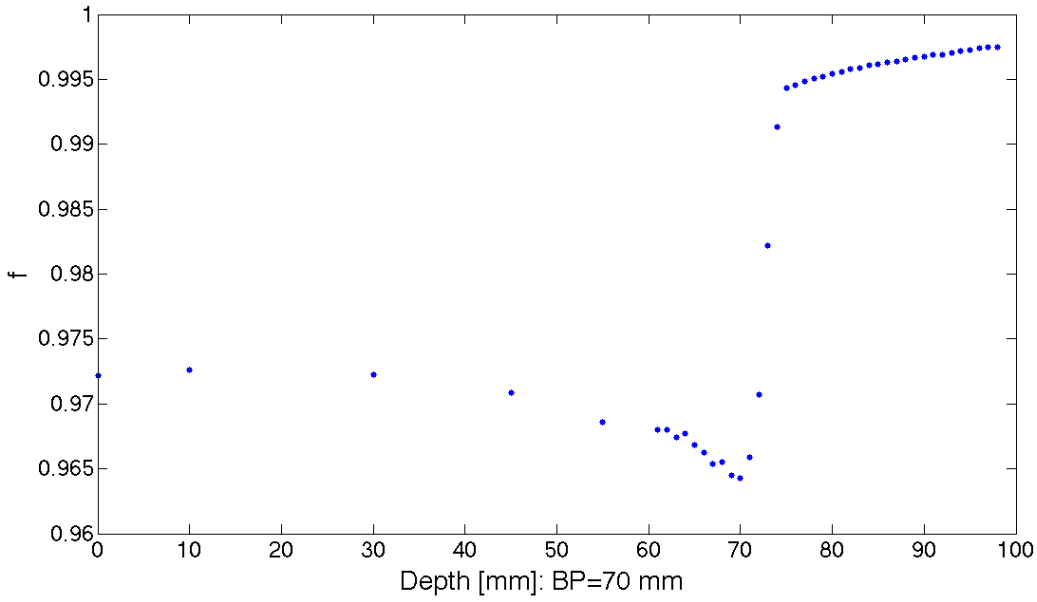

Figure 3.24: Collection efficiency f estimated for the pixel hit by the center of the beam. The chosen reference point is in the plateau region. Some fluctuations of f can be observed, as only one pixel is taken into account and the signal is more prone to instabilities.

an interested reader can refer to Appendix A.

3.10.2 Recombination in the air-filled IC

As reported by Kanai *et.al* [8], in the dosimetry of heavy-ion beams with air-filled ionization chambers, a correction due to initial recombination should also be taken into account. To evaluate such a recombination effect, which is usually considered insignificant in air-filled ICs ([9]), the behavior of the IC at different voltages has been studied for particle beams. An example for the V-curve evaluated with the IC irradiated at the Bragg peak position of a carbon beam of energy 241.84 MeV/u is shown in figure 3.25.

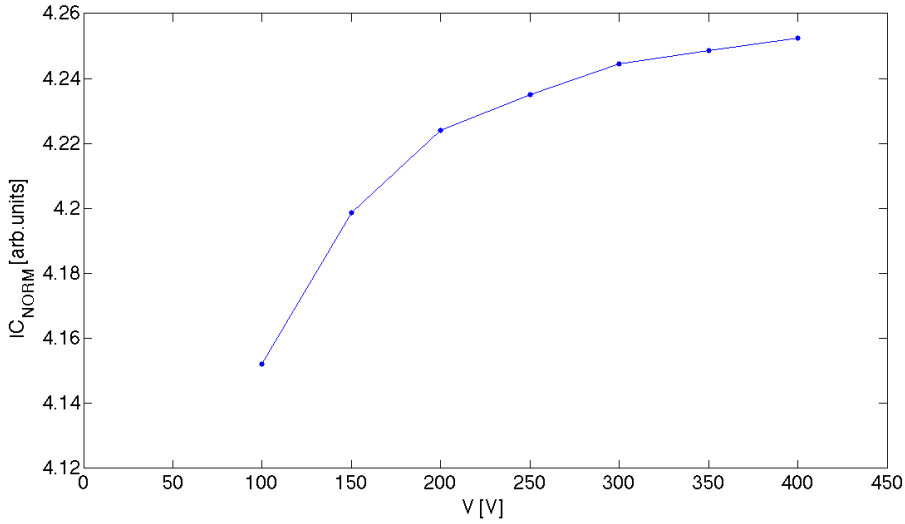

Figure 3.25: Voltage curve measured in the Bragg peak with the Bragg peak chamber (IC) for a carbon beam of E=241.84 MeV/u.

As explained in Chapter 2, the effect of GR is usually corrected for in ICs by using the 2VM, which assumes linearity between 1/Q and $1/V^2$ [5], [10]. It is clear from figure 3.26 that the trend observed in the case of a particle beam is far away from linearity.

Depending on the model published by Zankowski et al. ([7]), which takes into account the effect of GR, IR and ion diffusion, the relation between the charge Q, the saturation charge Q_{sat} and the voltage V is given by:

$$\frac{1}{Q} = \frac{1}{Q_{SAT}} + \frac{\alpha}{V} + \frac{\beta}{V^2} \tag{3.12}$$

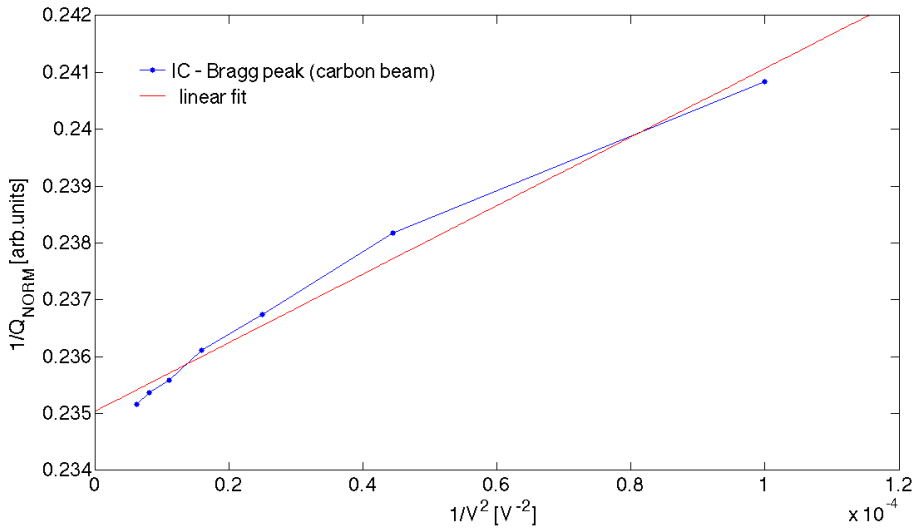

Figure 3.26: A plot 1/Q vs $1/V^2$ for a carbon beam at the Bragg peak position. Data are normalized using an air-filled monitor chamber in front of the phantom, to account for variations from irradiation to irradiation. The trend shows a lack of linearity foreseen by Greening.

with α related to IR and diffusion and β including also GR losses (eq. 2.4.1). The total f (f_T), that takes into account collection efficiencies for initial recombination, general recombination and diffusion losses, is given by 2.13. Figure 3.27 represents the experimental data and a least-squares fit of equation 3.12 to the data set with α=(0.57±0.19) V and β=(16.07±14.97) V^2 and results in a Q_{sat}=(4.281±0.001) nC. As in [7], the data are plotted in the form 1/Q vs. 1/V because equation 3.12 provides a better agreement with measured data than does the 1/Q vs $1/V^2$ linear relationship.

At a given depth, the value of f_T depends on the voltage and it increases with it from f_T(100V)=0.947 to f_T(400V)=0.987. To understand the different contribution of α and β, and hence of IR, GR and diffusion, one can suppress one of the two terms and evaluate the weight of the other one. In this respect, when switching the GR off (β =0), the expression for f associated to IR and diffusion (f_i) has the form:

$$f_i(V) = \frac{V^2}{V^2 + \alpha V Q_{sat}} \tag{3.13}$$

with values ranging from f_i(100V)=0.953 to f_i(400V)=0.988. When switching the IR off (α =0), the expression for f associated to GR (f_g) has the form:

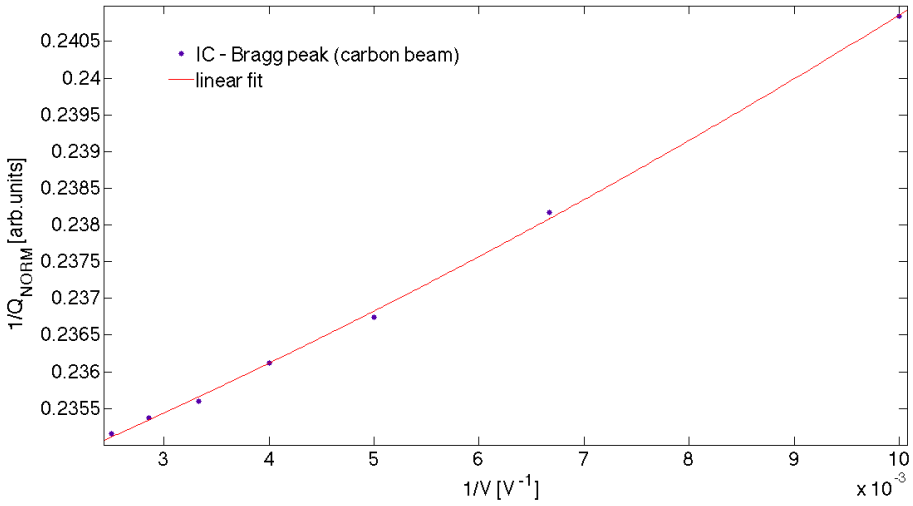

Figure 3.27: A plot of the saturation data in the form 1/Q vs 1/V for a carbon beam at the Bragg peak position. Data are normalized using an air-filled monitor chamber in front of the phantom, to account for variations from irradiation to irradiation. The fit corresponds to the least-squares fit of equation 3.12 to measured data in the range from 100 V to 400 V, with α=(0.57±0.19) V, β=(16.07±14.97) V^2 and Q_{sat}=(4.281±0.001) nC.

$$f_g(V) = \frac{V^2}{V^2 + \beta Q_{sat}} \tag{3.14}$$

with values ranging from f_g(100V)=0.993 to f_g(400V)=0.999, meaning that the GR is very small and that the bigger part is carried by the IR.

The value of f calculated with equation 2.13 and with the 2VM in the Bragg peak (fig. 3.26) are respectively f_T=0.987 and f_{2VM}=0.994. The two values differ due to the fact that, when the contribution of IR becomes important, the assumptions on which the 2VM is developed are no longer strictly met.

In case of a high-LET beam, therefore, the collection efficiency was calculated with equation 2.13.

3.10.3 Evaluation of the corrections for IR and GR

In absolute dosimetry the dose has to be measured very accurately and most dosimetric protocols require corrections for recombination effects. This is the reason why a lot of discussions arose in the literature to develop proper correction methods to account for recombination losses. Correction factors have been evaluated also in this work, to judge about their importance in relation to our experimental data. As shown in the previous paragraph, such corrections do not play a big role: in the LIC, GR losses vary only by less than $\sim$1% in depth until the Bragg peak and are responsible for f values around 0.97. In the IC, losses coming from GR, IR and diffusion are contributing all together to a value of f of 0.987, at the voltages used in the experiments.

As the effect of GR (in the 2D-array) and of IR and GR (in the IC) losses is small compared to the experimental uncertainties of the calibration curve procedure, none of the discussed correction has been incorporated in the data presented in the next sections. Despite this, the ratio IC/LIC is still mainly characterized by the difference in IR between the LIC and the IC, which is the main factor that suppresses the LIC curve, compared to that of the IC.

3.11 Proton, carbon and oxygen data

The LIC and IC curves, i.e. the measured detector signal as a function of the depth of the detectors in the water phantom along the beam propagation, are illustrated in figure 3.28. To evidence the different amount of peak suppression due to recombination (quenching) and only for this purpose, they have been normalized to the entrance channel, which therefore is 1. The depth in water is expressed as a relative depth because the zero position in the graph

does not coincide with the entrance wall of the phantom. This is due to the materials in front of the measuring position of the LIC (the IC_2, the holder and the PMMA belonging to the LIC, as depicted in figure 3.17) and also to a space left between the IC_2 and the phantom wall, as a precaution taken in case of errors of the remotely controlled moving device.

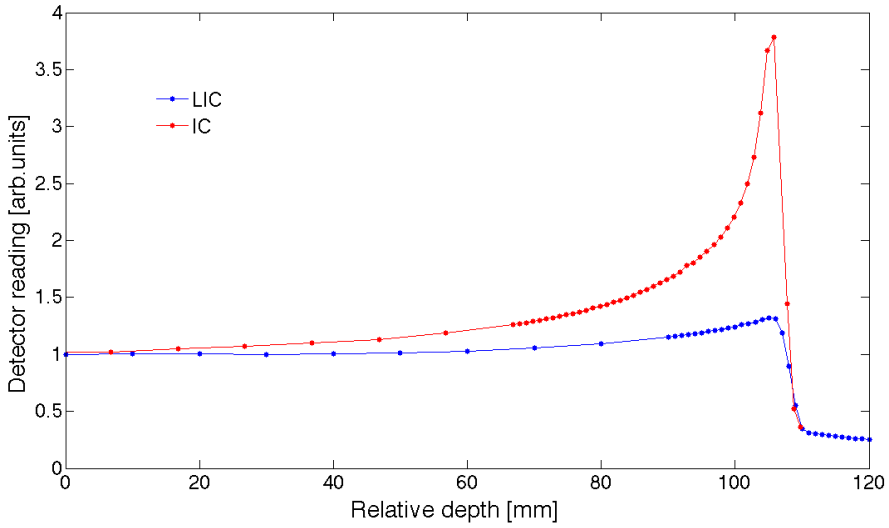

Figure 3.28: The data of LIC and IC are shifted to have the maxima of the depth dose curve at the same position. The higher amount of quenching of the LIC curve due to the increased IR to which the LIC is prone is clearly visible. The full circles are data points, the lines are spline interpolant fit to the data and are used to guide the eye.

All the data sets are always normalized to the monitor in front of the phantom (which measures charge in nC), to take into account the variations from irradiation to irradiation at the different depths.

After this normalization procedure, the resulting IC normalized data are expressed without units, as they are given by dividing two numbers both, measured in nC. The LIC normalized data, instead, are given by dividing the LIC data (expressed in ADC counts, which are proportional to the collected charge) and the monitor chamber data (nC). The conversion factor from ADC to nC is not known for the XDAS used in this 2D-array. Therefore, the $ADCs$ have not been converted in nC and the normalized values are given in arbitrary units.

The ratio between the IC and LIC normalized curves, IC_{NORM}/LIC_{NORM} will be called from now on the *recombination index* and it will be given in arbitrary units for the same reasons mentioned above. The first step for

the calculation of the recombination index is the shift of the two curves, one respect to the other, along the relative depth coordinate. Due to the different shapes of the two depth dose curves and to the uncertainty related to the water equivalent thickness of the exit window of the IC, shifting of the LIC and IC, one respect to the other is not straight forward. To account for such uncertainties, two methods have been applied: a first one, where the 50% dose fall-off of the two curves coincide, and a second one, where the two measures in the respective peaks coincide (fig. 3.29). For better illustration, all curves are normalized to the respective peak maxima, identified by a shape-preserving interpolant fit to the data.

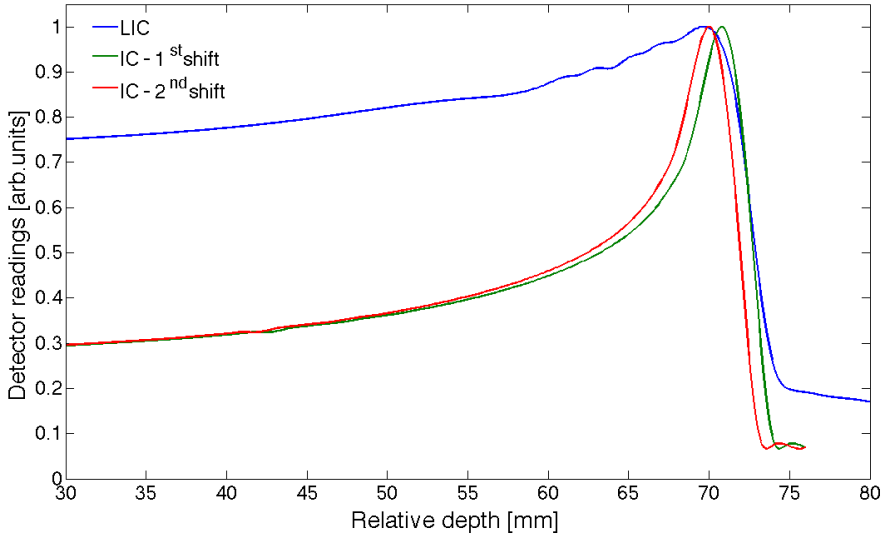

Figure 3.29: The main source of error is coming from the uncertainty in the shift of the LIC and IC curves, therefore, the error bars are the standard deviation of the peak shift and the 50% fall-off shift (see text for definitions).

To provide one value at each depth with its error, the two recombination indices have been calculated using both shifts, then averaged and the standard deviation was used as error bar.

As already mentioned in paragraph 3.7, the experimental setup was not the optimal one. Unfortunately, within the scope of this thesis, this could not be improved in a further experiment due to limited available beam time. The discrepancy between the IC and the 2D-array is due to the fact that the IC area was completely covering the beam section, while the LIC only covered the central part of it. The LIC reading is therefore not complete, contrary to the IC reading, and this affects the ratio calculation. Fortunately,

this happens only along the short side of the matrix, which is in the vertical direction. Along the horizontal axis, the beam is completely inside the matrix area, as represented in figure 3.30).

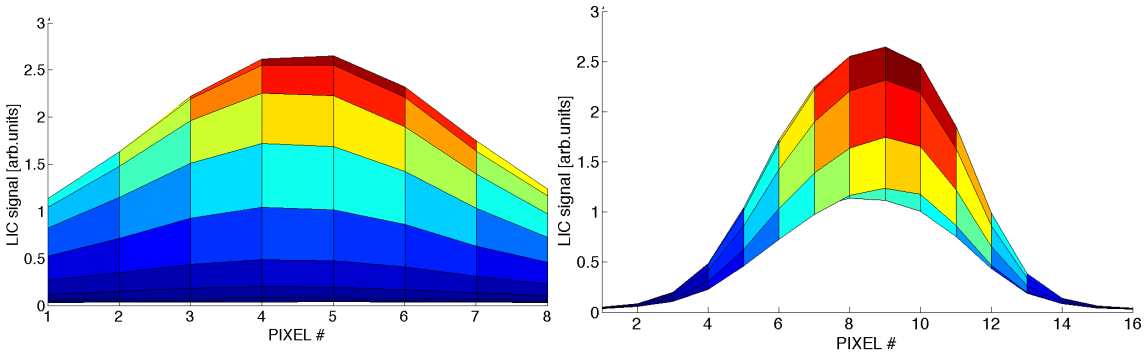

Figure 3.30: Beam impinging on the matrix: while in the horizontal direction the beam extension is entirely contained in the matrix (right) this is not the case in the vertical one, where the beam exceeds the matrix dimensions (left).

The same procedure was used to generate horizontal error bars with respect to the positioning of the LET curve. Here the LET value corresponding to the maximum of the dose is placed at the same position as the maximum of the LIC depth dose curve.

To take into account also the portion of the beam outside the matrix in the vertical direction, a simple geometrical estimation of the beam tails has been done by considering a linear slope passing through the two pixels closest to the edges of the matrix (fig. 3.31). This procedure has been performed for each row of pixels in the vertical direction, for all depths. A fitting procedure (e.g. double Gaussian fit) could also have been done. However, there were cases in which the fluctuations in some pixels made the fits problematic and an automatized procedure to evaluate the single fits for all the rows was difficult to implement. Again, such deviations from a perfect fit were considered negligible with respect to the errors coming from the shifting procedure. Therefore, the geometric evaluation was taken to be accurate enough and implemented.

In the calibration curves obtained after all the corrections described before, the recombination index is plotted against the calculated LET for each depth along the depth dose curves. Both the dose averaged and the fluence averaged LET are considered. Two different energies have been considered

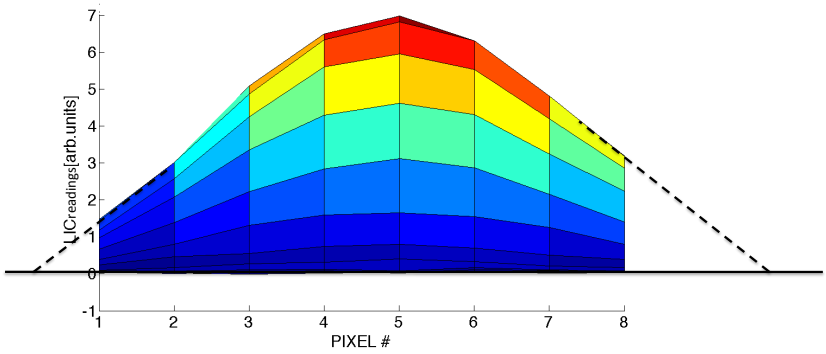

Figure 3.31: Estimation of the part of the beam exceeding the matrix: to the first order, it can be approximated with a linear slope.

for proton, carbon and oxygen beams. The calibration curves are plotted for the LET values all along the depth dose curve, but only until the Bragg peak. Beyond it, statistics become very poor and the averaging procedure lacks reliability.

Proton calibration curves

The proton calibration curves for dose averaged LET (LET_W^D) and fluence averaged LET (LET_W^F) are depicted in figure 3.32 and figure 3.33, respectively.

A clear difference between the LET_W^F curve and the LET_W^D curves can be observed. As compared to the heavier projectile ions, however, the maximum LET values close to the Bragg peak are quite similar for both averaging methods and only differ by a factor of about 1.5. This is due to the fact that the two averaging procedures for protons are quite similar, as no projectile fragmentation process take place. The dose is mainly carried on by the primaries. Surprisingly, for both averaging methods, significant deviations in the recombination index at the same LET but for different energies can be observed and no unique, projectile-energy independent calibration curve can be extracted within the experimental error bars at medium LET values. The reason for this is unclear, but it mainly depends on the averaging procedure applied. Nevertheless, taking the mean value between both projectile-energy curves the calibration is within $\pm 10\%$ for energies between 128.11 and 150.55 MeV.

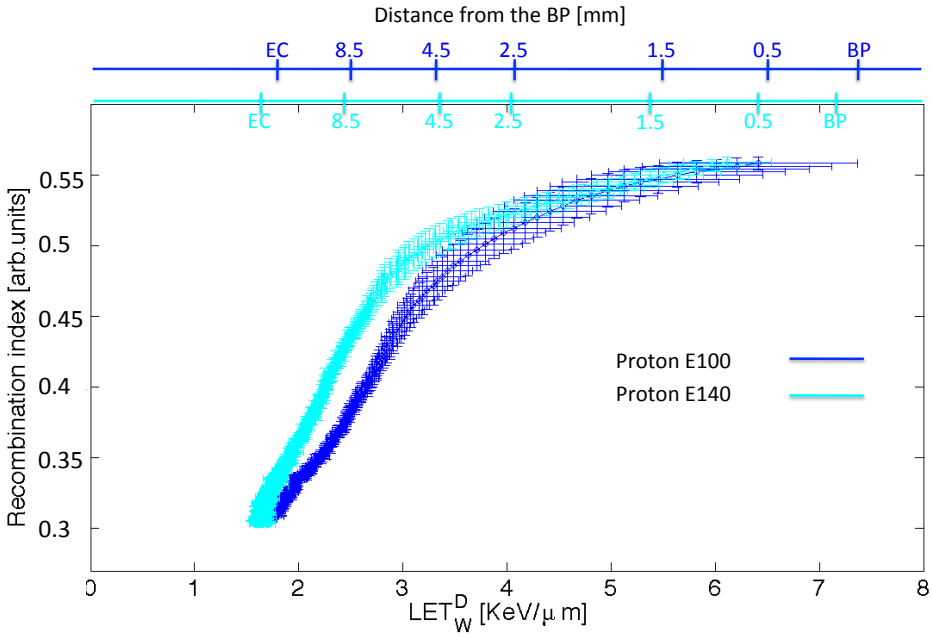

Figure 3.32: Recombination index vs. dose-averaged LET (LET_W^D) for the proton beam at two different energies (E100=128.11 MeV and E140=150.95 MeV/u). The distance from the Bragg peak (BP) is shown in relation to the LET, until the entrance channel (EC) as upper horizontal scale.

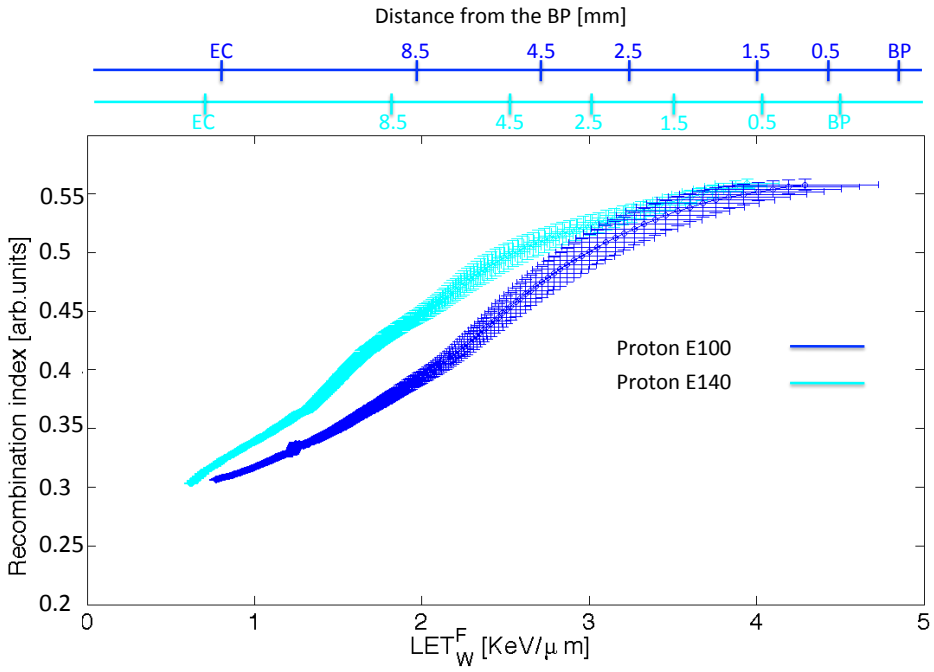

Figure 3.33: Recombination index vs. fluence-averaged LET (LET^F_W) for the proton beam at two different energies (E100=128.11 MeV and E140=150.95 MeV/u). The distance from the Bragg peak (BP) is shown in relation to the LET, until the entrance channel (EC) as upper horizontal scale.

Carbon calibration curves

The carbon calibration curves for dose averaged LET_W^D and fluence averaged LET_W^F are depicted in figure 3.34 and figure 3.35, respectively.

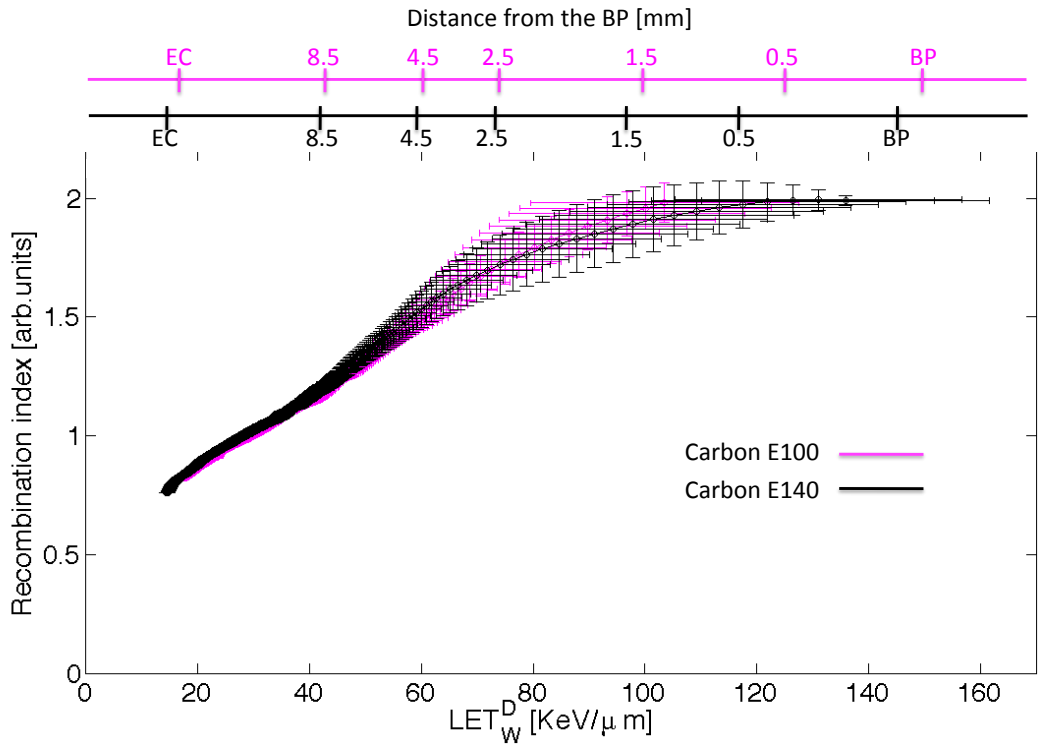

Figure 3.34: Recombination index vs. dose-averaged LET (LET_W^D) for the carbon beam at two different energies (E100=241.84 MeV/u and E140=283.76 MeV/u). The distance from the Bragg peak (BP) is shown in relation to the LET, until the entrance channel (EC) as upper horizontal scale.

In the case of carbon beams, the situation is different and the LET_W^D and LET_W^F curves have a different trend. The LET_W^D curves show energy independence, with the two curves at E100 and E140 one on the top of the other within the error bars. They are characterized by a shoulder for those LET values towards the Bragg peak area. The LET_W^F curves show, instead, an energy dependence, with the higher energy curve above the lower energy one. In this case, their trend is quite linear. Not only the curve shape, but also the LET_W^D and LET_W^F ranges are quite different for carbon ions. This is due to the fact that in the LET_W^D those particles that deposit more dose have more weight, while in the LET_W^F all the particles that carry a different amount

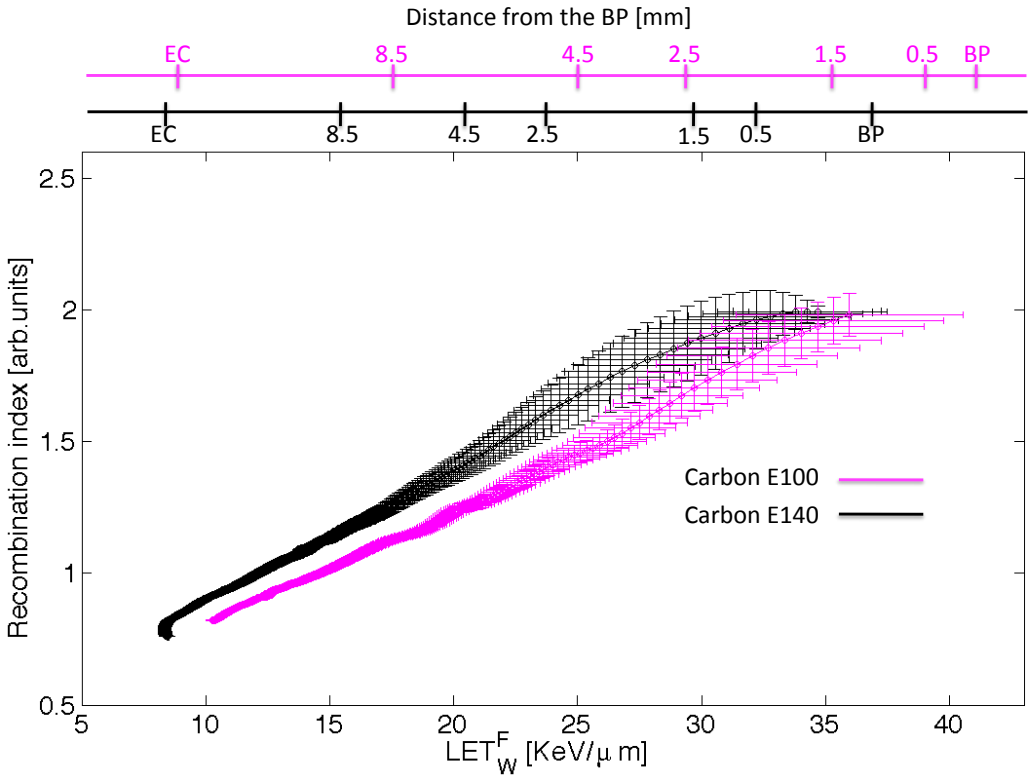

Figure 3.35: Recombination index vs fluence-averaged LET (LET_W^F) for the carbon beam at two different energies (E100=241.84 MeV/u and E140=283.76 MeV/u). The distance from the Bragg peak (BP) is shown in relation to the LET, until the entrance channel (EC) as upper horizontal scale.

of dose (and, therefore, are responsible for different biological damage) have the same weight, because the quantity that matters, here, is the fluence. LET_W^F shows, therefore, lower values because those species with a lower LET weight the same as those that have a very high LET.

Oxygen calibration curves

The oxygen calibration curves for dose averaged LET_W^D and LET_W^F are depicted in figure 3.36 and figure 3.37, respectively.

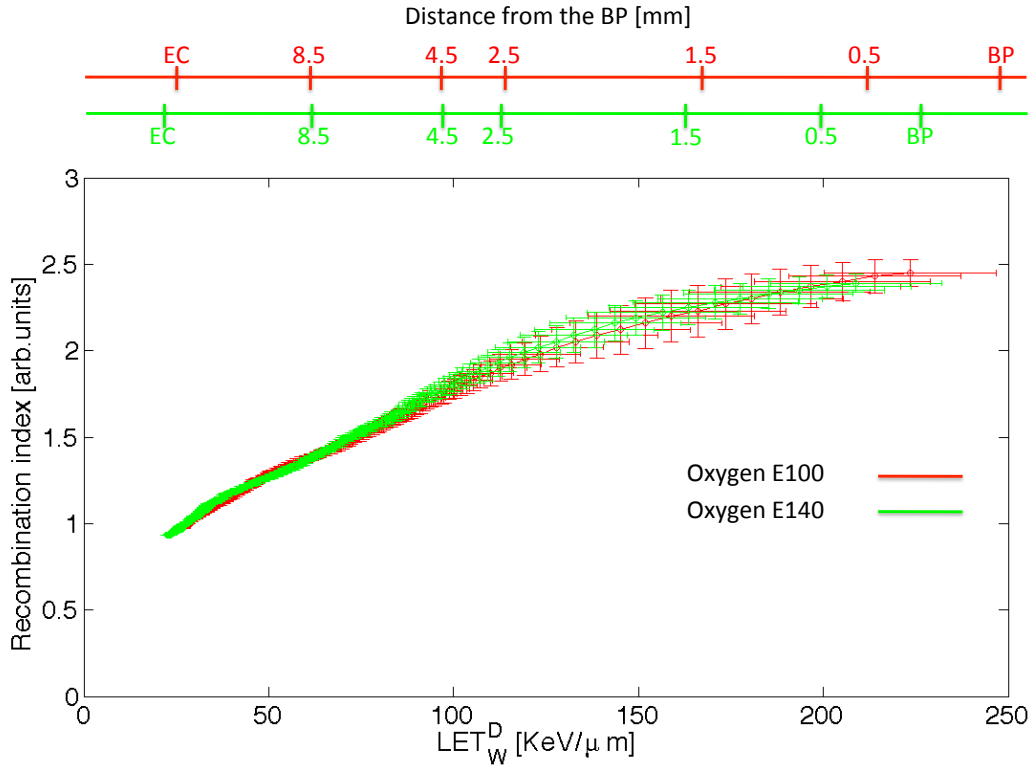

Figure 3.36: Recombination index vs. dose-averaged LET (LET_W^D) for the oxygen beam at two different energies (E100=286.05 MeV/u and E140=340.52 MeV/u). The distance from the Bragg peak (BP) is shown in relation to the LET, until the entrance channel (EC) as upper horizontal scale.

In the oxygen case, the main observations discussed for the carbon calibration curves are valid as well, except that the shoulder, which is so evident for carbon, is much more smooth and the trend is more linear. Moreover, the LET_W^D values are even higher, due to the fact that the oxygen particles have

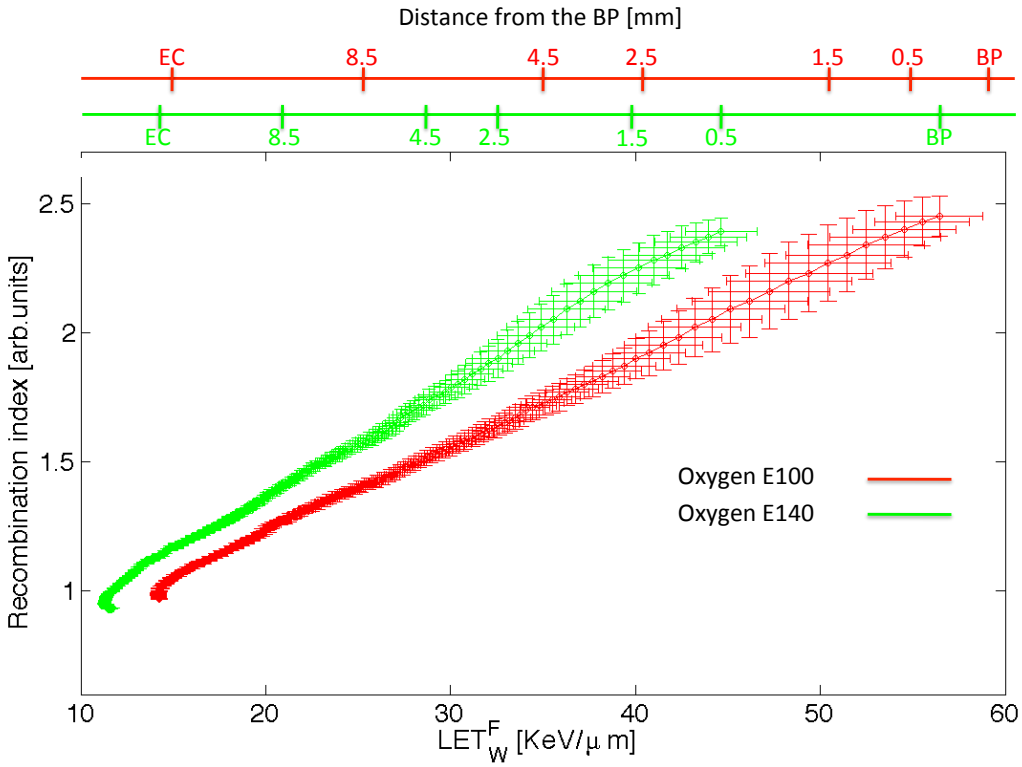

Figure 3.37: Recombination index vs. fluence-averaged LET (LET^F_W) for the oxygen beam at two different energies (E100=286.05 MeV/u and E140=340.52 MeV/u). The distance from the Bragg peak (BP) is shown in relation to the LET, until the entrance channel (EC) as upper horizontal scale.

a higher atomic number and charge (+8 compared to the +6 of the carbon beam).

All the calibration curves for protons, carbon and oxygen are represented in figure 3.38 and figure 3.39.

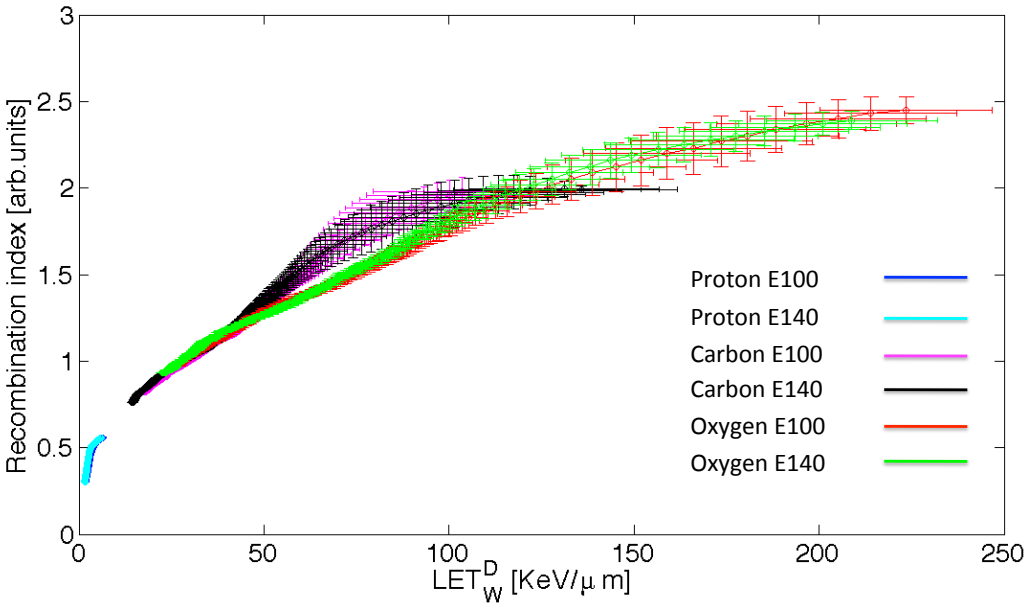

Figure 3.38: Recombination index vs. dose-averaged LET (LET^D_W) for the proton beam (E100=128.11 MeV and E140=150.95 MeV), the carbon beam (E100=241.84 MeV/u and E140=287.02 MeV/u) and the oxygen beam (E100=286.05 MeV/u and E140= 340.52 MeV/u).

In the LET^D_W the curves show a global trend which suggests that a unique calibration curve is valid - within the error bars - for all the species.

In the LET^F_W, the curves seem to be grouped depending on their energy levels, those with E100 being well separated from those with E140.

3.11.1 Antiproton data

The characteristics of the antiproton beam available at CERN are very different from those of the particle beams clinically used at HIT. Antiprotons are delivered with an energy of 126 MeV and in pulses, each one containing about 3×10^7 particles. Each pulse is 500 ns long and separated, typically, 90-120 seconds one from the other. Such a high number of particles per spill means that the dose rate is very high, compared to one of the typical dose

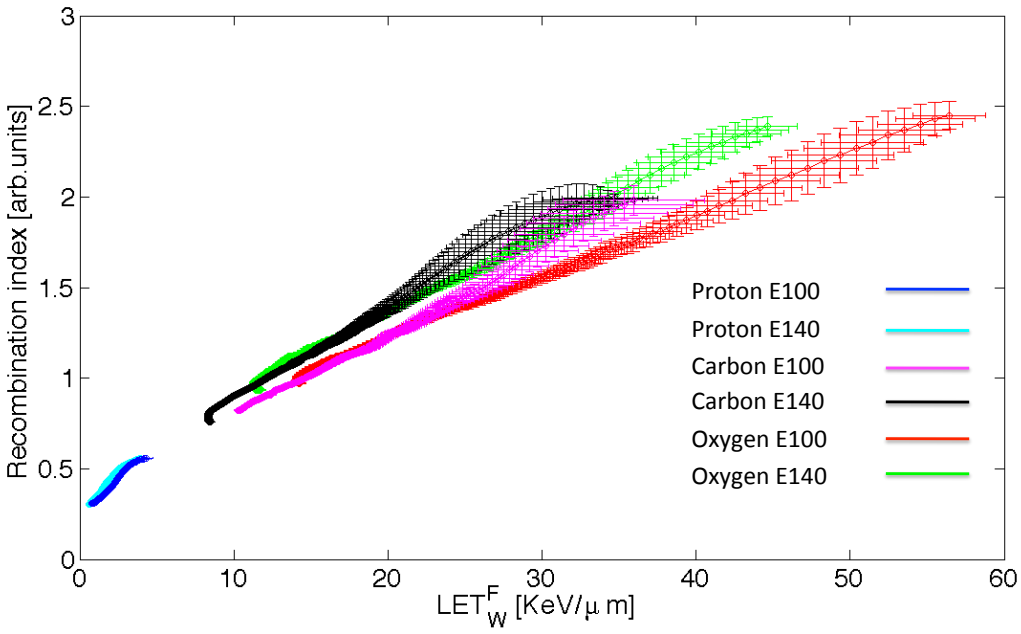

Figure 3.39: Recombination index vs. fluence-averaged LET (LET^F_W) for the proton beam (E100=128.11 MeV and E140=150.95 MeV), the carbon beam (E100=241.84 MeV/u and E140=287.02 MeV/u) and the oxygen beam (E100=286.05 MeV/u and E140= 340.52 MeV/u).

rates used at HIT (5×10^6 part/sec) and the recombination processes taking place in the sensitive volume are much more important at such a high dose rate.

The experimental setup for the antiproton experiments is the same as used at HIT, except for the two monitor chambers in front of the water phantom and attached to the 2D-array, which were in this case two *Advanced Roos Chambers*, instead of the Bragg peak chambers used at HIT. The *Advanced Roos IC* has a diameter of approximately 40 mm and a gap of 2 mm. Gafchromic films were used to determine the beam profile of the antiproton beam: the measured FWHM was approximately 8 mm in the entrance region. This means that the beam was fully contained in the IC. The standard potential difference between the electrodes was 400 V.

Sequences of 10 spills were measured with the 2D-array. The integration time was set to 200 msec and the number of subsamples was 4. The leakage current was always subtracted from the measurements. The beam was never stopped if some of the settings of the setup were changed (the position of the 2D-array in depth or the voltage applied to it). Thus, in order to be always in stable measurements conditions, the first two pulses have never been considered. Each of the remaining eight pulses has been integrated, normalized and the average of the eight spills was the outcome of the overall sequence.

One sequence is depicted in figure 3.40. A variation of the spill height during the same measurement is due to the different number of antiprotons per spill sent from the Antiproton Decelerator (AD). To account for such variations, the normalization with the IC in front of the phantom is required.

A zoom into one single pulse is depicted in figure 3.41. The real pulse is 500 ns long, but the charge collection in the 2D-array is much longer, due to the transit of the charge carriers towards the electrodes. The total collected charge is obtained by integration of the area under the pulse. After all the charge has been collected, the LIC reading goes back to zero.

The voltage curve has been measured in the Bragg peak and in the plateau position, for voltages from 400 V to 1300V, in steps of 200 V. The intercept-to-slope parameter was evaluated by fitting the linear part of the V-curve for the voltages from 700 V to 1300 V (figure 3.42).

As has already been observed by our colleagues of the AD-4 collaboration, the comparison of the asymptotic slopes of the curves shows a difference between those in the Bragg peak and in the plateau data sets. The voltage curves were measured during the 2011 run. In that year, the study of the intercept-to-slope parameter in relation to the LET was still in its first stages: although observing an LET dependence, a quantitative LET evaluation was

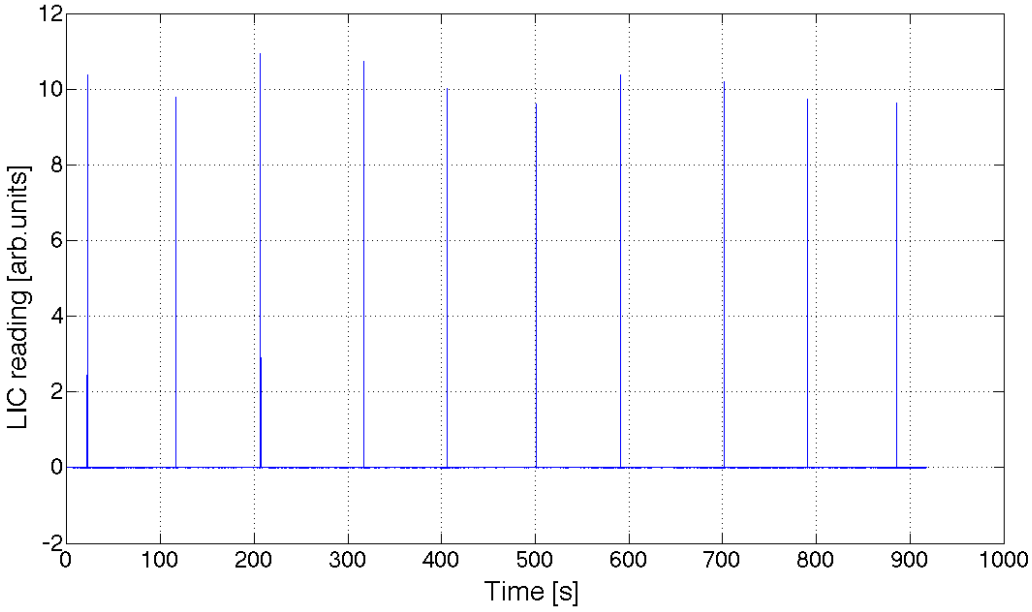

Figure 3.40: Antiproton (E=126 MeV) pulse sequence measured with the 2D-array. A variation of the pulse height is due to the different number of antiprotons per pulse. To account for such variations, the normalization with the IC in front of the phantom is required.

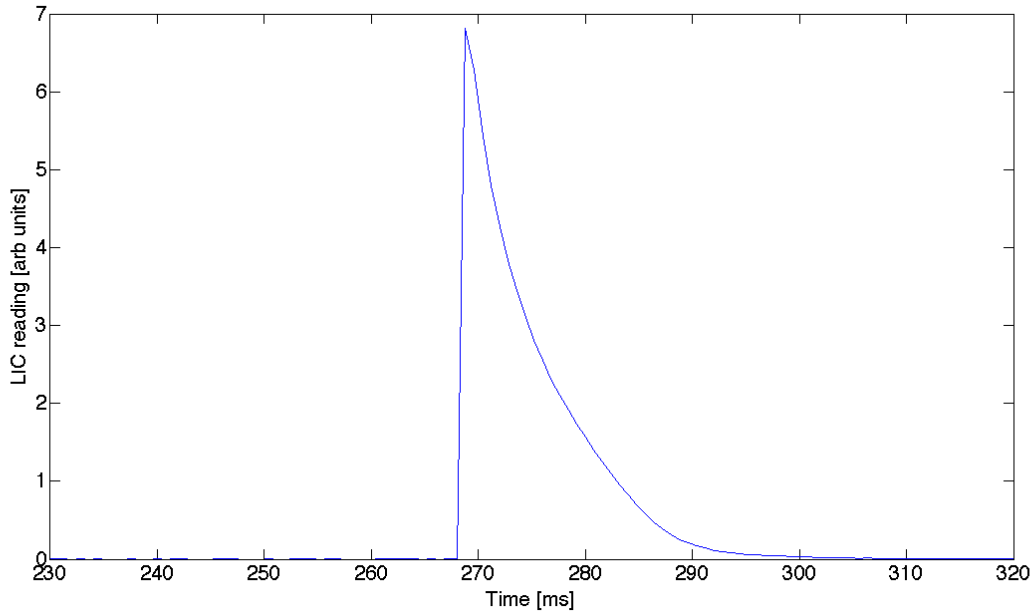

Figure 3.41: Antiproton single pulse (E=126 MeV) measured with the 2D-array. The voltage between the electrodes of the 2D-array was 1000 V.

not possible.

The setup was irradiated with antiprotons at two different dose rates on two different days. The high dose rate (HDR) was 6×10^{13} part/sec and the low dose rate (LDR) was 3×10^{13} part/sec. A factor of two between the two dose rates was obtained by sending a lower number of protons from the PS onto the production target. The antiproton depth dose curve was measured by manually shifting in depth the 2D-array. The measured curves are represented in figure 3.43 and the data points have been connected by a spline to guide the eye.

It can be observed that the depth dose curve at the high dose rate (in red in fig. 3.43) is suppressed with respect to the one at low dose rate. This effect is due to the higher amount of general recombination (GR) in the LIC in the high dose rate measurements, which lowers the LIC reading. A correction method for GR would be necessary, which, however, was not feasible on the basis of the available data within this thesis.

The calibration curve was evaluated also for the antiproton beam. Unfortunately, it was not possible to change the antiproton energy, therefore, two depth dose curves have been measured at the two different dose rates

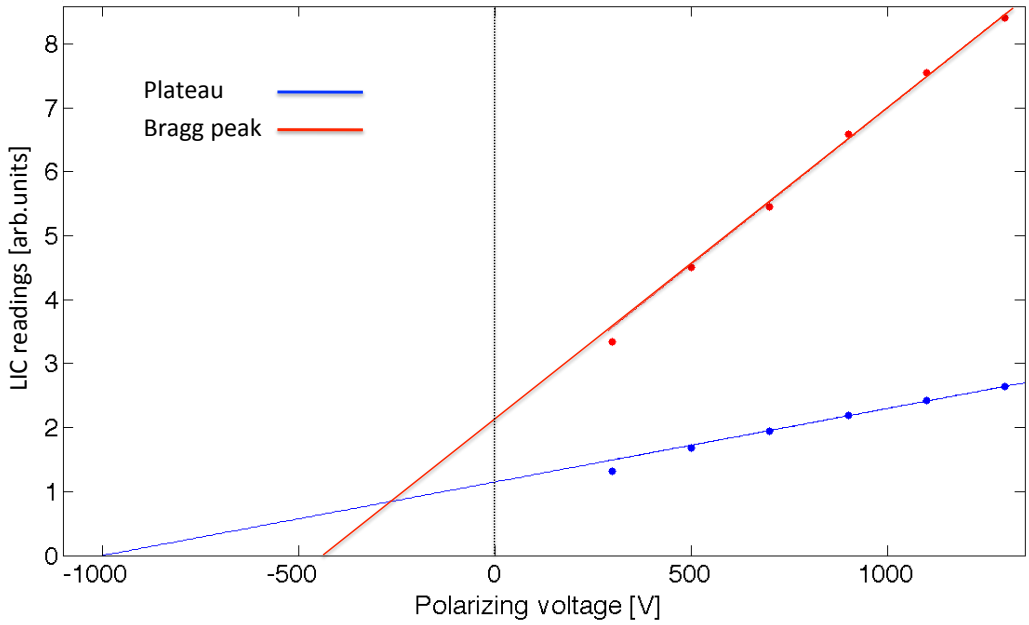

Figure 3.42: Voltage curve measured for antiprotons at two different depths: the data at 700, 900, 1100, 1300 V are fitted with a linear slope. The different intercept to slope is an index of the difference in LET in the Bragg peak and the entrance channel. Data are from the 2011 run.

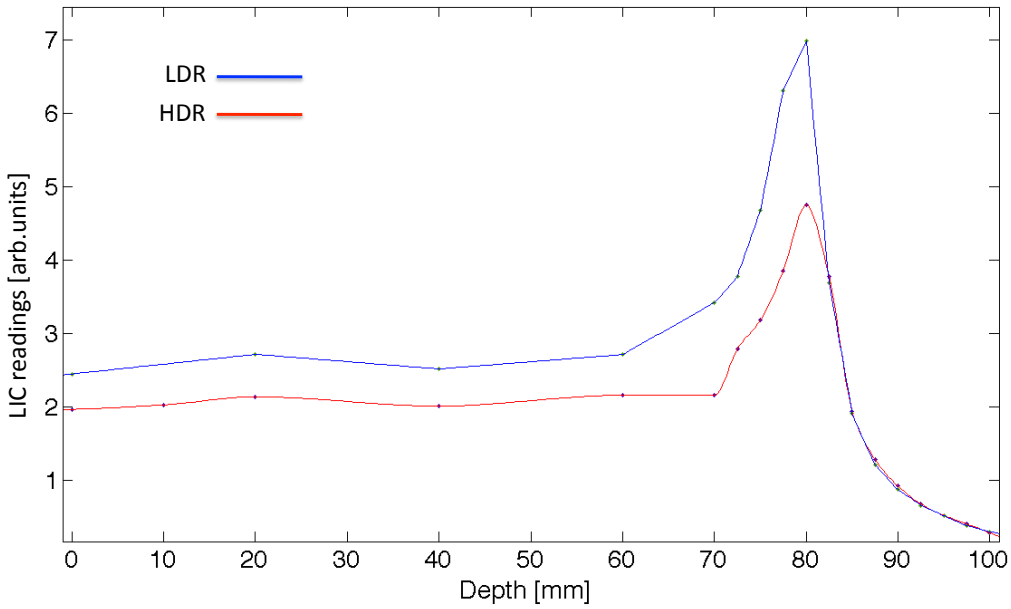

Figure 3.43: Depth dose curves measured with the 2D-array at two different dose rates, the high one in red (HDR) and the lower one in blue (LDR)(spline is shown to guide the eye).

available.

The dose-averaged LET of antiprotons was calculated with FLUKA and it is depicted in figure 3.44, in agreement with the one calculated by Bassler [4].

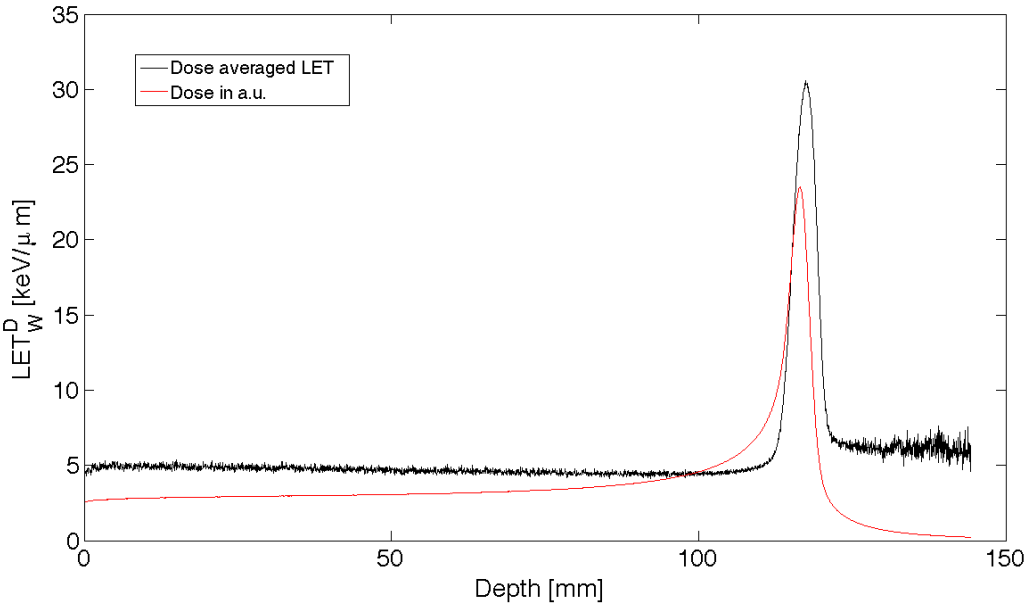

Figure 3.44: Dose-averaged unrestricted LET plotted as a function of depth in water (*courtesy of A. Mairani and K. Parodi*): the calculation is based on the FLUKA charged particle LET spectrum of a 126 MeV antiproton beam.

As previously mentioned, the LET^D_W curves shown in figure 3.38 for protons, carbon and oxygen indicate a particle-species dependent separation, while the fluence averaged (LET^F_W) curves (fig. 3.39) tend to present an energy separation: as only one energy was available for antiprotons, the calibration curve has only been evaluated for the dose averaged LET (LET^D_W). The calibration curves and the error bars have been evaluated with the same procedure already described for protons, carbon and oxygen. They are depicted in figure 3.45.

They are visibly affected by a dose-rate dependence, typical of general recombination losses. The high dose-rate curve is consequently shifted towards higher values of the recombination index, sensitive to LET.

In figure 3.46 the calibration curves for LET^D_W for protons, carbon, oxygen and antiprotons are plotted in the same graph.

Despite the separation between the two antiproton curves at the two different dose rates, they fit quite well in the general trend. The mismatch

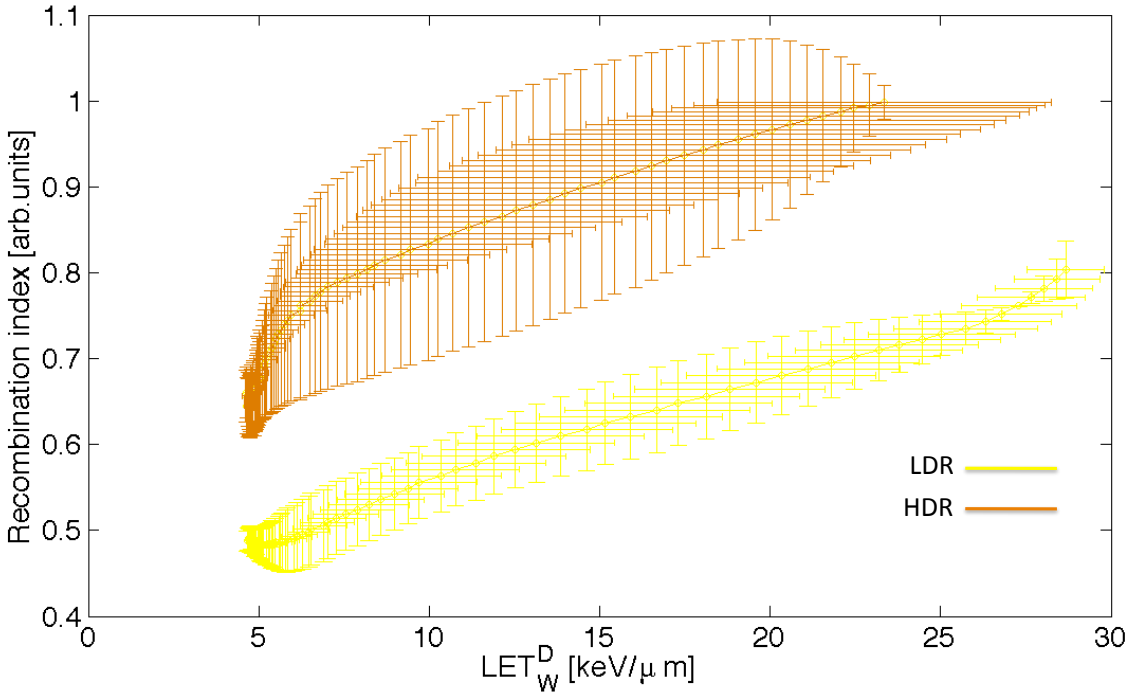

Figure 3.45: Recombination index vs. dose averaged LET for antiproton beam (E=126 MeV) at two different dose rates.

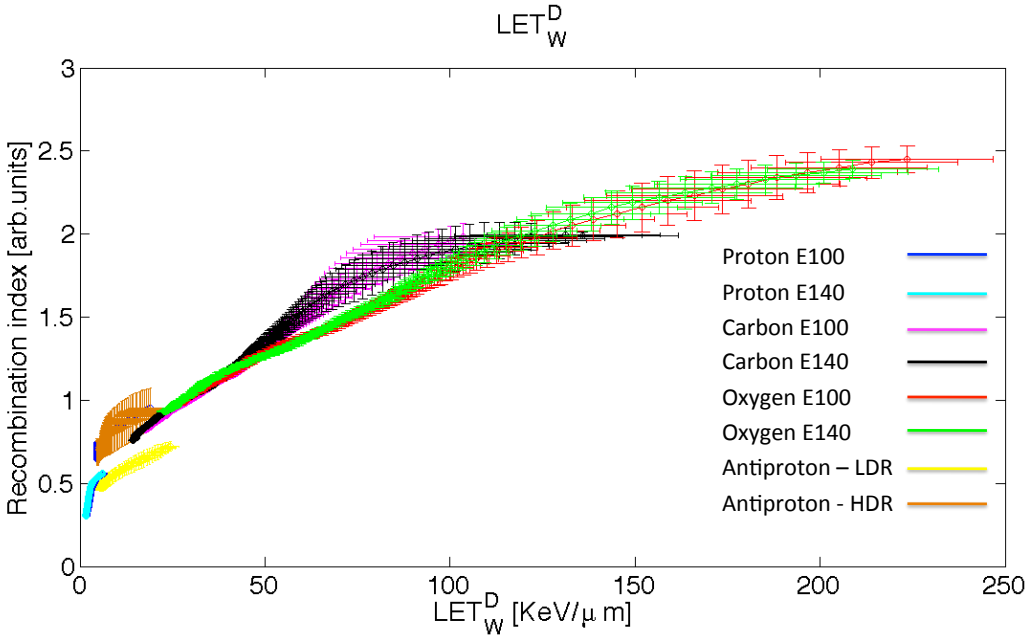

Figure 3.46: Recombination index vs. dose averaged LET for the proton beam (E=128.11 MeV/u), the carbon beam (E=241.84 MeV/u), the oxygen beam (E=286.05 MeV/u) and the antiproton beam (E=126 MeV).

in the absolute values of the recombination index between antiprotons and both protons and carbon ions is likely due to the extreme difference in dose rate ($\bar{p}$ = 6×10^{13} s^{-1}, C = 5.66×10^{6} s^{-1}). To resolve this issue, a complete correction for GR would be necessary. Anyway, to compare all the species, the experimental conditions should be as similar as possible.

This and other aspects of the experiments, together with some practical applications of the invented methodology will be discussed in the next session.

Chapter 4

Discussion and conclusion

The dependency of initial recombination (IR) processes on LET characterizes liquid filled ionization chambers and has been the starting point of our study.

Unfortunately, the lack of a theoretical model relating directly IR to LET does not allow to achieve a direct LET measurement. We investigated, therefore, methods to determine LET indirectly. A first approach is the study of the ionization curve and the change of its slope for different LET values. This procedure, however, is very sensitive on how the correction for general recombination (GR) is done. Moreover, assuming that such a correction is properly carried out, it requires the measurement of a whole voltage curve to evaluate the value of the slope. This has to be done at each point along the depth dose curve and it is, hence, quite time consuming and not practical.

A more robust method relies again on the dependence of IR on LET and it exploits the different sensitivities of LICs and ICs to IR losses. While in LICs IR is significant, in ICs it can be approximately neglected. The new approach consists, therefore, in measuring the signal at any point along the depth dose curve both, with the LIC and an IC. Subsequently, the ratio IC/LIC can be obtained and directly related to the Monte Carlo calculated LET of the particles in each measuring point along the depth dose curve. The final goal is to have, in the end, a calibration curve, in which the ratio value IC/LIC is plotted against LET, in a one-to-one correspondence.

Figure 3.46 shows the recombination index as a function of the dose-averaged LET (LET_W^D) for proton, carbon, oxygen and antiproton beams. The value of the recombination index increases with the LET for each particle type and is largely independent on the particle energy. All the different particles fit reasonably well, on a calibration band, within the error bars, that are relatively large.

One of the practical applications of the LIC would be an online monitoring of sudden changes of beam quality (change in the fragmentation spectra due

to setup errors) that would lead to a change in LET and, therefore, of the recombination index. The calibration band obtained in figure 3.46 is not yet, however, accurate enough to detect small changes in the LET spectra at a clinically relevant level. For this reason, the error bars for the recombination index need to be reduced as much as possible, especially in the Bragg peak region, where they become more important. Indeed, there are margins of improvement related to the experimental setup.

In particular, in one of the first stages of the analysis, our data showed, for a given particle type, a poor overlap of the calibration curves for the two beam energies. This was due to the fact that the beam size was larger than the dimensions of the matrix. When we realized the mismatch, we introduced a correction for such beam losses, which improved the overlap of the curves for two different energies for each particle type. However, in a future setup this source of error should and could be easily avoided.
Another limiting factor is the relatively large distance between the IC and the LIC, which could be minimized, to reduce the uncertainty in the shifting procedure preceding the recombination index calculation, responsible for the large horizontal error bars of the calibration curve, which are caused by the steepness of the depth LET curve.
Furthermore, a severe limitation of the current setup is the impossibility to perform a general recombination correction for the depth dose curves. Compared to the actual dimensions of the error bars, coming from the shifting procedure, this seems to be not a mayor problem in the measurements done at HIT, even though it turned out to be relevant in the CERN measurements, where we found a significant dose-rate dependence of the calibration curves, that could not be eliminated. Nevertheless, once the shifting-procedure error bars will be reduced, GR corrections will need to be taken into account more carefully.

In order to implement all the improvements in a new experimental setup, we discussed a next-generation version where the LIC and the IC with identical geometrical properties (size and pixelization) would be fused together. This would reduce uncertainties in the relative shift and the area coverage, which both are significant limitations in the current version. The idea of such a new apparatus and methodology for LET determination based on the calibration curve has been translated and developed into a Patent [113] (currently pending) together with our colleagues in USC. The design of the coupled system is depicted in figure 4.1.
The device body comprises three printed circuit boards (PCBs) and two

spacers. The upper PCB (1) is a multilayer circuit containing a segmented anode in pixels arranged in a 2D-array. In the outer layer (2), as well as in the inner one, tracks connect the different pixels to the read-out electronics. The gap between the PCB (1+2) and the PCB intermediate (4) is defined by a spacer (3) of a dielectric material, filled with isooctane. The intermediate layer contains two high voltage drift electrodes, one on each side, to create the potential difference required for reading the ionized charge both in the liquid and in the gas media. Another spacer (5) is attached to the PCB placed intermediate, to define the thickness of the gas gap. Finally, an additional multilayer PCB (6) contains an anode segmented in pixels and routing strips connecting the pixels to the read-out electronics.
The mass thickness of the layers of liquid, the gas and the intermediate PCB will be minimal to minimize the distance between the LIC and the IC. The beam (7) impinges on the system perpendicular to the plane of the detector.

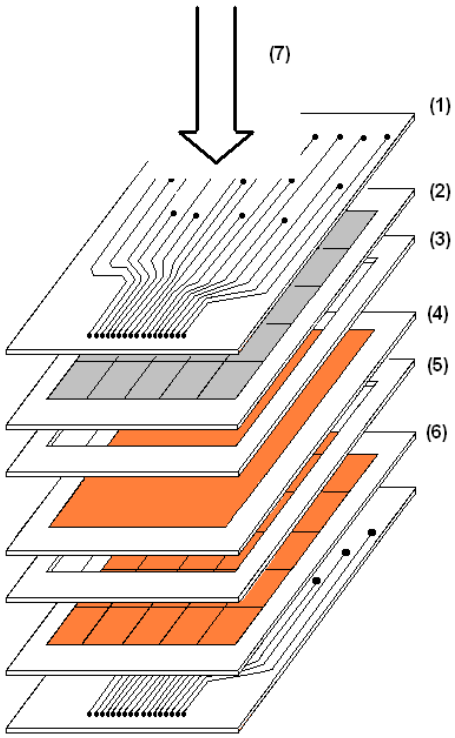

Figure 4.1: Design of the coupled system of LIC and IC for 2D LET map measurements: from the top to the bottom, the various components described in the text with the corresponding numbering are shown.

Figure 4.2 shows a transversal view of the device, comprising the IC plane (1) with the associated read-out electronics (2), the high-voltage intermediate plane (3) and the second LIC plane (4) with the associated read-out electronics (5). The beam is impinging on the planes of the pixelated ionization chambers perpendicularly from left (7). The system is immersed in a water phantom (6) to measure the LET variation in depth, therefore the device has to be water proof.

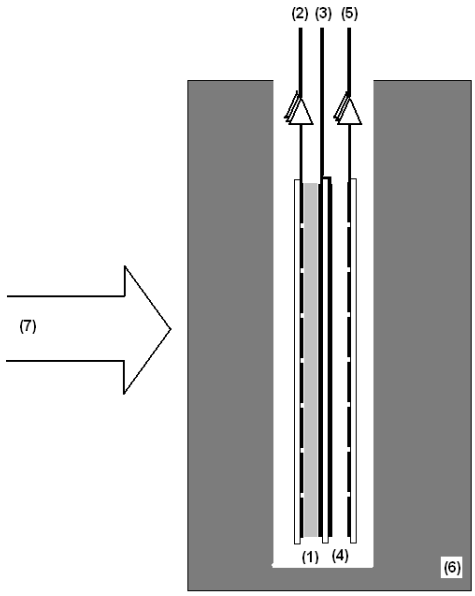

Figure 4.2: Transversal view of the device: the IC plane (1) and the associated read-out electronics (2), the high-voltage intermediate plane (3) and the second LIC plane (4) with the associated read-out electronics (5) are shown. The beam is impinging on the planes of the pixelated ionization chambers perpendicularly from left (7).

The new pixelized LIC-IC complex resolves the problems discussed and evidenced in the old version and could allow for a better correction for GR by using the 2DR or the 3VM approaches. Further improvement of the theoretical description of GR and IR would also be helpful.

Despite on the proton calibration curves at the two energies still lack an interpretation of the observed discrepancy in their shape, with the new improved setup the difference is expected to vanish and the error bars to be reduced.

Appendix A

Evaluation of f with the 3VM at different depths

The collection efficiency f changes with depth, decreasing while going from the entrance channel towards the Bragg peak region, due to the higher production of charge in this area. To apply the 3VM, therefore, a voltage curve at each depth is needed.

An alternative solution is to compute f in depth by relying on the Greening theory and the the 3VM (see par. 2.4.2) performed at a reference depth, where a whole voltage curve has been measured. Subsequently, f can be estimated at each depth.

The collected signal S_M can be expressed as a function of f:

$$S_M = S_0 \cdot f \tag{A.1}$$

where S_0 is the signal corrected for general recombination losses and f can be calculated with the 3VM according to:

$$f = \Big[1 + \frac{(1 + cV)A_c}{V^2}\Big]^{-1} \tag{A.2}$$

Here A_c and c are two parameters, the first one dependent on the dose rate and the second one independent on the dose rate.
In the reference point, the measured signal can be expressed as in equation (A.1):

$$S_M^{REF} = S_0^{REF} \cdot \Big[1 + \frac{(1 + c^{REF}V)A_c^{REF}}{V^2}\Big]^{-1} \tag{A.3}$$

and, for a certain depth d_i, S_0 and S_M are given, respectively, by:

$$S_0(d_i) = \frac{S_M(d_i)}{f(d_i)} \tag{A.4}$$

As we assume that S_0 and A_c depend in the same way on the dose rate, a factor Y_i can be introduced to keep into account the change of dose rate at each depth. Introducing Y_i, S_0 and A_c at each depth can be written as:

$$S_0(d_i) = S_0^{REF} \cdot Y_i \tag{A.5}$$

$$A_c(d_i) = A_c^{REF} \cdot Y_i \tag{A.6}$$

To estimate Y_i, S_M at each depth can be given by:

$$S_M(d_i) = S_0^{REF} Y_i \cdot \Big[1 + \frac{(1 + c^{REF} V) A_c^{REF} Y_i}{V^2}\Big]^{-1} \tag{A.7}$$

and then Y_i:

$$Y_i = \frac{S_M V^2}{S_0^{REF} V^2 - S_M A_c^{REF} - S_M c^{REF} V A_c^{REF}} \tag{A.8}$$

By substituting equation A.8 in equation A.5, the signal corrected for each depth can be estimated. This procedure has to be done for each individual channel of the matrix.

Bibliography

[1] L. Brualla-González et al, 2012 *"A two-dimensional liquid-filled ionisation chamber array prototype for small field verification: characterization and first clinical tests"*, Phys. Med. Biol., 57, 5221–5234

[2] G. Kraft, 2000 *"Tumor therapy with heavy charged particles"*, Prog. Part. Nucl. Phys. 45, S473-S544

[3] E. Haettner, H. Iwase, D. Schardt, 2006 *"Experimental fragmentation studies with ^{12}C therapy beams"*, Radiation Protection Dosimetry, Vol. 122, No. 1-4, pp. 485-487

[4] N. Bassler, M. Holzscheiter, 2009 *" Calculated LET spectrum from antiproton beams stopping in water"*, Acta Oncologica; 48: 223-226

[5] International Atomic Energy Agency (IAEA), 2000 *"Absorbed dose determination in external beam radiotherapy: an international code of practice for dosimetry based on standards of absorbed dose to water"*, IAEA Technical Reports Series (TRS) 398, Vienna

[6] G. Wickman, 1974 *"A liquid filled ionization chamber with high spatial resolution"*, Phys. Med. Biol. 19, 66-72

[7] C. Zankowski, E.B. Podgorsak, 1998 *"Determination of saturation charge and collection efficiency for ionization chambers in continuous beams"*, Med. Phys, Vol.25, n.6

[8] T. Kanai, M. Sudo, N. Matsufuji, Y. Futami, 1998 *" Initial recombination in a parallel-plate ionization chamber exposed to heavy ions"*, Phys. Med. Biol., 43, 3549-3558

[9] H. Tölli, R. Sjögren, M. Wendelsten, 2010 *" A two-dose-rate method for general recombination correction for liquid ionization chambers in pulsed beams"*. Phys.Med.Biol., 55, 4247-4260

[10] P.B. Scott, J. R. Greening, 1962 *" The determination of Saturation Currents in Free-air Ionization Chambers by Extrapolation Methods"*, Phys. Med. Biol., Vol.8, N.1, 51-57

[11] J. Pardo et al., 2005 *" Development and operation of a pixel segmented liquid-filled linear array for radiotherapy quality assurance"*, Phys. Med. Biol., 50, 1703-1716

[12] J. Pardo-Montero, F. Gómez, 2009 *" Determining charge collection efficiency in parallel-plate liquid ionization chambers"*, Phys. Med. Biol., 54, 3677–3689

[13] B. E. Johansson, J. Bahar-Gogani, G.Wickman, 1999 *" General collection efficiency in liquid isooctane and tetramethylsilane used as sensitive media in a thimble ionization chamber"*, Phys. Med. Biol., 44, 2161–2170

[14] B. E. Johansson, G. Wickman, 1997 *"General collection efficiency for liquid isooctane and tetramethylsilane used as sensitive media in a plane parallel ionization chamber"*, Phys. Med. Biol., 42, 133–45

[15] G. Shani, 2001 *" Radiation dosimetry: instrumentation and methods"*, CRC Press, Boca Raton, USA

[16] J. Bahar-Gogani, J. E. Grindborg, B. E. Johansson, G. Wickman, 2001 *" Long-term stability of liquid ionization chambers with regard to their qualification as local reference dosimeters for low dose-rate absorbed dose measurements in water"*, Phys. Med. Biol., 46, 729–740

[17] G. F. Knoll *"Radiation detection and measurement"*, New York: John Willey & Sons

[18] J. E. Turner *"Atoms, Radiation , and Radiation Protection"*, Third Edition, Wiley-VHC, Inc. (2007).

[19] L. Onsager, 1938 *"Initial recombination of ions "*, Phys. Rev. 54 554-7

[20] E. Kara-Michailova, D. E. Lea, 1939 *"The interpretation of ionization measurements in gases at high pressures*, Proc Camb Phil., 36 : 101–126.

[21] D. E. LEA, 1934 *"The theory of ionisation measurements in gases at high pressures"*, Proc. Cambridge Phil. Soc. 30, 80

[22] G. Mie, 1904 *"Der elektrische strom in ioniserter luft in einem ebenen kondensator"*, Ann. Phys., Lpz., 13, 857–89

[23] J. J. Thomson, E. Rutherford, 1896 *"On the passage of electricity through gases exposed to roentgen rays"*, Phil. Mag., 42, 392–407

[24] S. N. Ahmed, 2007 *" Physics and Engineering of Radiation Detection"*, First Edition, Academic Press

[25] M. Martisıkova, B. Ackermann, O. Jäkel, 2008 *"Analysis of Uncertainties in Gafchromic EBT Film Dosimetry of Photon Beams"*, Phys. Med. Biol., 53, 7013–7027

[26] H. Palmans, 2003 *"Effect of Alanine Energy Response an Phantom Material on Depth Dose Measurements in Ocular Proton Beams"*, Tech. in Canc. Res. Treatm., 2(6):579–586

[27] N. Bassler, 2006 *"Experimental Studies Relevant for Antiproton Cancer Therapy"*, PhD Thesis, University of Aarhus

[28] J. J. Wilkens, 2003 *"Evaluation of Radiobiological Effects in Intensity Modulated Proton Therapy: New Strategies for Inverse Treatment Planning"*, PhD Thesis, University of Munich

[29] M. Sakama, T. Kanai, Y. Kase, M. Komori, A. Fukumura, T. Kohno, 2005 *"Responses of a Diamond Detector to High-LET Charged Particles"*, Phys. Med. Biol., 50(4), 2275– 2289

[30] J. W. Boag, 1969 *"General Recombination in a standard parallel-plate free-air ionization chamber"*, Int. J. Radiat. Phys. Chem, Vol.1, pp. 267-285

[31] J. R. Greening, 1964 *"Saturation Characteristics of Parallel-Plate Ionization Chambers"*, Phys. Med. Biol., 9 143

[32] A. Fassò et al., 2003 *"The physics models of FLUKA: Status and recent developments"*, Computing in High Energy and Nuclear Physics 2003 Conference, La Jolla, CA (Paper No. MOMT005), eConf C0303241 (2003), e-print arXiv:hep-ph/0306267

[33] M. Bruzzi, 2009 *"Diamond Radiation Sensors for Radiotherapy"*, in RS Sussmann (ed.), CVD Diamond for Electronic Devices and Sensors, pp. 185-206

[34] C. S. Wedlund et al., 2011 *"On the energy per ion pair in planetary atmospheres"*, Ann. Geophys., 29, 187–195, 2011

[35] A.Mozumder, 1974 *"Effect of an external electric field on the yield of free ions: I. General results from the Onsager theory"*, J. Chem. Phys, 60, 4300-4304

[36] A.Mozumder, 1999 *"Fundamentals of Radiation Chemistry"*, Academic Press, San Diego, California

[37] K. J. Stewart et al, 2007 *"Development of a guarded liquid ionization chamber for clinical dosimetry"*, Phys.Med.Biol., 52, 3089-3104

[38] R. A. Holroyd, D. F. Anderson, 1985 *"The physics and chemistry of room-temperature liquid-filled ionization chambers"*, Nucl.Instrum.Methods A, 236, 294-9

[39] J. P. Montero, S. Tegami, A.Gago-Arias. D.M.González-Castaño, M. H. Holzscheiter, F. Gómez, 2012 *"Analysis of ionic mobilities in liquid isooctane with low dose radiotherapy pulsed photon beams"*, JINST, Vol. 7

[40] J. Pardo Montero, Ph.D. Thesis, Universidade de Santiago de Compostela, 2006

[41] K. J. Stewart, Ph.D. Thesis, McGill University, Montreal, 2007

[42] A. Mairani, Ph.D. Thesis, Universitá degli Studi di Pavia, Italy, 2007

[43] H. A. Bethe, 1930 *"Zur theorie des durchgangs schneller korpuskularstrahlen durch materie"*, Ann. Phys. 5, 325

[44] W. R. Leo, 1994 *"Particle Physics Experiments: A How-To Approach"*, Springer

[45] http://physics.nist.gov/PhysRefData/Star/Text/PSTAR.html

[46] ICRU Report 16 (1970), International Commission on Radiation Units and Measurements *"Stopping powers and ranges for protons and alpha particles"*

[47] http://physics.nist.gov/PhysRefData/Star/Text/ESTAR.html

[48] T. Elsässer, M. Krämer, M. Scholz, 2008 *" Accuracy of the local effect model for the prediction of biologic effects of carbon ion beams in vitro and in vivo"*Int. J. Radiation Oncology Biol. Phys., Vol. 71, No. 3, pp. 866–872

[49] M. Durante, J. S. Loeffler, 2010 *"Charged particles in radiation oncology"*, Nat. Rev. Clin. Oncol. 7, 37–43

[50] http://www.klinikum.uni-heidelberg.de

[51] M. H. Holzscheiter et al., 2006 *"The biological effectiveness of antiproton irradiation"*, Radiotherapy and Oncology, 81, 233-242

[52] A. H. Sullivan *"A measurement of the local energy deposition coming to rest in tissue-like material"*, Phys. Med. Biol., 1985, Vol. 30, No. 12, 1297-1303

[53] J. N. Kavanagh et al., 2010 *"Experimental setup and first measurement of DNA damage induced along and around an antiproton beam"*, Eur. Phys. J. D, 60, 209-214

[54] M. J. Berger et al, 1998 *"XCOM: Photon Cross Section Database"*, NIST Standard Reference Database 8 (XGAM)

[55] D. R. Olsen, O. S. Bruland, G. Frykholm, and I. N. Nordergaug, 2007 *"Proton therapy – A systematic review of clinical effectiveness"* Radiother. Oncol. 83, 123–132

[56] M. J. Berger, 1993 *"ESTAR, PSTAR, ASTAR: a PC package for calculating stopping powers and ranges of electrons, protons and helium ions"*, IAEA Technical Reports Series (NDS) 144

[57] B. Allen, L. Marcu, E. Bezak, 2012 *"Biomedical Physics in Radiotherapy for Cancer"*, Springer Science and Business Media B.V., New York

[58] U. Linz, in: U. Linz (ed.), 1995 *"Ion Beams in Tumour Therapy"*, Chapman and Hall, 15

[59] S. P. Ahlen, 1980, *"Theoretical and experimental aspects of the energy loss of relativistic heavily ionizing particles"*, Rev. Mod. Phys., vol.52, n.1

[60] W. H. Barkas, 1963 in: Nuclear Research Emulsions, Vol. I, Academic Press, New York - London, 371

[61] *http : //www.wcrf.org/cancer_statistics/world_cancer_statistics.php*

[62] W. Schlegel, T. Bortfeld, and A-L. Grosu, editors *"New technologies in radiation oncology"*, p. 366, Med. Radiology/Radiation Onc. Springer, 2006. 2

[63] RR. Wilson., 1946, *"Radiological use of fast protons"*, Radiology, 47:487–491, 1, 2, 3, 4

[64] Scott, W. T., 1963, *"The theory of small-angle multiple scattering of fast charged particles"*, Rev. Mod. Phys. 35, 23

[65] http://pdg.lbl.gov/2011/reviews/rpp2011-rev-passage-particles-matter.pdf

[66] B.Erdelyi, 2009 *"A comprehensive study of the most likely path formalism for proton-computed tomography"*, Phys. Med. Biol., 54, 6095-6122

[67] P. V. Vavilov, 1957, *"Ionizational losses of high energy heavy particles"*, Zh. Eksp. Teor. Fiz. 32, 920–923. Sov. Phys. JETP 5, 749–751

[68] B. Rossi, 1952, *"High-Energy Particles, Prentice-Hall Physics Series"*, Prentice-Hall, Englewood Cliffs, NJ.

[69] R. Serber, 1947 *"Nuclear reactions at high energies"*, Phys. Rev. 72 1114–5

[70] H. Paganetti, 2002 *"Nuclear interactions in proton therapy: dose and relative biological effect distributions originating from primary and secondary particles"*, Phys. Med. Biol, 47, 747

[71] ICRU, 1993, ICRU Report 51, *"Quantities and Units in Radiation Protection Dosimetry"* , International Commission on Radiation Units and Measurements, Bethesda, MD

[72] A. Ottolenghi, M.Merzagora , H. G. Paretzke, 1997 *" Dna complex lesions induced by protons and α-particles: track structure characteristics determining linear energy transfer and particle type dependence"*, Radiat. Environm. Biophys., 36, 96-103

[73] C. Tobias , 1985 *"The repair-misrepair model in radiobiology: comparison to other models.* Radiation research. Supplement, 8:S77–95

[74] D. Schardt , T. Elsässer, D. Schulz-Ertner 2010 *"Heavy-ion tumor therapy: Physical and radiobiological benefits"*, Rew Mod Phys, Vol 82

[75] M. Holzscheiter et al., 2010 *"Biological Effect of Antiprotons: are Antiprotons a Candidate for Canter Therapy?"*, AD-4 Status Report for Experiment AD-4/ACE 2010

[76] F.J.Kaiser, H. Tölli, *"Initial recombination in liquid filled ionization chambers: Charge carrier distributions and the effect on columnar recombination"*, private communication

[77] J. Andersson et al., 2012 *"A comparison of different experimental methods for general recombination correction for liquid ionization chambers"*, Phys.Med.Biol., 57

[78] J. Pardo et al., 2004 *"Free ion yield observed in liquid isooctane irradiated by γ-rays. Comparison with the Onsager theory"*, Phys.Med.Biol. 49, 1905-1914

[79] A.Ferrari et al., 1992 *"An improved multiple scattering model for charged particle transport"*, NIM B, 412-426

[80] A.Fassò et al., 1997 *"New developments in FLUKA modelling of hadronic and EM interactions"*, Proc. 3rd Workshop on Simulating Accelerator Radiation Environments (SARE 3), KEK, Tsukuba, Japan

[81] F. Sommerer et al., 2006 *"Investigating the accuracy of the FLUKA code for transport of therapeutic ion beams in matter"*, Phys. Med. Biol. 51, 4385

[82] I. Kantemiris, 2011 *"Dose and dose averaged LET comparison of ^{1}H, ^{4}He, ^{6}Li, ^{8}Be, ^{10}B, ^{12}C, ^{14}N, and ^{16}O ion beams forming a spread-out Bragg peak"*, Med. Phys., 38, 12

[83] A. Mairani, 2007 *"Nucleus-nucleus interactions modeling and applications in ion therapy and treatment planning"*, Scientifica Acta 1(1), 129-132

[84] *http : //www.fluka.org/fluka.php*

[85] U. Weber, G. Kraft, 1999 *"Design and construction of a ripple filter for a smoothed depth dose distribution in conformal particle therapy"*, Phys. Med. Biol., 44, 2765-2775

[86] F.Bourhaleb et al., 2008 *"Monte Carlo simulations of ripple filters designed for proton and carbon ion beams in hadrontherapy with active scanning technique"*, Journal of Physics: Conference Series 102, 012002

[87] August 2004, *"Tissue inhomogeneity corrections for megavoltage photon beams"*, aapm report. n.85

[88] Ph. Bernhardt et al., 2002 *"Monte Carlo simulation of DNA damage by low LET radiation using inhomogeneous higher order DNA targets"*, Rad. Prot. Dos., Vol. 99, Nos 1-4, pp. 203-206

[89] http://mightylib.mit.edu

[90] U. Weber, G.Kraft, 2000 *"Comparison of Carbon Ions versus Protons"*, The Cancer Journal, 1528-9117

[91] C.Grassberger et al., 2011, *"Variations in Linear Energy Transfer Within Clinical Proton Therapy Fields and the Potential for Biological Treatment Planning"*, I. J. Rad. Onc., Biol, Phys, vol.80, n.5

[92] J.F.Fowler, 2006 *"Development of radiobiology for oncology—a personal view"*, Phys.Med.Biol 51, R263-R286

[93] H. Paganetti et al., 2002 *"Relative Biological Effectiveness (RBE) values for proton beam therapy"*, Int.J.Rad.Onc.Biol.Phys., vol.53, n.2, pp.407-421

[94] Copyright © 2012 International Commission on Radiation Units and Measurements

[95] J. V. Siebers et al., 2000 *"Converting absorbed dose to medium to absorbed dose to water for Monte Carlo based photon beam dose calculations"*, Phys.Med.Biol., 45, 983-995

[96] Dan T.L.Jones, 2006 *"The w-value in air for proton therapy beams"*, Rad.Phys. and Chem., 75, 541-550

[97] ICRU Report 60 (1998), International Commission on Radiation Units and Measurements *"Fundamental Quantities and Units for Ionizing Radiation"*

[98] G. Wickmann, H. Nyström, 1991 "The use of liquids in ionization chambers for high precision radiotherapy dosimetry", Phys. Med. Biol., 37, 1789

[99] A. Ore, A. Larsen, 1964 *"Relative frequencies of ion clusters containing various numbers of ion pairs"*, Rad. Res., Vol.21, N.3, pp.331-338

[100] J. Andersson, H. Tolli, 2011 *"Application of the two-dose-rate method for general recombination correction for liquid ionization chambers in continuous beams"*, Phys. Med. Biol., 56, 299-314

[101] http://physics.nist.gov/PhysRefData/Star/Text/ESTAR.html

[102] K. Eberle et al., 2003, *"First tests of a liquid ionization chamber to monitor intensity modulated radiation beams"*, Phys. Med. Biol, 48, 3555-3564

[103] T. Berghöfer, 2005, *"A liquid ionization chamber as monitor in radiotherapy"*, Proceedings Trim Size: 9inX6in, Como

[104] T. Winkelmann et al., 2008 *"Experience at the ion beam therapy center (HIT) with two years of continuous ECR ion source operation"*, Proceedings of ECRIS08, Chicage, IL USA

[105] Z. Chen et al., 2007 *"Principles and requirements of external beam dosimetry"*, Rad. Meas. 41, S2-S21

[106] J. F. Fowler, F. H. Attix, 1966 *"Solid state integrating dosimeters"*, Radiation Dosimetry vol 2 (New York: Academic) 241-90

[107] T. Eriksson, 2009 *"AD: low-energy antiproton production at CERN"*, Hyperfine Interact, 194:123-128

[108] https://espace.cern.ch/liu-project/default.aspx

[109] J. C. H. Chu, 1980 *"A liquid ionisation chamber for neutron dosimetry"*, Phys. Med. Biol., vol.25, N.6, 1133-1148

[110] H. V. Knudsen, 2008 *"Antiproton therapy"*, Nucl. Instr. and Meth. in Phys. Res. B 266, 530-534

[111] N. Bassler, 2008 *"Antiproton Radiotherapy"*, Radiotherapy and Oncology 86, 14-19

[112] L. Gray, TE. Kalogeropoulos, 1984 *"Possible biomedical applications of antiproton beams: focused radiation transfer"*, Radiat. Res.: 246–52.

[113] Authors: F. G. Rodríguez, J. P. Montero, S. Tegami, M. Holzscheiter, 2012 *"Method and apparatus for measuring linear energy transfer and energy of hadron beams"*, Patent holding body: Universidade de Santiago de Compostela, Application number: P201231211, Priority country: Spain

[114] B. Rossi, 1965 *"High-Energy Particles"*, Prentice Hall Series

[115] G. Jaffé, 1906 *"Sur la conductibilitá álectrique de l'áther de petrole sous l'action du radium"*, J. Physique, 4, 262–70

[116] G. Battistoni, S. Muraro, P. R. Sala, F. Cerutti, A. Ferrari, S. Roesler, A. S Fassò. J. Ranft, 2007 *"The FLUKA code: description and benchmarking"*, AIP Conference Proceeding 896, 31-49

[117] A. Ferrari, P. R. Sala, A. Fassò, J. Ranft, 2005 *"FLUKA: a multi-particle transport code"*, CERN-2005-10, INFN/TC_05/11, SLAC-R-773

[118] S. Sellner, 2010, Diploma Thesis, University of Heidelberg

[119] E. Haettner, 2006, Diploma Thesis, GSI, Darmstadt

Acknowledgements

My first acknowledgement is addressed to Dr. Michael Holzscheiter, who gave me the opportunity to carry out my PhD in Heidelberg.
I would also like to thank Prof. Dr. Joachim Ullrich, for the fruitful discussions and valuable advises given to me especially in the last phases of my PhD.
I would also like to thank Prof. Oliver Jäkel, for his beneficial advises and for having introduced me to the E0409 group of DKFZ.
I want to express my sincere gratitude to Prof. Faustino Gómez Rodríguez, for his precious and friendly collaboration and for always supporting me until the end of my PhD.
A special acknowledgement is to Dr. Juan Pardo Montero, for his invaluable support, endless availability and effective discussions, and for always having guided me through hard times.
A warm thank to Stefan Sellner, the best office mate that one could desire, who sacrificed many of his nights to assist me during the experiments.
I thank also Carsten Welsch, for having involved me in a number of interesting initiatives.
I would also like to thank Stephan Brons, who always helped me during the experiments carried on at HIT, Katia Parodi and Andrea Mairani, for the precious time they dedicated to me.
Finally, I want to thank from the bottom of my heart my parents and my brother, who always believed in me and encouraged me with their love and support. Thank you to all my friends, near and far, who shared with me the last three years in Germany, making me feel like at home: Anto, Franci, Clara, Andre, Joe, Christian, Britta, Carlos, Andrea F.P.. And thanks Tommi, for having been so patient.

Acknowledgements

Erklärung

Diese Arbeit ist von mir selbstständig verfasst worden. Ich habe keine anderen als die von mir angegebenen Quellen und Hilfsmittel benutzt.

Heidelberg, 08.02.2013 .....

Sara Tegami